

DIOXYPYRROLE BASED SUPERCAPACITORS FOR ENERGY STORAGE

By

MERVE ERTAS

A DISSERTATION PRESENTED TO THE GRADUATE SCHOOL  
OF THE UNIVERSITY OF FLORIDA IN PARTIAL FULFILLMENT  
OF THE REQUIREMENTS FOR THE DEGREE OF  
DOCTOR OF PHILOSOPHY

UNIVERSITY OF FLORIDA

2009

© 2009 Merve Ertas

To my mom and dad

## ACKNOWLEDGMENTS

I would like to express my sincere gratitude to my advisor Prof. John R. Reynolds. The time in graduate school, especially in a foreign country, was one of the most challenging, yet rewarding and life changing experiences I have yet to go through, and none of it would have been possible without the support and guidance of him. I admire him not only as a scientist but as a person. I feel very fortunate having him as my research advisor and deeply thankful for his attention on my scientific, professional and personal development. I appreciate his complete confidence in my abilities as a chemist. He has always treated me with the utmost respect and I have learned plenty from him. I am grateful for his unique enthusiasm and optimism in science, his encouragement, his patience, his words of wisdom, and most importantly his genuine concern. I will forever be thankful for his presence in my life.

I would like to give my special gratitude to Prof. Andrew G. Rinzler, who in reality has been a second advisor to me. For the last three years, he welcomed me in his laboratory, guided me, was always interested in and appreciative of my work and patiently answered all my questions. I have to admit that I feel extremely privileged having collaborated with such a passionate scientist. I would also like to express my appreciation to the rest of my supervisory committee members; Professors Kenneth B. Wagener, David B. Tanner and Randolph S. Duran for the time they invested in reading and discussing this document.

Sincere gratitude goes to my undergraduate and masters thesis advisor Prof. Levent Toppare, who introduced me to the area of conducting polymers and encouraged me to pursue higher studies. He prepared me well for the challenge of studies abroad. Without the support and guidance of him, I would have not become a chemist.

I would like to thank Cheryl Googins, Sara Klossner and Gena Borrero in the polymer office and Lori Clark in the graduate office for their help getting me through the complex

administrative work. They always made sure that everything ran smoothly and have taken care of many problems that never reach our ears.

During my graduate career, I have had a pleasure to meet and work side by side among some extraordinary people who had a major impact throughout the completion of this dissertation. I would like to thank many past and current members of the Reynolds group for their time, advice, scientific help and laughs. I also thank the Rinzler group members for welcoming me to their lab and being always so helpful. Many thanks go to Dr. Ryan Walczak for working closely with me on several of the projects presented in this dissertation, providing me Sticky-PF and all the scientific and non-scientific discussions and also for his friendship. It was always a pleasure to “argue” with him over our coffee breaks. One person that I can definitely not omit is Rajib Das, who I thank for his research collaboration, his contributions in collecting some of the data presented in Chapter 3 and the time he put on assisting me in preparation of the SWNT films. I would like to thank Tim Steckler for providing me his precious DAD monomers presented in Chapter 4. I could not ask for a better colleague and friend to go together through the different times in graduate school. I also acknowledge Karen Kelly for her expertise and for assisting me through the SEM analysis. Special thanks go to Dr. Avni Argun, who was my mentor in the lab during the first year in graduate school. I extend my thanks to Dr. Christophe Grenier for his support during the first year and Dr. Jeremiah Mwaura for his help during my qualifying exam. I also offer thanks to Dr. Svetlana Vasilyeva, my successor as “Faraday Cage Coordinator”, for taking over all the lab duties and her immediate help when I needed it during the last year.

My time in Gainesville would not have been the same without my dear friends Dr. Josh McClellan, Dr. Kornelia Matloka, Dr. Sophie Bernard, Dr. Florence Courchay and Dr. Piotr

Matloka. They have accepted me for who I am, and have always been there for me through my ups and downs. I will never forget all the wonderful time we spent together. I also thank Jordan Mathias for all the good memories. I would like to give special thanks to Laura Moody, especially for her help in proofreading this document and for being such a great friend through the good and the difficult times. Enough thanks cannot be expressed to Dr. Olga Zolotarskaya for being such a wonderful friend whom I was very lucky to meet during the last chapter of Gainesville. I would also like to thank my friends from Turkey for being never more than a phone call away whenever I needed them. I am particularly thankful to Dr. Zeynep & Umut Sargut for their continuous friendship, being the best support a person could ask, and making me feel close to home throughout all the years in Gainesville. They were always there for me in the worst and the best of times and truly hold a special place in my heart. I would like to thank Dr. Scott Selph, for his support no matter how unbearable I get, especially during the incredibly stressful writing process. In the last two years of my graduate career, his constant love and enthusiasm kept me going and got me through some rough times. Even far away he always managed to keep my spirit up when I needed it the most. I feel very lucky to have him in my life.

Last and foremost, I would like to thank my parents Tomris and Prof. Arif Ertas for their eternal love, understanding, and support. They taught me how to work hard to pursue my dreams and have always supported all my decisions even at younger ages. Their courage and faith in me are the reasons that I became the person I am today. Words could never describe the respect, the love, and the gratitude I feel. I also thank my dear brother Emre Ertas for his support through the difficult times and cheerful conversations on the phone. I would have never come this far without them.

## TABLE OF CONTENTS

	<u>page</u>
ACKNOWLEDGMENTS .....	4
LIST OF TABLES .....	9
LIST OF FIGURES .....	10
ABSTRACT .....	14
CHAPTER	
1 INTRODUCTION .....	16
Historical Background .....	16
Operation Fundamentals .....	18
Comparison of Energy Storage in Capacitors and Batteries .....	19
Electric Double-Layer Capacitance .....	21
Pseudocapacitance .....	23
Adsorption pseudocapacitance .....	24
Redox pseudocapacitance .....	26
Electrode Materials .....	27
Carbon .....	27
Activated carbons .....	29
Carbon aerogels .....	30
Carbon nanotubes .....	30
Metal Oxides .....	31
Conducting Polymers .....	32
Type I & II supercapacitors .....	35
Type III & IV supercapacitors .....	37
Review of conducting polymer based supercapacitor literature .....	37
Applications and Current Industry .....	39
Structure of Dissertation .....	41
2 EXPERIMENTAL TECHNIQUES .....	43
Chemicals and Materials .....	43
Inert Atmosphere Handling .....	44
Electrochemical Methods .....	45
Cyclic Voltammetry .....	46
Constant Potential Method: Chronocoulometry / Chronoamperometry .....	48
Constant Current Method: Chronopotentiometry .....	49
Electropolymerization .....	49
Electrochemistry of Electroactive Film .....	51
Supercapacitor Device Fabrication .....	52
Energy and Power Characteristics of a Device .....	55

Surface Characterization Techniques .....	56
Scanning Electron Microscopy.....	57
Atomic Force Microscopy .....	57
3 PProDOP BASED TYPE I SUPERCAPACITORS.....	60
PProDOP as a Charge Storage Electrode Material.....	60
Electropolymerization of ProDOP.....	62
Electrochemistry of PProDOP Films.....	66
Surface Analysis of PProDOP.....	69
Capacitances of the PProDOP Films on Gold Electrodes .....	72
Type I Supercapacitor Devices with Gold Substrate.....	76
Stability of Type I Supercapacitor Devices with Gold Substrate .....	80
SWNT Films as Electrode Substrates.....	83
SWNTs Film Preparation .....	84
Comparison of Gold and SWNTs Substrates in Device Performances.....	86
Non-Covalent Modification of SWNT Surfaces with Sticky-PF .....	89
Electropolymerization of ProDOP on Bare and Sticky-PF coated SWNT Films .....	94
Electrochemistry of PProDOP Film on Sticky-PF coated SWNTs Film .....	97
Surface Analysis of PProDOP Film on Sticky-PF Coated SWNTs Film.....	102
Type I Supercapacitor Devices with Sticky-PF Coated SWNT Substrates.....	104
Stability of Type I Supercapacitors with Sticky-PF coated SWNTs Substrate.....	105
Conclusions and Perspective .....	108
4 TYPE IV SUPERCAPACITORS: Donor-Acceptor-Donor Systems.....	110
Introduction.....	110
Cyclic Voltammetric Deposition of DAD Systems.....	113
Electrochemistry of P(DAD) Films .....	116
Capacitances of P(DAD) Films .....	121
Type IV Supercapacitors .....	127
Conclusions and Perspective .....	136
5 HYBRID SUPERCAPACITORS: Ruthenium Oxides PProDOP.....	137
Introduction.....	137
Cyclic Voltammetric Deposition of Hydrous Ruthenium Oxide .....	139
Characterization of RuO <sub>x</sub> ·nH <sub>2</sub> O and Composite Films of RuO <sub>x</sub> ·nH <sub>2</sub> O with PProDOP .....	142
Electrochemical Characterization.....	142
SEM Analysis.....	151
XPS Analysis.....	152
Characterization of the RuO <sub>x</sub> ·nH <sub>2</sub> O PProDOP Supercapacitor .....	154
Conclusions and Perspective .....	157
LIST OF REFERENCES.....	159
BIOGRAPHICAL SKETCH .....	170

## LIST OF TABLES

<u>Table</u>		<u>page</u>
3-1	Capacitances, energy and power densities of PProDOP films and devices.....	105
4-1	Charge densities and capacitances of PBEDOT-BBT, PBEDOT-TQ-Me <sub>2</sub> and PBEDOT-TQ-Hx <sub>2</sub> with different deposition cycles.....	125
4-2	Charge densities and capacitances of devices prepared by PBEDOT-BBT, PBEDOT-TQ-Me <sub>2</sub> and PBEDOT-TQ-Hx <sub>2</sub> with different amount of PProDOP films.....	134
5-1	Capacitances, energy and power densities of the films and devices of RuO <sub>x</sub> ·nH <sub>2</sub> O PProDOP composite. ....	157

## LIST OF FIGURES

<u>Figure</u>	<u>page</u>
1-1 Ragone plot of various energy storage devices.....	18
1-2 Schematic of a electrical double-layer supercapacitor.....	22
1-3 Schematic diagram of a supercapacitor utilizing conducting polymers. ....	35
1-4 Classification of conjugated polymers in Type I to Type III supercapacitor. ....	36
3-1 Structure of poly(3,4-propylenedioxyppyrrrole) with its electropolymerization mechanism. ....	62
3-2 Electrochemical polymerization of PProDOP in TBAP/PC on Au Button, in LiBTI/PC on Au Button and in LiBTI/PC on Au/Kapton. ....	65
3-3 Cyclic voltammograms and capacitances as a function of applied potential of PProDOP films on Au/Kapton substrates.....	68
3-4 Scanning electron micrographs of PProDOP films on Au/Kapton deposited in LiBTI/PC.....	70
3-5 Scanning electron micrographs of PProDOP films on Au/Kapton deposited in TBAP/PC. ....	71
3-6 Calibration curves: Deposition charges and capacitances of PProDOP as a function of the mass of PProDOP on Au/Kapton substrates.....	73
3-7 Schematic diagram of Type I supercapacitor configuration utilizing PProDOP and photograph of Type I PProDOP supercapacitor with Au/Kapton substrate. ....	77
3-8 Cyclic voltammograms and capacitances as a function of applied potentials of Type I PProDOP supercapacitor with Au/Kapton substrates.....	78
3-9 Stability of Type I PProDOP supercapacitors with Au/Kapton substrates.....	82
3-10 Fabrication of SWNT Film.....	85
3-11 Atomic force micrograph of SWNTs film.....	86
3-12 Cyclic voltammograms and capacitances as a function of applied potential of Type I PProDOP supercapacitor with SWNTs substrates.....	87
3-13 Constant current charging/discharging of Type I PProDOP supercapacitor with Au/Kapton and SWNTs film substrates.....	89

3-14	Structure of poly(9,9-dioctylfluorene) (Sticky-PF) and its proposed non-covalent association with a SWNT surface. ....	91
3-15	Atomic force micrographs of SWNTs film before and after Sticky-PF coating. ....	93
3-16	Absorbance spectra of Sticky-PF coated SWNT film and solution of Sticky-PF in chloroform. ....	93
3-17	Schematic representation of PProDOP electrodeposition onto Sticky-PF SWNTs film. ....	94
3-18	Electrochemical polymerization of ProDOP in LiBTI/ACN on Sticky-PF SWNTs and bare SWNTs. ....	95
3-19	Cyclic voltammograms of PProDOP on Sticky-PF SWNTs and bare Sticky-PF SWNTs film in LiBTI/ACN. ....	99
3-20	Calibration curves: Deposition charges and capacitances of PProDOP as a function of the mass of PProDOP on Sticky-PF SWNTs substrates. ....	101
3-21	Cyclic voltammograms and capacitances as a function of applied potential of PProDOP films on Sticky-PF SWNTs in LiBTI/ACN. ....	102
3-22	Scanning electron micrographs of PProDOP films on Sticky-PF SWNTs substrates. ....	103
3-23	Cyclic voltammograms and capacitances as a function of applied potential of Type I PProDOP supercapacitor with Sticky-PF SWNTs substrates using LiBTI gel electrolyte. ....	104
3-24	Stability of Type I PProDOP supercapacitors with Sticky-PF SWNTs substrates using LiBTI gel electrolyte. ....	107
4-1	Structures of donor-acceptor-donor EDOT-benzobisthiadiazole and thiadiazole-quinoxaline monomers. ....	112
4-2	Electrochemical polymerization of BEDOT-BBT on Au button in TBAP/ACN and on Au/Kapton in TBAP/PC. ....	114
4-3	Electrochemical polymerization of BEDOT-TQ-Me <sub>2</sub> and BEDOT-TQ-Hx <sub>2</sub> on Au button in TBAP/ACN. ....	115
4-4	Anion radical structures demonstrating the hypothetical mechanism of the reductive doping of PBEDOT-BBT. ....	117
4-5	Reductive cyclic voltammograms of PBEDOT-BBT, PBEDOT-TQ-Me <sub>2</sub> and PBEDOT-TQ-Hx <sub>2</sub> on Au button. ....	119
4-6	Cyclic voltammograms, capacitances as a function of applied potential and charge densities as a function of time of varying amounts of PBEDOT-BBT. ....	122

4-7	Cyclic voltammograms, capacitances as a function of applied potential and charge densities as a function of time of varying amounts of PBEDOT-TQ-Me <sub>2</sub> .....	123
4-8	Cyclic voltammograms, capacitances as a function of applied potential and charge densities as a function of time of varying amounts of PBEDOT-TQ-Hx <sub>2</sub> .....	124
4-9	Stability of n-doping of PBEDOT-BBT, PBEDOT-TQ-Me <sub>2</sub> and PBEDOT-TQ-Hx <sub>2</sub> in TBAP/ACN.....	127
4-10	Expanding cell voltage of Type IV supercapacitor by combining PProDOP with PBEDOT-TQ-Me <sub>2</sub> . .....	129
4-11	Cyclic voltammograms, capacitances as a function of applied potential and charge densities as a function of time of PBEDOT-BBT and corresponding devices. ....	130
4-12	Cyclic voltammograms, capacitances as a function of applied potential and charge densities as a function of time of PBEDOT-TQ-Me <sub>2</sub> and corresponding devices .....	131
4-13	Cyclic voltammograms, capacitances as a function of applied potential and charge densities as a function of time of PBEDOT-TQ-Hx <sub>2</sub> and corresponding devices. ....	132
4-14	Stabilities of Type IV supercapacitors of PBEDOT-BBT, PBEDOT-TQ -Me <sub>2</sub> and PBEDOT-TQ-Hx <sub>2</sub> in TBAP/ACN.....	135
5-1	Electrochemical deposition of RuO <sub>x</sub> ·nH <sub>2</sub> O on bare SWNTs film and PProDOP Sticky-PF SWNTs substrate .....	140
5-2	Peak current densities of RuO <sub>x</sub> ·nH <sub>2</sub> O deposition on bare SWNTs film and PProDOP Sticky-PF SWNTs substrate .....	142
5-3	Cyclic voltammograms and capacitances as a function of applied voltage of PProDOP on Sticky-PF SWNTs in LiBTI/ACN and in 0.5M H <sub>2</sub> SO <sub>4</sub> .....	143
5-4	Cyclic voltammograms and capacitances as a function of applied potential of RuO <sub>x</sub> ·nH <sub>2</sub> O on bare SWNTs film and PProDOP Sticky-PF SWNTs substrates .....	144
5-5	Cyclic voltammograms and charge densities as a function of time of PProDOP before the RuO <sub>x</sub> ·nH <sub>2</sub> O deposition and the composite films .....	147
5-6	Capacitances of the composite as a function of the initial capacitance of PProDOP .....	148
5-7	Capacitances of the RuO <sub>x</sub> ·nH <sub>2</sub> O as a function of the initial capacitance of PProDOP ...	149
5-8	Scanning electron micrographs of RuO <sub>x</sub> ·nH <sub>2</sub> O on bare SWNTs film and PProDOP Sticky-PF SWNTs substrates. ....	151
5-9	XPS survey scans of RuO <sub>x</sub> ·nH <sub>2</sub> O PProDOP Sticky-PF SWNTs film and PProDOP Sticky-PF SWNTs films. ....	153

5-10 Cyclic voltammograms and capacitances as a function of applied potential of TYPE I  
Hybrid  $\text{RuO}_x \cdot n\text{H}_2\text{O}|\text{PProDOP}$  supercapacitor with Sticky-PF|SWNTs substrates.....154

Abstract of Dissertation Presented to the Graduate School  
of the University of Florida in Partial Fulfillment of the  
Requirements for the Degree of Doctor of Philosophy

DIOXYPYRROLE BASED SUPERCAPACITORS FOR ENERGY STORAGE

By

Merve Ertas

August 2009

Chair: John R. Reynolds

Major: Chemistry

This work details the application of conjugated polymers, particularly poly(3,4-propylenedioxy pyrrole) (PProDOP), to supercapacitor devices. The oxidation and reduction (redox) processes in electroactive polymers make it possible to use them as charge storage materials. Within this work, a detailed electrochemical and morphological characterization of PProDOP on varying electrode substrates was conducted. In the first study, devices based on PProDOP on Au electrodes were introduced with outstanding long-term stabilities (~20% loss after 37,000 switches). The use of single walled carbon nanotube (SWNT) films with porous 3D network structures were used, for the first time, to realize the interpenetration polymer into the SWNT matrix it, leading more material loading per unit area in the supercapacitor. A novel electrode design created by non-covalent modification of the surface of SWNT films with a pyrene functionalized polyfluorene has been demonstrated as a compatibilizer between the nanotube film surfaces and conducting polymers. A significant areal capacitance improvement (3 fold) has been observed with electrodes containing porous substrates over conventional non-porous flat metalized substrates. Any type of supercapacitor device utilizing varying charge storage materials can benefit from this method.

The key to achieving higher energy densities in an electrochemical supercapacitor is to expand the cell voltage as the energy stored scales with the square of this variable. For this purpose, a new family of n-dopable electroactive polymers, based on a donor-acceptor-donor design along with PProDOP were utilized in Type IV supercapacitors. The operating voltage ranges of the devices were enhanced up to 3V.

A novel device design utilizing a composite of conducting polymer and hydrous ruthenium oxide as the charge storage material in Type I supercapacitors was introduced. A two step all electrochemical method for preparation of interpenetrating PProDOP and hydrous ruthenium oxide composite was demonstrated. This method allows 100% increase in capacitance per unit area, of ruthenium oxide deposited on PProDOP compared to bare SWNT films. Capacitance contributions of each of the composite material to the total capacitance were also confirmed.

## CHAPTER 1 INTRODUCTION

### **Historical Background**

Electrical charge storage is based upon principles that were discovered in the mid-eighteenth century, with the observation of phenomena associated with ‘static electricity’ and is hence about 200 years old. The discovery of the “Leyden Jar” by Musschenbroek in 1745 represented the first capacitor and was of fundamental importance in the study of electricity.<sup>1</sup> Although electrostatic capacitors have been widely used in energy storage for nearly a century, their low capacitance values have traditionally limited their applications. The concept of storing relatively large quantities of electrical energy (compared to the energy density of batteries) at the interface between a metal and an electrolytic solution in reasonably small capacitors was first proposed in 1957 by Becker at General Electric when a patent was issued for an electrolytic capacitor using porous carbon electrodes.<sup>2</sup> Although the mechanism was unknown at that time, the device exhibited exceptionally high capacitance and it was mentioned that the energy was being stored in the pores of the carbon. In 1966, researchers at The Standard Oil Company, (SOHIO) rediscovered the same effect using the double-layer capacitance of high area carbon materials in non-aqueous electrolyte solution and patented a capacitor consisting of two layers of activated charcoal separated by a thin porous insulator where the energy stored in the double layer.<sup>3</sup> This basic design remains the basis of today’s modern electric double-layer capacitors. In 1970, SOHIO patented a disc-shaped capacitor utilizing a carbon paste soaked in electrolyte; however, unsuccessful sales led SOHIO to license their technology to the Nippon Electric Company (NEC).<sup>4</sup> Eight years later, NEC, produced the first commercially successful double-layer capacitors designed to provide backup power for maintaining computer memory. The term ‘supercapacitor’ was the trade name of this device, and continues to be in common usage today.<sup>5</sup>

A different principle was proposed and developed between 1975 and 1981 by Conway in Ottawa.<sup>6</sup> In this proposal, the concept of energy storage was based on pseudocapacitance associated by electrochemical adsorption of H or monolayer levels of electrodeposition of some base metals (Pb, Bi, Cu) at Pt or Au.<sup>7</sup> Solid oxide redox systems ( $\text{RuO}_x$ ) were also utilized as pseudocapacitance materials and were found to approach almost ideal capacitive behavior.<sup>8,9</sup> This work was continued by the Pinnacle Research Institute (PRI) and the first high-power double-layer capacitors, known as ‘ultracapacitors’ were produced for the US military applications including laser weaponry and missile guidance systems.

These developments toward the use of high surface area carbon, or metal oxide redox systems, continued as the market expanded, and by 1980’s numerous manufacturers were commercially producing high-capacitance electrochemical capacitors. Examples include “The Gold Capacitor” developed by Panasonic (Matsushita Electric Industrial Co., Osaka, Japan) and the double-layer capacitors produced by ELNA under the name “Dynacap”. This was followed by a study by the United States Department of Energy (DoE) to explore the use of capacitors in the context of hybrid electric vehicles, and by 1992 the DoE Ultracapacitor Development Program was underway at Maxwell Laboratories.<sup>10</sup> In 2005, the supercapacitor market was estimated between US \$270 to \$400 million<sup>11</sup> and continues to grow through improved performance and drastic reduction in cost. Today, various supercapacitors are being manufactured worldwide for applications that require rapid recharging, high power output, and repetitive cycling.

The high capacitance systems described have been labeled with a variety of names, many of which are unique to the particular manufacturer. Recently, however, the technical literature appears to have agreed upon a universal term proposed by Burke: “electrochemical capacitors”,

to refer to systems based on the double layer or pseudo-capacitances. Within this dissertation, the technology will also be referred as supercapacitor, a term will be used interchangeably with electrochemical capacitors.

### Operation Fundamentals

Batteries, fuel cells and capacitors have many features in common, and are all based on electrochemical principles. The energy obtained from any energy storage and conversion device depends strongly not only on the device but also on the power output. The so-called “Ragone plot” shown in Fig 1-1, visualizes the graphical comparison of the power density and energy density performance characteristics of various energy storage devices.<sup>1, 12, 13</sup>

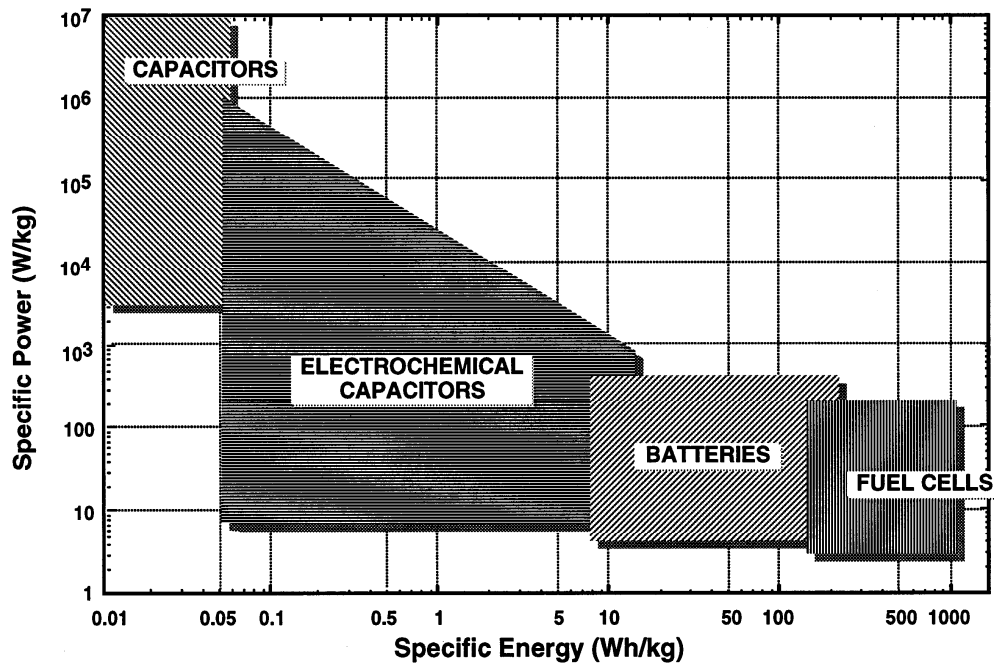


Figure 1-1. Ragone plot, in which the energy density (Wh/kg) is plotted against the power density (W/kg), of various energy storage devices. [Reprinted from *Electrochimica Acta*, 45/15-16, R. Kotz and M. Carlen, “Principles and applications of electrochemical capacitors”, pages: 2483-2498, Copyright (2000), with permission from Elsevier]

Batteries are typically high energy, low power devices, whereas conventional capacitors such as electrolytic capacitors or metalized film capacitors are higher power density devices with

limited energy storage capabilities. The quality of the energy obtained from conventional capacitors is generally poor due to variation of the voltage delivered with the state of discharge, whereas batteries tend to have a fairly constant output voltage. Fuel cells can have high energy storage, but their power output is limited. As demonstrated in Fig 1-1, electrochemical capacitors' properties fill the gap in energy storage devices capabilities that was previously vacant. This is important as, electrochemical capacitors have the ability to store more energy than conventional capacitors; yet, they are able to deliver more power than batteries. When used in combination, these devices can improve battery performances, as well as capacitor performances, in terms of power density or energy density, respectively.

### **Comparison of Energy Storage in Capacitors and Batteries**

There are two fundamental ways electrical energy can be stored: (i) directly, as negative and positive electric charges on the plates of a capacitor in electrostatic fashion and (ii) indirectly, as in batteries by Faradaic oxidation and reduction of the electrochemically active species.

When ions, or electrical charges, are released by the electrochemically active species going under redox process in a battery, they migrate from one electrode into the electrolyte, and a corresponding number of ions from the electrolyte are stored through another redox combination in the other electrode. The transfer and storage of ions does the electric work, while the current and resulting electrical potential produce the voltage difference across the poles of battery cells. Accordingly, the energy storage capability of a battery at a given electrochemical potential is directly proportional to the number of ions that can be absorbed in the electrodes.

The useable energy stored electrochemically in a battery is given as  $QV$ , where  $V$  is the voltage of the cell and  $Q$  is the cell charge capacity, the electrical charge transferred to the load during the chemical reaction. During discharging of an ideal battery cell exhibiting a Nernstian

cell potential, progressively increasing charge is being added at a relatively constant voltage which remains ideally constant until all reactant materials have been electrochemically consumed.

On the other hand, the energy storage phenomenon in a capacitor is based on charge separation, which is quite different than in batteries. The simplest conventional capacitors store energy in the form of electrical charge in a thin layer of dielectric material supported by metal plates that act as the terminals for the device. The current is a result of electron accumulation on one electrode and depletion on the complementary electrode rather than ion transfer. Positive and negative electrostatic charges physically reside at the surface of the plates. The electrical field is what generates the voltage, rather than an electrochemical potential.

The capacitance  $C$  is a measure of the energy storage capability expressed in Farads (F). It is given by the following Equation 1-1, which relates the amount of charge that can be stored in relation to the strength of the applied potential;

$$C = Q/V = \epsilon \epsilon_0 A/d \quad (1-1)$$

where  $V$  (V) is the voltage difference between the terminal plates and  $Q$  (Coulombs) is the charge accumulated on each plate. As it is also shown in relation to the geometrical dimensions of a capacitor, the capacitance depends on the dielectric constant,  $\epsilon$  and the thickness,  $d$  of the dielectric material or the separation distance between parallel plates and its geometric area,  $A$ , where  $\epsilon_0$  is the permittivity of free-space ( $8.854 \times 10^{-12}$  F/m). Often in the cases of double-layer and pseudo-capacitance,  $C$  is not constant with changing  $V$ , therefore a differential capacitance is defined as  $C = dq/dV$ . The charge density of a capacitor is described by  $Q/A$  and the maximum voltage that can be achieved by a dielectric capacitor is dependent on the breakdown

characteristics of the dielectric material. The storable energy in a capacitor charged to a potential difference of  $V$  can be calculated as

$$E = \frac{1}{2} CV^2 = \frac{1}{2} QV \quad (1-2)$$

for an accumulated charge  $Q$  residing on plates of the capacitor. During charging of a capacitor, work is being continuously done against the charges being accumulated on the electrodes, therefore the voltage progressively rises in the charging process. This phenomenon explains the fact that the energy stored in the capacitor is half the value of the equivalent charge stored in a battery where energy scales as  $QV$ . For a usual separation distance of  $10^{-4}$ m and a dielectric materials having  $\epsilon \cong 100$  ( $\epsilon_{\text{water}} = 78$  at 298K), the capacitances are very small, on the order of pF calculated due to the Equation 1-1.<sup>14</sup> It is convenient to discuss the energy storage mechanism in electrochemical capacitor in terms of double-layer capacitance and pseudocapacitance separately due to the fundamental differences between these two principal types of supercapacitors.

### **Electric Double-Layer Capacitance**

Similar to conventional electrostatic capacitors, charge storage in electric double layer capacitors (EDLCs) is largely electrostatic in nature. Instead of charges accumulating on two conductors separated by a dielectric as in conventional capacitors, the charge accumulates in the double-layer formed at the interface between the solid electrode material surface and an electrolytic solution in the micropores of the electrodes.<sup>15</sup> A schematic of an EDLC is shown in Fig 1-2. When an electric potential is applied across the electrodes, one layer forms on the charged electrode, and the other layer comprised of ions forms in the electrolyte giving rise to the double layer formation. The thickness of double layer or the separation of charges is very

small, on the order of several Angstroms. An estimate of the specific capacitance of such a double-layer can be obtained using Equation 1-3.

$$C/A = \epsilon/4\pi\delta \quad (1-3)$$

where  $C$  is the capacitance,  $A$  is the surface area,  $\epsilon$  is the relative dielectric constant of the medium between the two layers (the electrolyte), and  $\delta$  is the distance between the two layers (the distance from the electrode surface to the centre of the ion layer).<sup>4</sup> In terms of the charges  $\Delta q$  that are accumulating across electrode electrolyte interphase to extents the potential difference built up across the interphase,  $\Delta V$ , the double layer capacitance can be expressed as  $C = \Delta q / \Delta V$  or  $d(\Delta q) / d(\Delta V)$ .

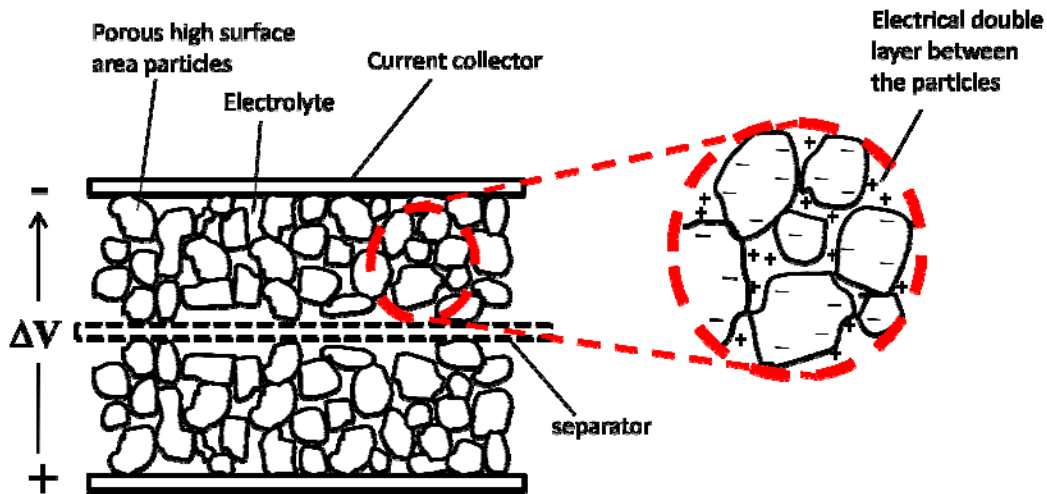


Figure 1-2. Schematic of a electrical double-layer supercapacitor. [Adapted from Journal of Power Sources, 91/1, A. Burke, "Ultracapacitors: why, how, and where is the technology", pages 37-50, Copyright (2000), with permission from Elsevier]

EDLCs are constructed by two electrodes immersed in an electrolyte with an ion permeable separator placed between the electrodes in order to prevent electrical contact, but still allow ions from the electrolyte to pass through. The ions in the pores of the active material create the double layer by diffusion. As a result, at each electrode/electrolyte interface, there is

one double-layer present. In addition to the capacitance that arises from the separation of charge, sometimes a small Faradaic contribution to the double-layer capacitance can be made from electrochemical surface reactions (e.g. reversible surface quinonoid-type redox reactions or chemisorption processes) that can occur on the surface of the carbon electrode.<sup>14</sup> Since the thickness of the double layer is very small, a fraction of a nm, capacitance values of 15–50  $\mu\text{F}/\text{cm}^2$  are possible with the EDLCs. Moreover, by utilizing high surface area of materials ( $\sim 1000 \text{ m}^2/\text{g}$ ), large capacitances of 150–300 F/g are practically attainable.<sup>16-21</sup> Since the double layer capacitance does not involve any phase transition mechanism as in batteries, charging/discharging is highly reversible, rapid and hundreds of thousands of cycles are typically achievable with a given element of charge being able to be admitted or withdrawn at virtually the same potential.<sup>14</sup>

### **Pseudocapacitance**

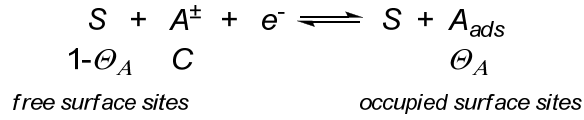
Pseudocapacitance arises from Faradaic charge transfer process occurring at the surface or in the bulk near the surface of the electrode material to an extent limited by a finite quantity of reagent or of available surface. The potential at which charge is being passed is a function of the charge accumulated. Unlike ideal Nernstian behavior in batteries, where a constant electrode potential is independent of the extent of the reaction, in the pseudocapacitance process, the extent of Faradaically admitted charge depends linearly, or approximately linearly, on the applied voltage. In other words, the charge transfer leading to passage of extent of charge,  $Q$  is voltage dependent. Consequently, a capacitive phenomenon occurs which is not electrostatic in origin as in double-layer capacitance, and is denoted as ‘pseudo’ in order to differentiate it from electrostatic capacitance. The systems utilizes pseudocapacitance provide a transition between electrochemical battery-cell and double layer electrostatic charge and energy storage.

Pseudocapacitance occurs when the extent of reaction,  $Q$  is some continuous function of potential, so that a derivative  $dQ/dV$  arises that has the properties of a capacitance. There are two types of electrochemical reactions that can involve a charge transfer that is voltage dependent, giving rise to pseudocapacitance. These include adsorption pseudocapacitance, resulting from a process of progressive occupation of surface sites on an electrode by ions from the electrolyte, and also from redox pseudocapacitance associated with the redox processes involving ions from the electrolyte where the electrode potential  $E$  of a redox system is a logarithmic function of the ratio of activities of the oxidized and reduced species. Both of these two processes are principally surface mechanisms; hence are highly dependent on the surface area of the electrode material. The redox pseudocapacitance can also arise from the oxidation or reduction followed by charge neutralization of active conducting polymer material in the electrode which is more of a bulk process. Although the surface area of these materials is not that critical for high capacitance values, relatively high surface area with micropores is required for the insertion and expulsion of ions from the electrolyte to the matrix. All the processes leading to an experimentally accessible pseudocapacitance require high electronic conductivity of electrodes in order to distribute and collect the electron current. Both adsorption and redox pseudocapacitances will be explained in more detail in the following sections.

### **Adsorption pseudocapacitance**

Two-dimensional surface deposition of ions to form a monolayer on the electrode substrate is the best example of reversible process that results in a Faradaic charge transfer, and is hence associated with pseudocapacitance. These processes can give rise to almost one hundred times greater capacitance than the double-layer capacitance at the same electrode. Reversible deposition/desorption of H at Pt, Rb and Ir, or deposition/desorption of Pb and Bi atoms on Au

or Ag are good examples of two-dimensional Faradaic electrode processes. These adsorption and desorption process can be expressed as follows:



where  $S$  is the electrode substrate (usually a noble metal),  $C$  is the concentration of the ionic species  $A$ , “ $1-\theta_A$ ” is the fractional free surface area available for adsorption at a coverage,  $\theta_A$ .<sup>22</sup>

$$\frac{\theta_A}{1-\theta_A} = K \cdot \exp\left(-\frac{VF}{RT}\right) \quad (1-4)$$

The fractional coverage can be determined by using Equation 1-4, for an equilibrium situation at any potential where it assumed that sites are occupied randomly in a fixed lattice; where  $K$  is an electrochemical equilibrium constant. This relation shows the dependence of the extent of fractional coverage  $\theta_A$ , proportional to charge passed, on the electrode potential,  $V$ .

Since  $\theta_A$  is proportional to charge passed and  $\theta$  is a function of  $V$ , then  $d\theta_A/dV$  is proportional to corresponding capacitance. If  $Q_1$  is the amount of charge required for formation or dispersion a complete monolayer, then a pseudocapacitance can be derived by differentiating Equation 4 with respect to  $V$ , giving,<sup>14</sup>

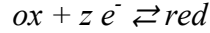
$$C = Q_1 \frac{d\theta_A}{dV} = \frac{Q_1 F}{RT} \frac{K \pm \exp\left(-\frac{VF}{RT}\right)}{\left[1 + K \pm \exp\left(-\frac{VF}{RT}\right)\right]^2} \quad (1-5)$$

According to Equation 1-5 and cyclic voltammetry experimental results, these adsorption/desorption process are highly reversible with respect to changes of scan rate ( $dV/dt$ ) from negative to positive values, giving mirror-image voltammograms. Since only two-dimensional arrangement are involved in adsorption/desorption process without any phase change or reconstruction mechanisms, the capacitance versus voltage profile is stable and

repeatable over thousands of cycles in a clean solution and can be maintained up to quite high sweep rates of 100 V/s.

### Redox pseudocapacitance

A general redox reaction involving any oxidized (*ox*) and reduced (*red*) species can be simply expressed as



and the equilibrium redox potential of this reaction is given by the Nernst equation,

$$E = E^\circ + \frac{RT}{zF} \ln \frac{[ox]}{[red]} = E^\circ + \frac{RT}{zF} \ln \frac{\frac{[ox]}{[ox+red]}}{1 - \frac{[ox]}{[ox+red]}} = E^\circ + \frac{RT}{zF} \ln \frac{\mathfrak{R}}{1-\mathfrak{R}} \quad (1-6)$$

where  $E^\circ$  is the standard potential,  $R$  is the gas constant,  $T$  is the absolute temperature,  $F$  is the Faraday constant, and  $[ox]$  and  $[red]$  are the concentrations or the activities of oxidized and reduced species, respectively. The concentrations of the active species can also be expressed as their relative fractions, “ $[ox]/([ox]+[red])$ ” and “ $[red]/([ox]+[red])$ ” or “ $1-[ox]/([ox]+[red])$ ” so that Nernst equation can be rewritten which is also shown in Equation 6.

When  $\mathfrak{R}$  is defined as “ $[ox]/([ox]+[red])$ ”, the analogy between  $(\mathfrak{R}/1-\mathfrak{R})$  and  $(\theta_A/1-\theta_A)$  in Equation 4, is obvious. Thus, redox pseudocapacitance is formally analogous to an electrochemical adsorption capacitance with charge transfer. The amount of charge required to convert a given quantity of “*ox*” to “*red*” or vice versa, is given by the product of  $z$  and  $F$  and as it can be clearly seen from the Nernst equation, it is a function of the potential  $E$ . If Equation 6 is rearranged as the following, it takes the form of Equation 1-4.

$$\frac{\mathfrak{R}}{1-\mathfrak{R}} = \exp \frac{(E-E^\circ)zF}{RT} = \exp \frac{\Delta E z F}{RT} \quad (1-7)$$

Therefore, differentiation of Nernst equation produces a pseudocapacitive expression, having the same relation to potential as in the Equation 1-5.<sup>14</sup>

Similar pseudocapacitive behavior arises in the case of intercalation processes (e.g., lithium intercalation into layer-lattice host materials). The equation for these reactions has the same form as in Eq 1-4 and Eq 1-7 with the conversion of the logarithmic portion including the three-dimensional site fraction occupancy by the intercalated guest atom or ion (e.g.,  $\text{Li}^+$ ).  $\text{Li}^+$  batteries can be regarded in some sense as pseudocapacitors since their extents of charge are a continuous function of voltage, although their response times in a capacitive sense are longer.<sup>23</sup>

## **Electrode Materials**

### **Carbon**

Since the early years of the supercapacitor development, a substantial fraction of EDLCs have relied on carbonaceous materials, which remain the most popular electrode material today. Carbon has been an attractive choice due to its low cost, availability, and long term history of use. Although carbon has now been used in EDLCs for over 20 years, the mechanisms of energy storage and the relationships between the quantified specific capacitances and the morphological properties of the different carbon materials have been studied in depth only relatively recently.

It is necessary for the carbon materials to have high surface areas, on the order of 1000  $\text{m}^2/\text{g}$  and good intra and inter particle conductivity in porous matrices to be optimal for today's state of the art supercapacitors.<sup>12, 13, 24, 25</sup> Although surface area and capacitance can generally be increased by increasing porosity of the carbon materials, the specific capacitance is not necessarily directly proportional to the surface area of the electrode.<sup>26</sup> High specific capacitances are achievable with EDLCs due to their high electrode/electrolyte interface area and a small charge layer separation of atomic dimensions. Charge is stored in the pores at or near the interface between the active carbon material and the electrolyte. If electrolyte ions can not access the pores, the surface area will not contribute to the specific capacitance. Therefore, the

electrolyte accessibility to intrapore surface area is what ultimately influences the capacitance, rather than simply a high surface area. As a consequence, the way the surface is developed greatly influences the specific capacitance value that can be obtained from carbon materials. The mobility of ions in the electrolyte solution within the pores is significantly influenced by pore size. The key factor in designing carbon electrodes is to attain the best pore size related to the electrolyte ion size, which will maximize the specific capacitance. In this regard, many research groups have studied the ways to control porosity in the mesoporous range (2 to 10 nm) to maximize the capacitance.<sup>27-30</sup> In contrast to the traditional view of linear dependence of the capacitance on the pore size, recently it has been demonstrated that even micropores of less than 2 nm, which are smaller than the size of solvated electrolyte ions can contribute to the charge storage mechanism.<sup>31-34</sup> This phenomena is explained by the distortion of the solvation shell of the ions as they enter to the narrower pores (<1 nm) leading to closer distance of the ion to the carbon surface so thus enhanced capacitances are achieved.

In addition to surface area and porosity, the conductivity of carbon electrodes is of substantial importance to the power density of EDLCs. The conductivity of the electrodes is inversely proportional to the particle size of the carbon materials. The electrodes with high surface area that are made of smaller particles usually show increased resistances, and thus lower power densities. However, using larger particle sized materials will limit the specific energy due to the reduced surface area. In conclusion, a vital aspect in the fabrication of carbon electrodes for supercapacitors is to compromise between the pore-size distribution to ensure easy access of electrolyte ions, or the specific surface area to ensure high capacitance, and the particle size to achieve good conductivity.<sup>35</sup> In its more dispersed and conducting forms, carbon electrodes can take many different manufactured forms that can be utilized in EDLCs, such as foams, fibers,

and nanotubes, all of which are nanoporous material.<sup>36</sup> EDLCs fabricated using such electrodes in conjunction with both aqueous and organic electrolytes have demonstrated capacitances between a few Farads to several thousand Farads per cell.<sup>37</sup> Several representative technologies available today are briefly explained below.

### **Activated carbons**

Activated carbons are the most extensively used material in the fabrication of EDLCs due to their high surface area and relatively low cost. Traditionally, these high specific area carbons are in powder or fiber form which gives rise to good mechanical reliability and electrical conductivity, both of which are useful for EDLCs applications. Activated charcoal is a powder made up of extremely small and very rough particles, which in bulk form a low-density volume of particles with holes between them resembling a sponge. Treatment of carbon materials has a significant effect on the structure of the electrode morphology in terms of surface size and porosity. The capacitance varies depending on the process used to prepare the carbon electrode. High surface area electrodes with the randomly sized porous networks are obtained by activation processes. The resulting overall accessible surface area of even a thin layer of activated carbon is in the range of 1000-2000 m<sup>2</sup>/g which is many times greater than the geometrical surface area of the electrode, allowing many more electrons to be stored in any given volume. Activated carbon powders usually require binders to be processed into electrode films. These inactive components occupy a significant fraction of the total electrode weight which results in low energy densities. The capacitances of these materials are about 100 F/g and 50 F/cm<sup>3</sup> using inorganic electrolytes. In contrast to powders, activated carbon fabrics can be used without any binder addition. Although they have high surface areas compared to activated carbons and high electrical conductivity (200-1000 S/cm), the high cost restricts their use in EDLCs to very specific applications.

## **Carbon aerogels**

Besides activated carbons, recently nanostructured carbons, such as aerogels<sup>38</sup>, nanotubes<sup>17</sup> and nanotemplates<sup>39</sup> have been the focus of attention to be used as electrode materials in EDLCs. Aerogels are low-density suspensions of carbon nanoparticles within a gel in which the liquid component of the gel has been replaced with gas. A pyrolysis treatment in an inert atmosphere leads to a controlled and uniform particle and pore sized (mesoporous between 2 and 50 nm) carbon aerogels with a good electrical conductivity (several S/cm).<sup>35</sup> Although, the usable surface areas of carbon aerogels (400-900 m<sup>2</sup>/g) are usually lower than the activated carbons, the advantages of these materials are mainly their low ionic and electronic charging resistance due to the ordered and interconnected pore structure, which leads to high specific power. Specific capacitances in the range of 50 -100 F/ g have been reported in the literature for these materials.<sup>36</sup> Since the use of binding materials in the carbon based electrodes greatly reduces the conductivities, the fact that aerogels can be used without binding material makes them an attractive supercapacitor electrodes material. In addition to power performance, capacitance and cyclability of EDLCs are improved by replacing the activated carbons with carbon aerogel electrodes.

## **Carbon nanotubes**

Carbon nanotubes have recently become a new choice of electrode material to be used in EDLCs due to their unique architecture and remarkable characteristics such as high specific surface area, unique pore structure, excellent electrical conductivity and interconnectivity, chemical stability and low mass density.<sup>17, 40</sup> They can be produced as single walled (SWNTs) or multi walled carbon nanotubes (MWNTs) depending on the synthesis route, and both are actively being researched as supercapacitors electrode materials. Capacitance values from 20 to 180 F/g have been reported depending on the purity of carbon nanotubes and the electrolyte.<sup>21, 36, 41-46</sup> To

improve these values, significant efforts have been focused on surface functionalization of nanotubes; however, the results are still not impressive and cycling stability is a problem.<sup>35</sup> Recent trends in nanotube-based supercapacitor research involve the nano-engineering of microscopic forests of dense, nano-ordered, and vertically aligned nanotubes to the current collector. Such carbon nanotube based electrodes, analogous to a paintbrush, as opposed to a sponge as in activated carbon electrodes, could help increase capacitance by maximizing the accessible surface area through modification inter-tube distances.<sup>47-49</sup>

### **Metal Oxides**

Metal oxides are attractive electrode materials, and are utilized in supercapacitors due to their high specific capacitance and low resistance.<sup>12, 13, 24, 50, 51</sup> Application of metal oxides in pseudocapacitance research has been started with ruthenium oxides. However, this material is a noble metal and far too expensive for many commercial applications. Most of the early work on ruthenium oxides was carried out for military applications, where cost was of less concern than military capability. The charge storage process in ruthenium dioxide electrodes is surface limited and progresses in several one electron steps, resulting in broad range of capacitance values. Thus, a constant pseudocapacitance occurs over the full operating voltage range. Subsequent to crystalline ruthenium oxide, the use of hydrous ruthenium oxide as an electrode material was investigated and specific capacitance of 750 F/g was found with an aqueous electrolyte sulfuric acid solution.<sup>14</sup> The US Army Research Lab has assembled prototype cells with an impressive energy density of 8.5 Wh/kg and a power density of 6 kW/kg.<sup>15</sup>

Since, high capacitance and fast charging result from H adsorption, metal oxides electrodes must be used with acidic aqueous electrolytes to provide good proton conductivity. This narrows the achievable cell voltage and moreover, most metal-oxides break down rapidly in acidic solutions. Although the high cost of ruthenium prevents its large-scale use, the best charge

storage capability of any capacitor reported to date have been 840 F/g (200Wh/kg) and 500 mF/cm<sup>2</sup> with hydrous ruthenium oxides in an aqueous electrolyte sulfuric acid solution. In addition to the high power densities and the almost constant capacitance over a wide voltage range, it shows an excellent reversibility with a cycle life over several hundred-thousand cycles.<sup>16, 52-58</sup>

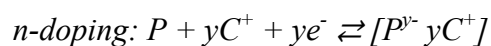
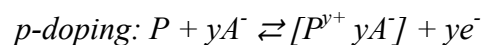
Current academic efforts are focused on other lower-cost metal oxides to be utilized in more practical supercapacitors. Recently, some materials used in batteries such as manganese-oxides and vanadium oxides have attracted attention for application in pseudocapacitors due to their lower cost and encouraging specific capacitances.

The interest in manganese oxides for electrochemical energy storage has shown a steady and continuing growth since 2000. Specific capacitances of amorphous manganese oxides powders were reported as 200 F/g in aqueous electrolytes.<sup>59, 60</sup> Although these capacitance values are lower than ruthenium-oxides, the interest in manganese oxides for energy storage applications is driven by their low cost and low toxicity as a practical alternative to other metal oxides. Moreover, it has been shown that milder aqueous electrolyte solutions such as potassium chloride can be used with manganese-oxides. Vanadium oxides are another class of metal oxides that draw attention as a low-cost alternative to ruthenium oxides for supercapacitor applications. They exhibit a broad range of morphologies, on which the electrochemical characteristics are strongly dependent and their discharging curves demonstrate typical capacitive-like behavior.<sup>61, 62</sup> These materials are likely contenders for a number of future commercial supercapacitor applications.

### **Conducting Polymers**

Another interesting class of materials that demonstrate pseudocapacitance with highly reversible behavior is the family of conducting polymers.<sup>14, 63-65</sup> Conducting polymers store and

release charge through the redox process. Typically oxidizing or reducing and neutralization of these compounds is referred to as doping and dedoping, respectively. Conducting polymers can be doped and dedoped rapidly to high charge densities. During the oxidation and reduction process, charge is removed from or transferred to the polymer, respectively creating electron deficiency (p-doping) or excess of electrons (n-doping) on the backbone as delocalized  $\pi$ -electrons. Consequently, the appropriate counter ions from the electrolyte enter into the polymer to compensate the charge created on the backbone, which is referred as doping. These two types of doping processes are shown below:



When neutralization occurs, the ions are released back into the electrolyte solution, referred to as dedoping, or neutralization. Doping of conducting polymers takes place throughout the bulk volume of the material, rather than just at the outer surface of particles as is the other cases for electrochemical capacitances. Since the entire volume of the polymers is involved in the charge storage process, high levels of capacitive energy densities can be achieved with polymer films. Conducting polymers can be tailored to provide specific properties, such as high conductivity, flexible morphologies, wide voltage windows, high storage capacity, porosity, and reversibility. Moreover, conducting polymer materials can be easily and economically made in large amounts. Although, conducting polymer systems are less stable than ruthenium dioxides, due to the phenomenon of swelling and shrinking during doping and dedoping processes<sup>12</sup>; they still demonstrate stabilities over thousands of cycles with wide voltage ranges<sup>66</sup>, and are much lower-cost than ruthenium oxides. Another advantage of conducting polymer systems is that their redox capacitance are not diffusion limited in terms of the oxidized and reduced species

since they are not solution species but they are physically anchored on the electrode surface. Thus, rapid charging and discharging giving high power densities is possible. In terms of satisfactory energy and power densities, cycle life, low weight and thermal stabilities with the predicted low material cost relative to the other materials that were traditionally used, conducting polymers represent an attractive material currently available to be used in electrochemical capacitors.

Characteristically, conducting polymers offer specific capacitances in the range of about 100-250 F/g.<sup>16, 67-72</sup> As initial work in this field, a prototype polymer film capacitor with an energy density of 39 Wh/kg and a power density of 35 kW/kg has been demonstrated by the Los Alamos National Laboratory.<sup>63</sup> Over the years, several supercapacitors have been fabricated using polyaniline, polythiophene, polypyrrole, and their derivatives with different electrolyte and substrate systems to achieve high energy storages with high capacitances.

Conducting polymers were originally generalized using three schemes in which they can be utilized in electrochemical capacitors by Rudge *et al.* These were referred as Types I, II and III.<sup>73</sup> In Fig 1-3, a general diagram of a supercapacitor utilizing conducting polymers as anode and cathode electrodes is shown. Among these, Type I and II supercapacitors utilize only p-doping conducting polymers for both positive and negative electrodes. A Type I device is based on a symmetric configuration with the same p-dopable polymer on both electrodes, whereas a Type II device uses an asymmetric configuration with two different p-dopable polymers on each electrode. A Type III supercapacitor consists of a p-dopable polymer and an n-dopable polymer as the positive electrode and the negative electrode, respectively. This original classification of application of conducting polymers into supercapacitors is based on the increasing operating voltage range and charge storage capacity of the devices. However, there has been an ambiguity

about symmetric and asymmetric Type III supercapacitor since Type III is the only term that incorporates an n-doping polymer.<sup>74</sup> Hence, the term “Type IV supercapacitors” was later proposed to distinguish between symmetric and asymmetric devices that use an n-doping polymer. Type III refers to a symmetric configuration utilizing the same polymer that both p- and n-dopable, while Type IV supercapacitors are based on an asymmetric configuration that utilize one polymer as the p-doping and a different polymer for the n-doping on each electrode.

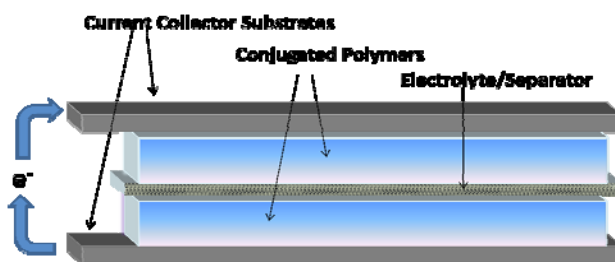


Figure 1-3. Schematic diagram of the general construction of a supercapacitor utilizing conducting polymers as anode and cathode electrodes.

### Type I & II supercapacitors

For the construction of these devices, polymers are initially set in the fully oxidized (p-doped) state and laminated with the fully neutralized forms to establish the initial charge state of the capacitor. With the discharge of the supercapacitor, neutralization of the p-doped films proceeds with concurrent oxidation of the cathode films in the device. In Type II supercapacitors, the polymer with the higher oxidation potential is used as the anode and the polymer with the lower oxidation potential serves as the cathode. Since oxidation and reduction potential of the anode and cathode are equal in Type I, at most only half of the total charge capacity of the polymer is used.<sup>14, 75, 76</sup> Type I devices usually have approximately 1V operating potential ranges. As a consequence of the difference between oxidation and reduction potential of the anode and cathode films, in Type II supercapacitors, the cell potential range is higher than Type I devices (around 1.0 to 1.25 V) and only about 75 % of the total charge capacity of the polymers can be

utilized. Type II supercapacitors benefit from the increased cell voltage, which allows them to deliver more charge. In both Type I and II cases, the cell voltages are limited by the intrinsic over-oxidation resistance of the polymers.

The representation of the separate cycling of each electrode during charging of a Type I and II supercapacitors is shown in Fig 1-4a and b, as the anode oxidizes and the cathode neutralizes. Since there is either complete or partial overlap between the voltage range during oxidation/neutralization of the anode/cathode electrodes, the cyclic voltammogram of an ideal Type I or II supercapacitor would be a rectangular plot, showing a constant current within the operating voltage window of the device.<sup>14, 75-78</sup> Furthermore, under constant current conditions, the voltage outcome of the both devices would show a linear decay in an idealized case.

Although Type I supercapacitors can be reverse biased because there is no polarity between the electrodes, a CV plot would resemble the original one. However, the charge capacity of the Type II devices will be much lower when reverse biased, and stability could be a problem since there is a polarity between the electrodes.

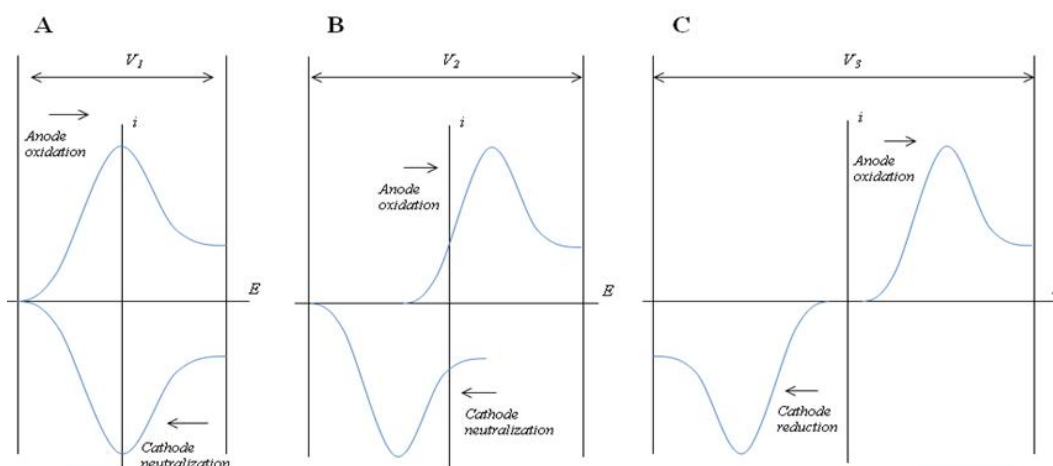


Figure 1-4. Classification of conjugated polymers in three generalized configurations in an increasing charge storage capacity and operating potential range in a) Type I, b) Type II and c) Type III supercapacitors. [Adapted from Journal of Power Sources, 47/1-2, A. Rudge, J. Davey, I. Raistrick, S. Gottesfeld and J. P. Ferraris, “Conducting polymers as active materials in electrochemical capacitors”, pages: 89-107, Copyright (1994), with permission from Elsevier].

### **Type III & IV supercapacitors**

In Type III and IV configurations, polymers are in the fully oxidized (p-doped) state on the anode and in the fully reduced (n-doped) form on the cathode electrode in the charged state of the device, while in the discharged state both polymers are in their neutral state. In Type III & IV configuration, the full total charge capacity of both anode and cathode polymers is used. Among the remaining polymer supercapacitor configurations, only the p-/n-type device configuration has the ability to outperform the conventional double-layer carbon supercapacitor. The key to achieving higher energy density in an electrochemical supercapacitor is to expand the cell voltage the energy of a capacitor scales with the square of the cell voltage ( $E = \frac{1}{2}CV^2$ ) as has been described in the previous sections. With the p-/n-type design, the operating voltage range of the devices can be increased up to 3 to 4 V, as it is shown in the representation of the charging cycle in Fig 1-4c. Hence the highest energy density can be obtained. Besides providing the broadest cell operating voltages, Type III&IV supercapacitors can deliver all the doping charge during discharge at high potentials; consequently high power densities can be demonstrated. Compared to Type I and II supercapacitors, under constant current conditions, the charge is delivered at a much higher voltage and voltage drops very rapidly after discharge.

### **Review of conducting polymer based supercapacitor literature**

Over the years, the bulk of conducting polymer based supercapacitor research has focused on polyaniline, polypyrrole, polythiophene and their derivatives with different electrolyte and substrate systems, directed toward achieving high energy storage with high capacitances. Most of this work have been evaluated for use in Type I supercapacitors.<sup>67, 68 69-72</sup>

**Polyaniline:** In addition to its usage in batteries<sup>79-81</sup>, polyaniline (PANI) is one of the most studied conducting polymers which is utilized in supercapacitors.<sup>82-87</sup> Most PANI electrodes are prepared with electrochemically grown films, as chemically synthesized PANI presents

solubility and processability limitations. These polymers operate well in both aqueous and non-aqueous electrolytes.<sup>88</sup> Very high doping levels of one electron per two monomeric units are achievable with PANI.<sup>89</sup> Supercapacitors exhibiting specific capacitances from 107 F/g<sup>85, 86</sup> to 250 F/g<sup>84</sup> have been reported for PANI. The PANI electrodes also demonstrated stabilities over 20,000 cycles with 5% loss in electroactivity.<sup>82</sup> Currently, the development of soluble polyaniline based supercapacitors were being investigated for military applications, with a focus on fast switching, improved cycle time and reduced production costs.<sup>90</sup>

**Polypyrrole:** Another conducting polymer; polypyrrole (PPy) which is also widely used for battery research, has received considerable attention for supercapacitor applications.<sup>65, 73, 91-94</sup> Specific capacitance values ranging from 40-84 F/g (100-200 F/cm<sup>3</sup>) were exhibited by PPy electrodes, using different electrolytes.<sup>82, 95-97</sup> Similar to electrochemically deposited PANI, PPy works well in aqueous and non-aqueous electrolytes.

**PolyThiophene:** Although very high capacitance values of 250 F/g were reported for polythiophene (PTh)<sup>87</sup>, because of its instability, only a limited number of research studies have focused on PThs for the energy storage applications. However, a derivative of PTh; poly(3,4-ethylenedioxythiophene) (PEDOT) which is one class of PTh derivative, has been extensively studied for use in supercapacitor electrode, due to its excellent chemical stability and fast switching speeds.<sup>78</sup> PEDOT offers specific capacitances of 210 F/g<sup>98</sup>. Energy densities of 1-4 Wh/kg with power densities of 35-2500 W/kg have been reported for PEDOTs based supercapacitors.<sup>78, 99</sup> Moreover, devices that exhibit high charge storage capability with potential window of 2.15 V have been demonstrated with PEDOT derivatives.<sup>98</sup>

Relative to Type I supercapacitors, there have been far fewer publications on Type II devices. The device performances are often reported as similar to Type I devices based on the

same polymers. The best systems reported include PPy/poly(3-methylthiophene)<sup>95</sup>, PPy/PANI devices with specific capacitance values as high as 25 F/g<sup>100</sup>, and (PEDOT)/poly(3,4-propylenedioxythiophene)<sup>77, 101</sup>. In attempts to obtain high energy and power densities, a number of research groups have focused on n-doping polymers for use in Type III and Type IV supercapacitors, allowing a wide voltage range for development of pseudocapacitance.<sup>73, 75, 76, 95, 98, 102-105</sup> Although specific capacitances of 70-180 F/g have been reached for n-doping of PTh derivatives, unfortunately, many n-doping polymers suffer from poor cycle stability<sup>105</sup>. Energy and power densities in the range of 6-39 Wh/kg and 1600-3500W/kg, respectively, were reported with these type of devices with cell voltages exceeding 3 V; however in every case cycle life was a problem. In order to eliminate the need for a stable n-doping polymer, several groups<sup>106-108</sup> have tried to use carbonaceous electrodes as the cathode electrode, referring these devices as “hybrid supercapacitors”. Another approach towards improved capacitance, energy, power and better stability is to use a combination of electroactive polymers with carbonaceous materials. Several groups have investigated electroactive polymer based composites based on PPy<sup>85, 104, 109, 110</sup>, PANI<sup>85, 111-114</sup>, and PTh.<sup>87, 107</sup>

### **Applications and Current Industry**

Commercial activity in electrochemical capacitor technology development was quite limited until 1995, due to limitations in fabrication equipment and the lack of testing procedures and standards for these devices. However, the U.S. Department of Energy (DoE) has since stimulated the development of electrochemical capacitors for commercial and other purposes through research funding and standardization of performance goals. With the increasing demand for new manufacturing techniques, novel applications with challenging power requirements, and the requirement for materials of high capacitances and low resistance, world-wide academic and commercial efforts have been focused on the many aspects of supercapacitors development.

As intermediate energy and power sources between batteries and conventional electrolytic capacitors, supercapacitors fill the gap in the energy storage technology. Their range of applications is broad, with potential uses varying from alternative power sources in diverse electronic applications such as computer power backup, medical equipment, electronic fuses, burst power for military systems, to high power applications including load leveling, electrical vehicles, space crafts, etc.<sup>12, 13, 15, 24, 97</sup>

One of the most important and large-scale applications of supercapacitors is load leveling in capacitor-battery hybridization for electric vehicle drive systems.<sup>115</sup> This application arises from the recent push toward the production of electric cars, with current rechargeable battery systems unable to satisfy increased power demands, faster charging time and lower costs. The high power capability of supercapacitors is predicted to take the main load from the battery component during acceleration, while regenerative braking systems are envisioned for partial recharging and overall energy economy. In addition to automotive applications, industrial equipment such as cranes, fork-lifts, and elevators, can gain energy efficiency from recovery of energy normally wasted during braking of repetitive motion by using supercapacitor hybrid-electric power systems. Since the Li-ion and Ni-hydrate batteries are approaching their limits for the higher power density demands, supercapacitors also present as new charge storage systems in applications where weight is a concern, such as portable consumer electronic devices.<sup>116, 117</sup> Moreover, supercapacitors are becoming important energy and power sources in military applications such as aircrafts, missiles or the portable devices such as GPS locators and night vision goggles.

There are a wide range of commercial electrochemical capacitor research and development activities in progress with different energy and power density requirements; from small

millifarad size devices up to several kilofarads size devices. When designing, fabricating and testing electrochemical supercapacitors, these power and energy density requirements of the intended application are important to take into account. Devices will be different designed for high power pulse delivery purposes such as electric vehicles, starting assist hybrid systems, than for small less demanding applications as computer memory backup, domestic electronic applications, the telecommunication systems. Parameters like power, energy, weight, volume, cycle life, cost, safety must be distinguished and assessed for different type of applications. For instance, heat management for high power charging and discharging applications or provision for overcharge protection are important concerns for larger units.<sup>118</sup>

Numerous companies around the world currently manufacture supercapacitors in a commercial capacity. The major commercial research and development activities in this field are under progress mainly in the United States, Japan, and Europe.

### **Structure of Dissertation**

The main characteristics of this work are the utilization of conjugated polymers in different supercapacitor device designs. Among conducting polymers, poly(3,4-propylenedioxyppyrrrole) (ProDOP) has been the focus of this dissertation. Chapter 2 mainly summarizes the background information of the experimental methods used throughout the dissertation and also details the supercapacitor device fabrication.

The Type I supercapacitors prepared using PProDOP were investigated in Chapter 3. Two different current collector substrates have been used in the device construction. A new concept to utilize porous 3D network structured single walled nanotube (SWNT) film as the substrate in order to achieve higher amount of capacitances per unit volume, by more material loading, is demonstrated. Moreover, the novel technique of non-covalent modification of SWNT surfaces with a pyrene functionalized polyfluorene (Sticky-PF) is introduced. By this means, carbon

nanotube film electrodes provides a significant areal capacitance improvement over conventional non-porous flat metalized substrates. Any supercapacitor utilizing varying charge storage materials can benefit from this method.

Chapter 4 details the Type IV supercapacitors utilizing PProDOP and a family of n-dopable donor-acceptor-donor systems. It evaluates the importance of n-dopability in order to increase the conjugated polymer based supercapacitor cell voltages.

Application of a composite of PProDOP and hydrous ruthenium oxide in a Type I supercapacitor configuration is demonstrated in Chapter 5. The unique electrode design allows interpenetration of metal oxide particles through PProDOP matrix. Ruthenium oxide loading per unit area were increased, accordingly, improved energy storage capabilities were realized with contributions from both PProDOP and ruthenium oxide.

## CHAPTER 2 EXPRIMENTAL TECHNIQUES

This chapter provides necessary background information of the experimental methods used throughout this dissertation. These techniques will be frequently referred to in the subsequent chapters.

### **Chemicals and Materials**

HPLC grade propylene carbonate (PC) and reagent grade acetonitrile (ACN) in Sure Seal® were purchased from Aldrich. ACN was distilled over calcium hydride before use. PC was percolated through type 3A activated molecular sieves (Aldrich), followed by fractional vacuum distillation. All solvents used on the bench were purged with Argon prior to use and were stored in Schlenk flasks under Argon.

Lithium bis(trifluoromethanesulfonyl) imide  $\text{Li}(\text{CF}_3\text{SO}_2)_2\text{N}$  or (Li-BTI), was purchased from Aldrich, and dried under vacuum at 150°C for 24 hours prior to use. Tetrabutylammonium perchlorate (TBAP) was either purchased from Aldrich or synthesized by mixing a 1:1 mole ratio of tetrabutylammonium bromide dissolved in a minimal amount of water with perchloric acid. The resulting white precipitate was filtered, recrystallized from a 1:1 molar ratio mixture of ethanol and water and dried under vacuum at 60°C for 48 hours. Poly(methylmethacrylate) (PMMA) (Mw:996,000 g/mol) was purchased from Aldrich and was dried under vacuum at 50°C for 12 h and stored under argon prior to use.

The monomers 3,4-propylenedioxy pyrrole (ProDOP),<sup>119 120</sup> 4,8-bis(2,3-dihydrothieno[3,4-*b*][1,4]dioxin-5-yl)benzo[1,2-*c*;4,5-*c'*]bis[1,2,5]thiadiazole (BEDOT-BBT)<sup>121</sup>, 4,9-bis(2,3-dihydrothieno[3,4-*b*][1,4]dioxin-5-yl)-6,7-dimethyl-[1,2,5]thiadiazolo[3,4-*g*]quinoxaline (BEDOT-TQ-Me<sub>2</sub>), 4,9-bis(2,3-dihydrothieno[3,4-*b*][1,4]dioxin-5-yl)-6,7-dihexyl-[1,2,5]thiadiazolo[3,4-*g*]quinoxaline (BEDOT-TQ-Hx<sub>2</sub>) whose structures are shown in Chapter 4

were synthesized according to the previously reported literature. Poly (9, 9-dioctylfluorene) (Sticky-PF) was synthesized specifically for this study.<sup>122</sup>

Gold coated Kapton® (100 nm gold layer on 1 mm Kapton® sheets) used as an electrode substrate was purchased from Astral Technologies (product no: ATU1310) and cut into the desired size. Adhesive conducting copper tape was used to make electrical contacts to the gold electrodes and was purchased from 3M Electronics Department (3M™ EMI Copper Foil Shielding Tape 1194). Platinum wires and sheets and silver wires were purchased from Alfa Aesar. Gold and platinum button electrodes were purchased from Bioanalytical Systems, Inc. (BAS). Single walled nanotubes films (SWNT) were prepared according to methodologies previously reported<sup>41</sup> and details will be explained in Chapter 3.

### **Inert Atmosphere Handling**

Since n-doping of donor-acceptor-donor systems is extremely sensitive to water and O<sub>2</sub> in ambient conditions, all of the Type IV devices were handled in a dry box (VAC Omni Lab) providing a working area hermetically sealed from the ambient environment, consisting of an inert atmosphere of Argon, nearly free of moisture (~1ppm) and oxygen (~0.15ppm). An antechamber mounted on the side of the dry box is used for passing materials in and out without disturbing the inert atmosphere of the box. Any time the antechamber is exposed to ambient atmosphere for the insertion of items into the dry box, three cycles of evacuation and filling of the antechamber with inert gas before any of the objects can be safely brought inside the dry box, without contaminating the inert atmosphere.

The solvents used in the glovebox were deoxygenated by freeze-pump-thaw for three cycles before being transferred into the glovebox. This process is as follows: The distilled solvents in a sealed Schlenk flasks were placed in liquid nitrogen filled dewar. Once the solvent solidified, the flasks were exposed to vacuum for 30 minutes. Then the flasks were sealed again

and solvents were allowed to melt by removing away from liquid nitrogen dewar. After transferring into the glovebox, activated molecular sieves were again added to the solvents to remove any residual water.

### **Electrochemical Methods**

All the electrochemical measurements were performed using an EG&G PAR model 273A potentiostat which utilizes a three electrode configuration, controlled using CorrWare software (Scribner Associates). A typical one compartment three electrode cell setup is comprised of a working electrode, an auxiliary (counter) electrode, and a reference electrode in a glass container. A number of different materials used as working electrodes in this work include 0.02 cm<sup>2</sup> diameter gold and platinum electrodes encapsulated in a Teflon casing (BAS), gold coated Kapton® sheets, gold/chromium coated glass slides, SWNTs film on glass and SWNTs film on polyethylene terephthalate (PET). Electrical contact to gold coated Kapton®, gold/chromium coated glass slides electrodes were made with copper tape and to SWNTs on glass or SWNTs on PET were made with palladium layer in contact with nanotubes. A piece of Pt foil welded together with a Pt wire was used as the counter electrode, providing the required current to sustain the developing processes at the working electrode. The size of the foil Pt counter electrode is always chosen as larger than the area of the working electrode to be used. This arrangement prevents large currents from passing through the reference electrode and changes its potential. Several different types of reference electrodes were used in this work. In aqueous solvents, a silver-silver chloride (Ag/AgCl) saturated in KCl electrode, commercially available from BAS, was used. For non-aqueous reaction mediums, a silver wire in contact with 0.1M AgNO<sub>3</sub> dissolved in a particular solvent (e.g., ACN) is used and denoted as Ag/Ag<sup>+</sup> reference. A silver wire (Ag) pseudo-reference is used by directly immersing into the reaction medium. Since the potential of silver wire pseudo-reference electrodes rigorously depends on the instant

conditions, it was frequently calibrated versus a standard ferrocene solution, which consist of 10 mM ferrocene in an electrolyte solution of interest, and the potentials are reported due to the  $E_{1/2}$  of the ferrocene/ferrocinium ( $\text{Fc}/\text{Fc}^+$ ) against the silver wire.

All solutions used for electrochemical techniques discussed within this dissertation were carefully prepared from dry solvents as well as pure electrolytes and monomers. Electrolyte and monomer purity is a significant contributor to maximize reproducibility in electrochemistry. Therefore, fresh solutions were used unless otherwise noted, due to the highly reactive nature of electron-rich heterocyclic monomers. Furthermore, the solutions were carefully bubbled with Ar to remove incipient oxygen prior to any experiment. The argon line is positioned just above the surface of the solution to maintain an inert atmosphere blanket during the experiments. This procedure helped to eliminate or at least minimized any experimental variable.

### **Cyclic Voltammetry**

Cyclic voltammetry (CV) is one of the most extensively used electrochemical techniques to study electroactive and conjugated polymers as well as metal oxides due to its simplicity and versatility. It provides both quantitative and qualitative information about the system under study. In this technique, the current density at the working electrode/solution interface is monitored as a function of the potential, while the potential is being swept over a specified voltage range at a constant rate. This dynamic parameter, rate of the potential cycling can be variable accordingly for different reactions and is expressed in mV/s units. The obtained voltammograms reveal information regarding the electrochemical potentials at which the oxidation and reduction processes occur, how fast these processes occur, the potential range over which the electrochemical system is stable and the degree of reversibility of the electrode reactions under study. The scan rate, switching potentials, as well as the magnitudes of the anodic peak current ( $i_{pa}$ ), cathodic peak current ( $i_{pc}$ ), anodic peak potential ( $E_{pa}$ ) and cathodic

peak potential ( $E_{pc}$ ) are the most important parameters of cyclic voltammetry. Furthermore, CV reveals information regarding the stability of the product during multiple redox cycles.

In this dissertation, CV is used for three different purposes; first, to prepare the electroactive films via potentiodynamic electrodeposition; second, to study electroactive films of polymers and metal oxides; and finally, to characterize the supercapacitor devices which are fabricated by combining the two electrode films together by a conducting electrolytic media.

Cyclic voltammetry measures current with regard to applied voltage at a constant sweep rate, ( $v=dV/dt$ ), and is therefore a means of evaluating capacitance. As explained in Chapter I of this dissertation, the capacitance of a capacitor is defined by the relation  $C = dQ/dV$ , where  $V$  the voltage difference between the plates associated with accommodation of charge  $Q$  on the each plate. Since the charge actually is the integration of current over time range and can be calculated with the following equation;

$$Q = \int I dt \quad (2-1)$$

where the current  $I$  is expressed in amperes (A), the charge  $Q$  is in coulombs (C or As) and time  $t$  is in seconds.

The capacitance can then be calculated through incorporating Equation (2-1) into the capacitance equation as follows;

$$C = dQ/dV = \int I dt / dV = I \Delta t / \Delta V = I / v \quad (2-2)$$

where  $I$  is the average current density ( $A/cm^2$ ) and  $v$  is the scan rate in V/s.<sup>123</sup>

Throughout this dissertation the voltammograms are often graphed as capacitance vs. voltage as well as current vs. voltage. Ideally, a perfect capacitor response would be a rectangular shaped voltammogram. However, the resistance is unavoidable in real systems so most experimental data take the shape of a parallelogram with irregular peaks. The plots obtained at

different scan rates are often displayed on the same graph to demonstrate the rate of charging and discharging characteristics which corresponds to different power levels. Faster sweep rates indicate higher power levels. As expected, capacitance decreases with higher discharging frequencies. Voltammograms that depicts mirror-images represents reversible charging and discharging profile while an irreversible process will have two separate charge and discharge profiles.

### **Constant Potential Method: Chronocoulometry / Chronoamperometry**

In the controlled potential experiment, the potential is set at a constant value sufficient to cause the rapid oxidation or reduction of the species and is maintained at this value until only the oxidized or reduced species is present. During potential step methods, the potential of the working electrode is switched instantaneously between two potentials, either as a single step or repeated steps. Both chronoamperometry and chronocoulometry have the same potential wave form. In chronocoulometry, the charge is monitored as a function of time, whereas in chronoamperometry, the current is monitored as a function of time. The data obtained during the chronoamperometry experiment is based on the Cottrell equation, which defines the current-time dependence for linear diffusion control:

$$i = nFACD^{1/2} \pi^{-1/2} t^{-1/2} \quad (2-3)$$

where,  $n$  is the number of electrons transferred per molecule,  $F$  is Faraday's constant (96,485 C/mol),  $A$  is the surface area of the working electrode ( $\text{cm}^2$ ),  $D$  is the diffusion coefficient of the redox active sites ( $\text{cm}^2/\text{s}$ ),  $C$  is the bulk concentration ( $\text{mol}/\text{cm}^3$ ), and  $t$  is the time in seconds.

The analysis of chronocoulometry data is based on the charge calculated by integrating the Cottrell equation, which defines the charge-time dependence for linear diffusion control:

$$Q = 2nFACD^{1/2} \pi^{-1/2} t^{1/2} \quad (2-4)$$

Chronocoulometry has an advantage over chronoamperometry that the integration of current smoothes random noise and eliminates time independent current. In this dissertation, constant and step potential methods are used for to prepare homogeneous electroactive films and to examine these electroactive films of polymers and metal oxides as well as supercapacitor devices in terms of switching charges prior to device construction for balanced switching, stability of the films and devices, etc.

### **Constant Current Method: Chronopotentiometry**

In chronopotentiometry, a current step is applied across an electrochemical cell, between the counter and working electrodes, and the potential of the working electrode is monitored with respect to the reference electrode. The data obtained is based on the rate of change in potential versus time. In order to support the applied current, a redox reaction occurs at the surface of the working electrode. In this technique, the ohmic drop results from solution resistance are constant and equal to the product of the current and the solution resistance. The ohmic distortion can be simply corrected by a constant potential offset in contrast to potentiostatic experiments.

To analyze the supercapacitor devices as well as active films, cyclic chronopotentiometry, in which instantaneous current reversal is enforced on the working electrode, is used. The films or devices were charged and discharged repeatedly; and the potential change is monitored versus time. From the slope of the linear part of the discharging curves, the voltage change over the time interval; " $\Delta V/\Delta t$ " can be calculated. Since the current is constant, by incorporating the slope of the discharging curve into Eq 2-2, the discharge capacitance  $C_d$  can be evaluated.

### **Electropolymerization**

Electrochemical deposition of the polymer films was carried out in solutions composed of 10 mM monomer in 0.1 M electrolyte solution of interest unless otherwise noted. The electrodeposition is performed via potentiodynamic or potentiostatic methods.

The potentiodynamic polymerization of a monomer is typically performed by cyclic voltammetry. The anodic scanning usually starts at low potentials where no redox reactions occur. Once the electrode potential reaches to a sufficient value, the monomer is oxidized to its radical cation, which is determined by an anodic peak appearance. Monomer oxidation is immediately followed by coupling of radicals to form oligomers which precipitate onto the electrode surface as polymers. The electroactivity of the polymers that was deposited onto the working electrode can be instantly monitored by the appearance of a reduction peak of the oxidized polymer while scanning in the cathodic direction. Since the current is directly proportional with the electrode area, as shown in the Randles-Sevcik equation<sup>124</sup> (Equation 2-1), the increase in the peak currents is attributed to an increase of the working electrode area.

$$i_p = (2.69 \times 10^5) n^{3/2} A D^{1/2} C_b \nu^{1/2} \quad \text{at } 25^\circ\text{C} \quad (2-5)$$

where  $n$  is the number of electrons,  $A$  is the surface area of the working electrode ( $\text{cm}^2$ ),  $D$  is the diffusion coefficient ( $\text{cm}^2/\text{s}$ ),  $C_b$  is the bulk concentration of the electroactive species ( $\text{mol}/\text{cm}^3$ ), and  $\nu$  is the scan rate ( $\text{V}/\text{s}$ ).

Continuous cycling yields more polymer deposition on the electrode, revealed by the increasing anodic and cathodic peak current densities of the polymer oxidation/reduction. Besides the polymer's reduction, usually the return scan right after the monomer oxidation crosses the anodic wave and is called as the nucleation loop which is exclusive to conjugated polymers. This feature also arises due to the increased conducting surface area of the working electrode by polymer (or metal) deposition. Furthermore, the Randles-Sevcik equation dictates that the peak current is proportional to the square root of the scan rate for diffusion-controlled solution-based electrochemical systems.

The potential for potentiostatic electropolymerization of a monomer either via single or repeated steps, is typically determined from cyclic voltammograms of the monomer. When the peak current for monomer oxidation is determined, the corresponding potential is applied to the working electrode during subsequent potentiostatic electropolymerization experiments. Potentiostatic deposition is a very effective method to deposit smooth and homogeneous conjugated polymer film. The polymerization can be terminated once certain amount of charge has passed (determined by chronocoulometry), so the desired mass of the polymer has reached. By using a calibration plot of charge versus polymer mass, determined by performing separate experiments for different monomers, the resulting polymer mass can be chosen by setting the potential to be applied until the necessary charge has passed. Once the polymer films are prepared they were rinsed thoroughly with fresh solvent or monomer-free electrolyte solution to wash away unreacted monomers trapped on the film prior to electrochemically switching in a monomer-free electrolyte.

### **Electrochemistry of Electroactive Film**

Electrochemistry of active films was performed again in a one compartment three-electrode cell as described above. Only this time the polymer-coated (or metal oxide coated) electrode were used as the working electrode. The working potential range of a polymer includes a region from the neutral form of the polymer to a value sufficient to oxidize or reduce the polymer. Electroactive films were reversibly cycled in this range between their neutral and doped forms in a monomer free 0.1 M electrolyte solution using cyclic voltammetry.

As the electroactive polymer films are stepped between their fully neutral and fully doped states, an increase or a decrease in the current response is observed, which is attributed to polymer oxidation or reduction and incorporation or expulsion of the charge compensating counter-ions throughout the polymer film, respectively. Prior to electrochemical study, all the

films were switched between their oxidized and reduced states 3 to 8 times to condition the polymer by stabilizing ion and solvent diffusion in and out of the polymer film. This is called “break-in” period required to obtain more reproducible experimental observations. Important parameters of a polymer CV are; the half-wave potentials  $E_{1/2}$ , (the potential where the concentrations of the oxidized and reduced species are equal), determined by taking the average of the peak anodic and cathodic current potentials; scan rate dependence of the peak current; and the reversibility (shape) of the potential wave.

In those cases for electrode adsorbed species such as electroactive polymers adhered to the working electrode, the Randles-Sevick equation (Eq 2-5) does not apply, because the redox processes of electrode-bound conjugated polymers are not diffusion controlled. Therefore a different approach must be taken. The following Eq 2-6, for surface-confined species dictates that both the anodic and cathodic current responses will scale linearly with scan rate.

$$i_p = n^2 F^2 A \Gamma \nu / 4RT \quad (2-6)$$

where  $n$  is the number of electrons,  $F$  is Faraday’s constant (96,485 C/mol),  $A$  is the surface area of the working electrode ( $\text{cm}^2$ ),  $\Gamma$  is the concentration of surface bound electroactive centers ( $\text{mol}/\text{cm}^2$ ) and  $\nu$  is the scan rate (V/s). In scan rate dependence experiments, a linear relationship between the current responses and scan rate indicates a non-diffusion controlled process where the electroactive polymer is well adhered to the working electrode surface. Although conjugated polymers can switch rapidly without loss of current response, the rate of switching is still dependent upon film thickness, electrolyte, and the morphology of the polymer.

### **Supercapacitor Device Fabrication**

The construction of a supercapacitor device consists of combining together positive and negative electrodes containing active films with a conducting electrolytic media. The polymeric

gel electrolyte used as the conductive media in Chapter 3 and regular liquid base electrolyte solutions were used in the studies presented in Chapter 4 and Chapter 5.

The uniform electroactive films used as electrodes of the device were obtained by electrodeposition of the polymers or metal oxides onto the substrates, where the details are specified in each chapter. The amount of complementary polymers or metal oxides on each electrode can influence the device operation to a large extent. Therefore, it is important to match redox switching charges of the complementary polymers for balanced switching in a supercapacitor device fabrication. As it was mentioned earlier in the previous section, the deposition amounts can be controlled by monitoring the total charge density passed during electrosynthesis. However, it is not so accurate to get the same amount of active material deposition in each deposition due to the unavoidable experimental errors. For that reason, it is essential to check the charge density of the electroactive films while switching between their doped (p- or n-) and neutral states prior to device assembly. By using CV or simply by applying an oxidizing or reducing potentials, respectively, conjugated polymers can be switched between their doped and neutral states and the total charge passed during the experiments can be calculated as explained in the previous sections; (Equation 2-1). This total charge,  $Q$  is related to the number of electrons transferred per molecule,  $n$  and the number of moles of the oxidized species initially present,  $N$  through Faraday's law:

$$Q = nFN \quad (2-7)$$

where  $F$  is Faraday's constant (96,485 C/mol),  $n$  = number of electrons transferred/molecule, and  $N$  = amount of material (mol). When dealing with conjugated polymers, the doping level of the films should be included in this equation as well.

After the electropolymerization, the films were set to the desired doping state of fully oxidized, fully reduced or neutral by applying a consequent potential for 15s to ensure charge balance level prior to device assembly. In Type I and hybrid devices as described in Chapter 3 and Chapter 5 respectively, anode films were oxidatively doped (fully oxidized) while cathode films were fully neutralized in a monomer-free solution in order to establish the initial charge balance state of the device. In Type IV devices described in Chapter 4, both anode and cathode films were fully neutralized prior to device construction and a special Teflon cell was used that allows insertion of two Au-Button electrodes separated by 0.5cm with the electrolyte solution in between them. In Chapter 5, the positive and negative electrode films were placed 1.5 cm away from each other in a glass container with the electrolyte solution.

In Chapter 3, multiple layers including two electroactive films deposited on a conducting substrate either onto Gold/ Kapton or onto SWNTs were sandwiched together to form the supercapacitor device. The films were coated via syringe with a viscous gel electrolyte until the entire polymer surface was uniformly covered to ensure adequate swelling of the polymer. These substrates were then carefully applied to face to face and allowed to stabilize for 24 hours. To prevent electrodes from shorting out that might occur while applying two electrodes to one another, a porous separator paper (Gore™ Excellerator®) were used between the electrodes. In case of flexible Gold/Kapton and SWNT films which are not on glass slides, acetate (3M transparency film, PP2500) were used as a support and cover for the substrates. Besides acting as an ion transport material, the gel electrolyte provides a relative encapsulation at the edges of the device as the PMMA becomes insoluble. This minimizes further solvent evaporation, prevents leaking, and allows for long-term testing at ambient conditions. Although the devices are self-encapsulated by a seal formed around the edges by the gel electrolyte, the entire device still

carefully sealed on all four edges using transparent tape to prevent a possible leakage. The device schematic and photographs can be seen in the subsequent chapters.

The polymeric gel electrolyte used as the conductive media was based of a salt plasticized in solvent that has a high boiling point. The optimized composition of the gel electrolytes includes 10% salt, 20% ultrahigh molecular weight PMMA and 70% solvent by weight ratio in order to get both substantially conducting and mechanically stable and viscous gel. The gel was prepared by dissolving Li[N(CF<sub>3</sub>SO<sub>3</sub>)<sub>2</sub>] in tetraethylene glycol dimethyl ether or PC, followed by very slowly adding PMMA while vigorous stirring and mild heating (60°C) for a period of about two hours or until all components were incorporated to form a highly viscous, a honey like - consistency.

The performance of the capacitors was characterized using linear sweep voltammetry and galvanostatic charge/discharge techniques as described in the previous sections.

### **Energy and Power Characteristics of a Device**

Supercapacitors are energy storage and conversion devices. Besides the charge storage ability, the energy and power densities are among the most important metrics for supercapacitors. The performances of these devices are characterized using their energy storage and conversion features as demonstrated in Ragone plots shown in Fig 1.1 (Chapter I). The energy density of a supercapacitor charged to a potential difference of V, for an accumulated charge Q (Coulombs) residing on electrodes of the capacitor, can be calculated due to Eq 1-2:

$$E = \frac{1}{2} CV^2 = \frac{1}{2} QV$$

where C is the capacitance in Farads (F). Although the voltage is defined as the potential difference between the cathode and the anode; the voltage of a supercapacitor progressively decays during the discharging process since work is being continuously done against the charges being accumulated/released on the electrode. Thus an average voltage of

$$V = (V_{charged} + V_{discharged})/2 \quad (2-8)$$

is realized in calculation of the energy density of a supercapacitor device. This equation assumes a ideal linear voltage decay at constant current. The energy density is usually expressed in (Wh/kg) as the specific (or the gravimetric) energy density and can also be stated as the areal (Wh/m<sup>2</sup>) and the volumetric (Wh/L) energy density depending on how the capacitance is expressed.

Power is the average amount of energy delivered per unit time, in essence, it is the discharge rate of the supercapacitor device. The power density values are evaluated by dividing the energy density values by the discharge time of the cell. Correspondingly, the average power delivered by a supercapacitor is defined as:

$$Power = iV \quad (2-9)$$

where  $i$  is the average current and  $V$  is the average voltage described above. In a chronopotentiometry, discharge performed at constant current, thus determining the average power requires only monitoring of voltage during discharge. In a CV experiment, the average current density during the discharge of the cell should be determined. The power density is typically expressed in W/kg as the specific (or the gravimetric) power density and can also be stated as the areal (Wh/m<sup>2</sup>) and the volumetric (W/L) energy density depending on how the capacitance is expressed.

### **Surface Characterization Techniques**

In this dissertation, both atomic force microscopy (AFM) and scanning electron microscopy (SEM) used to characterize surface and cross section morphologies of films. Both techniques are the foremost tools for imaging and offers high-resolution at the nanometer scale.

## **Scanning Electron Microscopy**

In SEM, images are formed by scanning the sample surface with a high-energy beam of electrons in a raster scan pattern. The electrons interact with atoms at or near the surface of the sample resulting in low energy secondary electrons being emitted from the sample surface. These emitted electrons are detected by a photomultiplier tube to form the topographic image. The other types of imaging with the SEM includes backscatter imaging that can provide compositional information, characteristic x-ray imaging providing information on the elements present in the sample and specimen current imaging that can be used to show sub-surface defects. Depending on the instrument, the SEM can produce very high-resolution images with the resolution between less than 1 nm and 20 nm and also with a three-dimensional appearance useful for understanding the surface structure of a sample.

For all SEM studies, an Hitachi S-4000 FE-SEM was utilized for obtaining topographic images throughout this dissertation. The carbon double side conductive tabs (PELCO Tabs™) were used to place the films onto the sample holder and the conducting carbon paint (EM Graphite Conductive Adhesive 154) is applied to the edges of the films to enhance the adhesion. Prior to imaging, the samples were sputter coated a thin layer (about 100Å thickness) of gold and palladium alloy in a Denton Vacuum sputter coater in order to prevent surface charging, minimize radiation damage and to increase the electron emission from the films. A 45° tilted angle sample holder is used unless otherwise is indicated, in order to improve the quality of the images obtained. An acceleration voltage of 6 kV was selected for examining the samples.

## **Atomic Force Microscopy**

This contact technique has an operation principle involving a stylus or cantilever that moves across a sample surface. The sample surface is scanned with a sharp tip, with nominal tip radius on the order of 10 nm, located at the end of the cantilever. AFM tips and cantilevers are

typically microfabricated from Si or Si<sub>3</sub>N<sub>4</sub>. This flexible cantilever with a very low spring constant induces forces smaller than the interatomic forces between the tip and the sample, thus the topography of the sample can be monitored without displacing the atoms. AFM uses an optical lever detection system involving a focused beam from a laser diode onto the back of the cantilever, to sense the deflection of the cantilever as a response of surface height variation. The beam reflects off the back of the cantilever onto a segmented position sensitive photodiode. The amplified differential signal between the upper and lower photodiodes provides a sensitive measure of the cantilever deflection. Finally, this response signal is converted to a digital signal. AFM has the advantage of imaging almost any type of surface, including polymers, ceramics, composites, glass, and biological samples, whether it is conducting, semiconducting or insulating surface. Three imaging modes; contact mode, non-contact mode and tapping mode can be used to produce topographic images of sample surfaces.

**Contact Mode AFM:** The contact mode AFM operates by dragging the tip over the surface corrugation, while monitoring the change in cantilever deflection with a split photodiode detector. The tip is in contact with the surface through the adhesive forces between the tip and the surface, and therefore it is adjusted to maintain a constant height above the surface, so a constant deflection. The dragging motion of the probe tip can cause substantial damage to both sample and the probe and create artifacts in the image data.

**Non-Contact Mode AFM:** This mode uses an oscillating stiff cantilever located quite close to the sample surface in the attractive regime, but not touching it. Attractive Van der Waals forces between the tip and the sample lowers the cantilever's resonant frequency, and topographic images are monitored based on measuring changes to the resonant frequency or

amplitude of the cantilever. Since the forces between the tip and sample are substantially low, on the order of pN ( $10^{-12}$  N), this mode has a very low resolution.

**Dynamic Force/“Tapping Mode” AFM:** A very stiff cantilever is oscillated closer to the sample than in noncontact mode and close to its resonance frequency (normally on the order of 100 kHz) so that the tip intermittently touches to the sample only for a short duration in each oscillation cycle. The amplitude at the operating frequency is maintained at a constant level, called the set-point amplitude, by adjusting the relative position of the tip with respect to the sample during scanning. As the tip touches the sample, the interactions between the tip and the surface molecules alter the amplitude, resonance frequency and the phase angle of the oscillating cantilever. The changes in the amplitude and phase angle of the cantilever probe are monitored as the topographic (height) and the phase image, respectively. The phase image often provides significantly more contrast than the topographic image and has been shown to be sensitive to the material surface properties such as stiffness, viscoelasticity and chemical composition. This method of operation results in high resolution images especially on soft samples, while virtually eliminating the lateral forces such as drag, so less surface damage is inflicted.

All the AFM experiments were carried out using the Digital Instruments MultiMode<sup>TM</sup> Nanoscope III in this dissertation. Tapping mode AFM utilized in all of the AFM images unless otherwise is indicated.

CHAPTER 3  
PPRODOP BASED TYPE I SUPERCAPACITORS

**PProDOP as a Charge Storage Electrode Material**

The use of conjugated polymers (CPs) as pseudocapacitor electrode materials has been widely investigated.<sup>125, 126</sup> As explained in Chapter I, their energy storage is attributed to redox p- and n-doping Faradaic reactions. The redox process of conjugated polymers is fast, and occurs efficiently since films are highly porous and accessible, allowing fast percolation of electrolyte through the matrix. Thus, fast discharging gives rise to the high power densities that are possible with these materials. CPs have the ability to store charge throughout their entire volume; therefore, elevated levels of high charge densities can be achieved. One of the most attractive aspects of CPs is the ability to tailor specific properties such as conductivity, morphology, etc. with straight forward synthetic modifications without drastic adjustments to the polymer backbone. In addition to fast redox electrochemistry with suitable morphology, CPs' lightweight nature, synthetic flexibility and ease of preparation in the form of extended surface films make them attractive for supercapacitor applications. Moreover, CPs can be easily and inexpensively made in large amounts. Since the entire volume of polymer is involved in the charge storage process, supercapacitors that use CPs have high capacitive energy densities. Furthermore, their fast doping-dedoping processes allow for devices with low equivalent series resistance (ESR) and high specific powers. In terms of satisfactory energy and power densities, cycle life, low weight and thermal stabilities with the predicted low material cost relative to other materials, conducting polymers represent an attractive alternative to materials currently used in electrochemical capacitors.

Characteristically, conducting polymers offer specific capacitances in the range of about 100-250 F/g. Over the years, the bulk of conducting polymer based supercapacitor research has

focused on polyaniline, polypyrrole, polythiophene and their derivatives with different kind of electrolyte and substrate systems to achieve high energy storages with high capacitances.<sup>4, 15, 127</sup>

Most of this work has been directed toward use in Type I supercapacitors.

Being one of the most commercially successful polymers used for supercapacitor applications to date, poly(3,4-ethylenedioxythiophene) (PEDOT), exhibits higher chemical and electrochemical stability than most of the other CPs.<sup>69, 72, 128</sup> Introduction of the ethylenedioxy bridge with electron-donating oxygen atoms onto the 3- and 4-positions of the thiophene ring increases the electron density on the  $\pi$ -system, which raises the highest occupied molecular orbital (HOMO).<sup>129, 130</sup> As a result, PEDOT can be easily oxidized, the polymer has a lower bandgap (1.6 eV) than unsubstituted PTh, possesses lower oxidation potentials, and higher stability upon oxidation. A family of poly(3,4-alkylenedioxythiophene) derivatives (PXDOTs) with varying size and composition of the alkylene bridges has been synthesized by the Reynolds' group, and shown to have a variety of the electronic and optical properties.<sup>131-135</sup> Moreover, through the same approach by introducing alkylenedioxy bridge as in the PXDOTs, a series of poly-(3,4-alkylenedioxypyrrole)s (PXDOPs) have been synthesized in the Reynolds' group to obtain polymers with very low oxidation potentials.<sup>119, 120, 136</sup> Analogous to PXDOTs, introduction of the alkylenedioxy moiety in the 3- and 4- positions of the pyrrole ring increases the electron-rich character of the monomer, and raises the HOMO level of the molecule.<sup>137-139</sup> Consequently, this new family of monomers and polymers have a relatively lower bandgap (~2.2 eV), exhibit outstanding stabilities as analogues to PXDOTs, display very low oxidation potentials that allows milder polymerization conditions yielding polymers with much fewer structural defects.<sup>140</sup> Moreover, some of them possess aqueous compatibility similar to the intrinsic property of polypyrroles.<sup>141</sup>

## Electropolymerization of ProDOP

Among the PXDOP derivatives, poly(3,4-propylenedioxy pyrrole) (PProDOP), whose structure is illustrated in Fig 3-1, has started to attract attention in the academic world recently, due to its multitude of interesting and unique materials properties. PProDOP is highly electron rich in character, easily p-type doped, and exhibits highly capacitive behavior in its redox electrochemistry. Besides its high doping capacity, it provides a long-term chemical stability, high electrical conductivity, along with fast and efficient switching between redox states. This chapter will focus on the behavior of PProDOP in greater detail, specifically in the realm of supercapacitors.

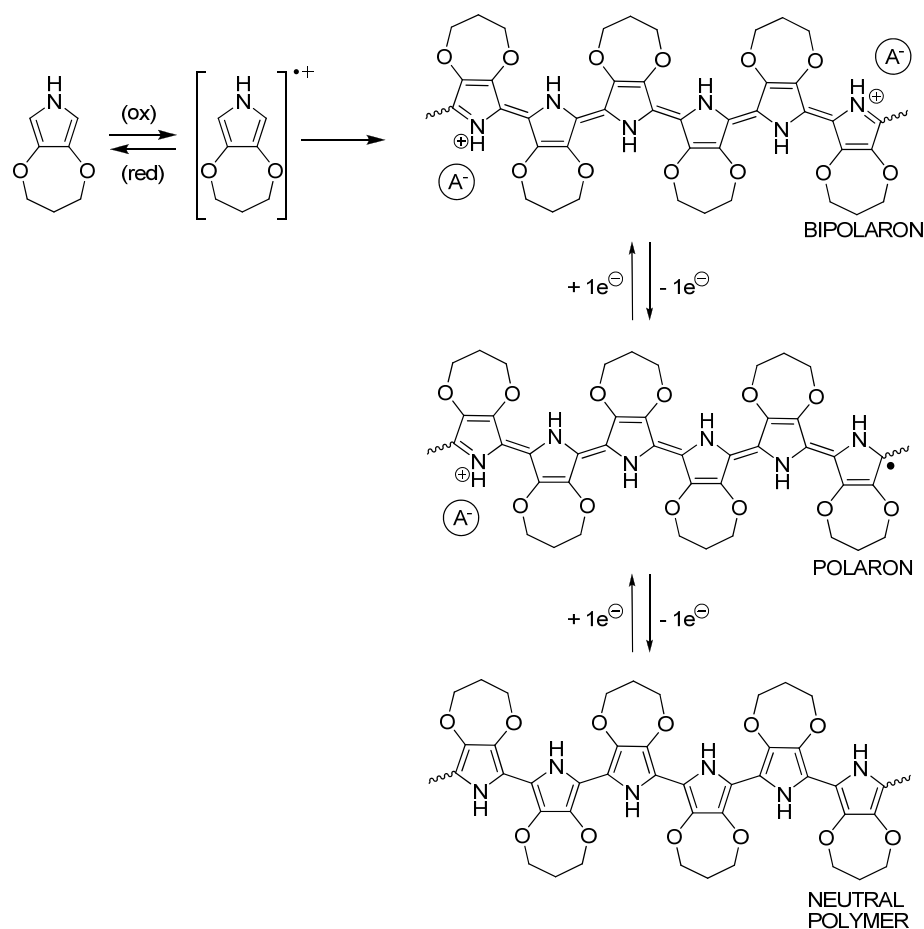


Figure 3-1. Structure of poly(3,4-propylenedioxy pyrrole) (PProDOP) shown along with the electropolymerization mechanism and the doping/dedoping processes of PProDOP, where  $\text{A}^-$  represent dopant ion.

Electrochemical formation of PProDOP proceeds via a step-wise chain growth mechanism by oxidation of the neutral monomer, shown in Fig 3-1, that yields the radical cation formation at the anode surface. Then coupling of two radical cations (dimerization reaction) proceed. Further, this dihydro dication dimer species loses two electrons and rearomatizes to form the neutral dimer. Consequently the dimer oxidizes again to form the radical cation. Through coupling of two radical cations or a radical cation with a neutral monomer, the polymerization proceeds and the chain length increases. As the oligomers become insoluble in the electrolyte solution, they start precipitating on the anode. The polymerization proceeds through coupling at the 2, 5 positions of the ProDOP monomer resulting in a linear backbone polymer with an enhanced degree of order. As was mentioned above, the substitution of the PPy monomer with electron donating propylenedioxy group increases the electron-rich character of the monomer and decreases the monomer oxidation potential. This results in one of the most important features of PProDOP that the electropolymerization occurs under milder conditions, reducing the possibility of obtaining overoxidized material with structural defects.

Cyclic voltammetry offers a powerful method for the characterization of the monomer and polymer redox processes. Oxidative electrochemical polymerization of ProDOP was carried out using multiple scan cycling in propylene carbonate (PC) with 0.1 M electrolyte solution on gold substrates as illustrated in Fig 3.2. Tetrabutylammonium perchlorate (TBAP) and lithium bis(trifluoromethanesulfonyl) imide (LiBTI) were used as electrolytes, as shown in Fig 3.2A and Fig 3-2B, respectively. Electroactive films were easily prepared from a 10mM solution of monomer in each electrolyte system by potentiodynamic sweeping from a potential of negative to that of the polymer reduction, to a potential approximately 50–100mV past the peak monomer oxidation potential. The peak oxidation potentials ( $E_{p,m}$ ) obtained during the first scan were

found to be +0.65 vs.  $\text{Fc}/\text{Fc}^+$  and were all in agreement with each other for different electrolyte systems. The lower oxidation potential compared to pyrrole (+0.9 vs.  $\text{Fc}/\text{Fc}^+$ ) can be attributed to ease of formation of the radical cation at the electrode due to the electron rich character of ProDOP monomer. The changing shape of the current-voltage relationship with the progression of the cycles in Fig 3-2A and B is most probably due to the deposition of polymer on the electrode with an increased resistance.

ProDOP exhibits the fastest nucleation and the most efficient deposition rate among several other XDOPs.<sup>119</sup> ProDOP electropolymerized quite efficiently in each electrolyte medium; only few potential sweeps were enough for the formation of an adhering, adsorbed electroactive film onto the electrode surface. This efficient film deposition is attributed to fast coupling of the reactive intermediate radical cations with instant polymerization on the electrode surface. No color is evident in the electrolyte solution and, thus; soluble oligomer formation does not occur. The coupling of radicals to form oligomers results in precipitation of them on the electrode surface. The electroactivity of polymer on the gold electrode can be easily seen from the voltammograms evidenced by the redox peak appearance by the as made polymer film. The redox peak potentials of oxidative doping of CPs to their conducting forms are functions of the dopant ion, solvent and supporting electrolyte used.<sup>130</sup> There were not any sharp faradaic peaks from polymer redox processes observed for PProDOP films. This result is probably due to the polymers' capacitive behavior, especially in the presence of LiBTI electrolyte. PProDOP exhibits a half-wave potential ( $E_{1/2,p}$ ) approximately of -0.3V vs  $\text{Fc}/\text{Fc}^+$  and is among the polymers with the lowest oxidation potentials for p-type doping. As an example, PEDOT has an half-wave potential of around -0.2V vs  $\text{Fc}/\text{Fc}^+$  in regular electrolyte solutions, which shows its more resistive character to oxidaditive doping compared to ProDOP.

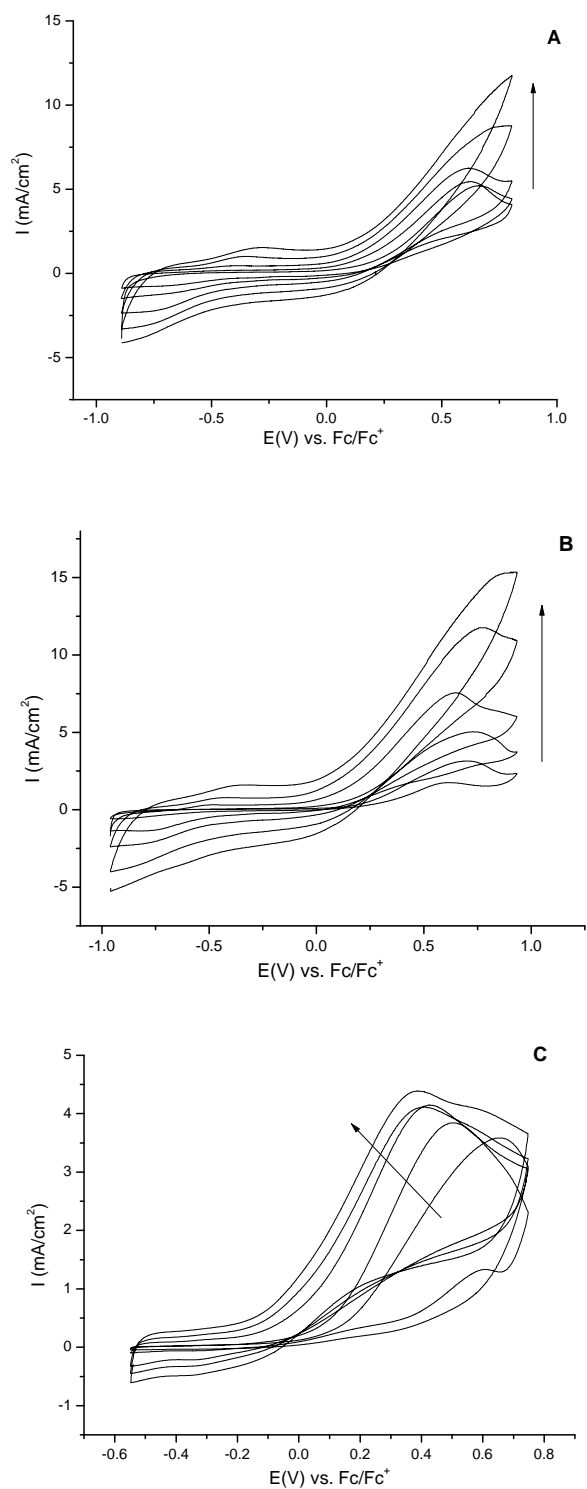


Figure 3-2. Electrochemical polymerization (first 5 cycles) of ProDOP by potential scanning A) in TBAP/PC on Au Button, B) in LiBTI/PC on Au Button and C) in LiBTI/PC on Au/Kapton at 50mV/s.

In Fig 3-2C, cyclic voltammogram of ProDOP in a same electrolyte solution (LiBTI/PC) as in Fig 3-2B, however on a larger area gold substrate ( $1\text{cm}^2$ ) is shown. The broader monomer oxidation peak, compared to the same system on gold button electrode which is  $0.02\text{cm}^2$ , is typically observed for larger area electrodes with conducting polymer systems. Moreover, the appearance of a shift in the monomer oxidation potential was observed with the progression of each cycle, and may indicate a growth involving the coupling of soluble oligomers, which are probably more reactive than the monomer itself, so have a reduced oxidation potential.<sup>142, 143</sup> Therefore, the combination of the oxidation of monomer species with the oxidation of oligomer species results in a broader and shifted peak.

### **Electrochemistry of PProDOP Films**

As was introduced in Chapter I, conducting polymers store and release charge through their redox doping and dedoping processes. Fig 3-1 illustrates the mechanism of this Faradaic charge storage in PProDOP. It can be seen that the neutral polymer in its uncharged state becomes positively charged (p-type doping) upon the removal of an electron from the polymer to form a delocalized radical cation (a polaron). The polaron can undergo a second oxidation to form the dication (a bipolaron). Consequently, the dopant anions, shown as  $A^-$  in the figure, from the electrolyte enter into the polymer to compensate the charge created on the backbone. When neutralization occurs the anions are released back into the electrolyte solution. Introduction of charge carriers in the form of polarons and bipolarons into the polymer matrix occurs at the polymer/electrode interface and these charged states are quickly dispersed through the polymer matrix due to migration and diffusion via a hopping mechanism. PProDOP can be doped and dedoped rapidly to high charge densities.

Electropolymerization is a suitable synthetic method to prepare electrodes for supercapacitor applications, since it gives rise to polymers that are more open and porous

structure compared to the packed morphologies that result from spin coating deposition.<sup>144</sup> While cyclic voltammetry offers a powerful method for the characterization of the monomer and polymer redox processes, deposition of the polymer has been carried out by potentiostatic electrochemical polymerization in order to get higher current efficiencies, more homogeneous (uniform) and smooth films of PProDOP.<sup>119</sup> Polymer films were deposited at an applied potential equal to the monomer peak potential of +0.65V vs. Fc/Fc<sup>+</sup> plus 0.05V on Gold/Kapton electrodes (1cm<sup>2</sup>) in PC using 0.01M monomer and 0.1M TBAP and LiBTI as electrolytes. PProDOP is stable to higher potentials, since the presence of 3,4-alkylenedioxy bridge substituent at 3 and 4 position of the pyrrole ring prevents overoxidation of the polymer thus the degradation of the conjugated backbone.

The prepared films were washed in monomer free electrolyte media and characterized by cyclic voltammetry. Cyclic voltammograms of PProDOP films with the scan rate dependence for the redox switching are shown in Fig 3-3a&c. Cyclic voltammograms were carried out at different scan rates from 50 to 500 mV/s between -0.4 and +0.4 V vs Fc/Fc+. Well-defined voltammograms with reversible broad peaks, which are typical of large surface area (1cm<sup>2</sup>) electrodes, were observed for both electrolyte systems. The peak currents in the cyclic voltammograms in the presence of LiBTI electrolyte increase linearly up to 500 mV/s scan rate, indicating that the electroactive sites are surface bound to the electrode and that the oxidation and reduction processes are not diffusion limited. The variation of the voltammograms in the case of TBAP electrolyte shows almost linear dependence up to 250 mV/s scan rate. However, at higher scan rates from 250 to 500mV/s, a slight deviation has been observed for each voltammogram, which is attributed to resistive effect on the kinetics of the slow diffusion of ions in and out of the polymer with respect to the fast potential change and also to a probable

resistance occurs during redox processes. In other words, the diffusion of ions can be considered as the rate-determining step, as it is much slower than the electron-transfer reaction. An important aspect is that PProDOP presents a highly capacitive like voltammogram shape, especially in the presence of LiBTI electrolyte, with fast and efficient switching. This is likely due to the size effect of the ions, especially during the electrochemical synthesis, and how the size of the ions influences the morphology of the polymer.

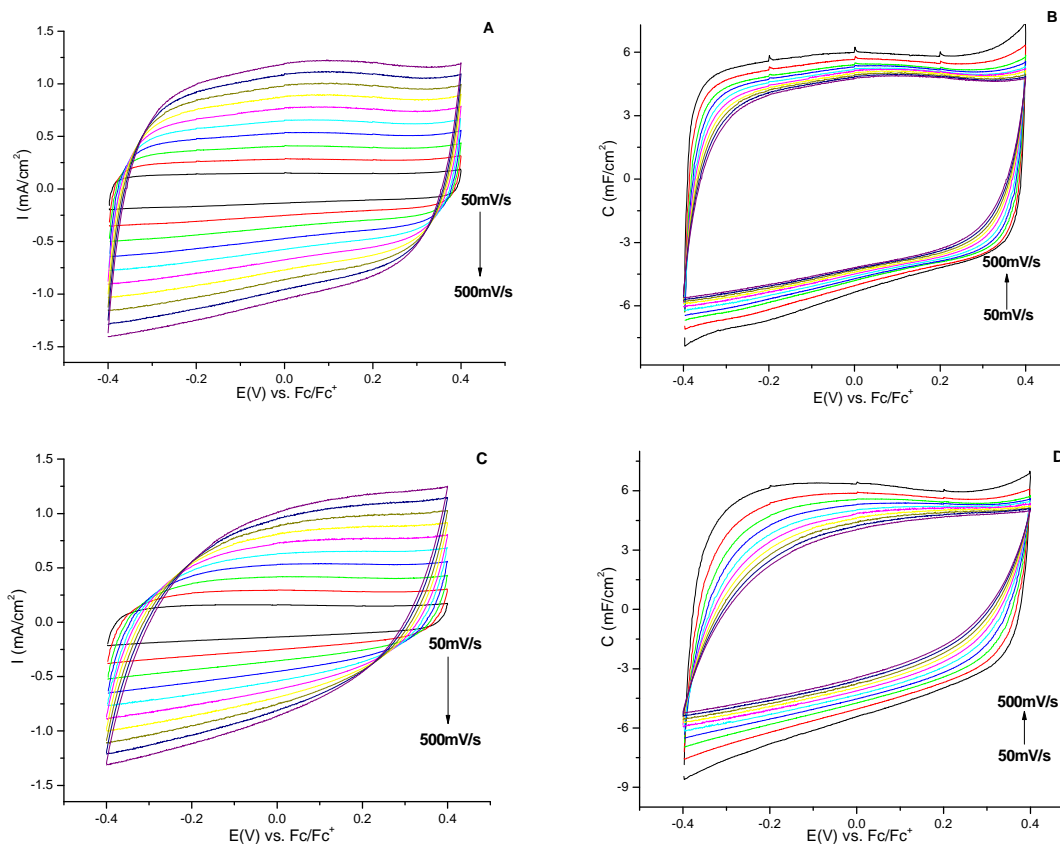


Figure 3-3. A&C) Cyclic voltammograms and B&D) capacitances as a function of applied potential of PProDOP films on Au/Kapton substrates in A&B) LiBTI/PC and C&D) TBAP/PC at 50 to 500mV/s with 50mV/s intervals.

Fig. 3-3B&D shows the capacitance as a function of potential at scan rates from 50 to 500mV/s. In Fig 3-3B&D, the capacitances of the films were obtained by using the relationship; “ $C=i/s$ ” (Equation 2-2), where “ $i$ ” is the current density ( $A/cm^2$ ) and “ $s$ ” is the sweep rate (mV/s). Moreover, the average capacitance of each polymer film, determined as the ratio of the

average charge density, integrated from the cyclic voltammograms, involved in the charging and discharging process over the potential range. The equation dictates that the capacitances calculated for each voltammogram to be independent of the scan rates. In the Figure 3-3, a decrease in the capacitances with increasing scan rates can be attributed to the unavoidable resistance occurrence during redox switching of the polymer. Overall, the results show efficient switching with reasonable fluctuations of the values in the limits of experimental errors.

PProDOPs present an almost ideal ratio of 1 of the anodic to cathodic peak currents ( $i_{pa}/i_{pc}$ ) even at a scan rates as high as 500mV/s, which illustrates the outstanding reversibility of PProDOP's redox processes. Its capacity to be switched in highly reversible manner at high scan rates is rather unusual for conducting polymers. This phenomenon might be stem from the high conductivity of PProDOP films. Electrochemically prepared films of PProDOP have been reported to exhibit conductivities of 95 S/cm with a variability of about one order of magnitude depending on the polymerization conditions, dopant ion, and film thickness.<sup>120</sup> This fine conductivity of PProDOP is probably due to a relatively planar polymer backbone with no substituent units, along with a negligible steric hindrance between adjacent units.<sup>145</sup> This allows for better packing of the monomer chains, allowing efficient  $\pi$ -stacking and consequently enhancing the material's conductivity via interchain hopping (the mechanism of charge percolation). This also suggests that PProDOP has a long effective conjugation length with limited defects that could localize charge carriers.

### **Surface Analysis of PProDOP**

The structures of the PProDOP films on Kapton/Au electrodes (1cm<sup>2</sup>) were examined using a scanning electron microscope (SEM). SEM images of polymer films deposited under constant potential polymerization conditions in the presence of electrolytes LiBTI and TBAP in PC are shown in Fig 3-4 and Fig 3-5 respectively. The prepared films were reasonably smooth as

viewed by the eye. The SEM studies were aimed to gain insight into the fine structure of the films. A 45° tilted angle sample holder was used in order to improve the quality of the topographic images obtained.

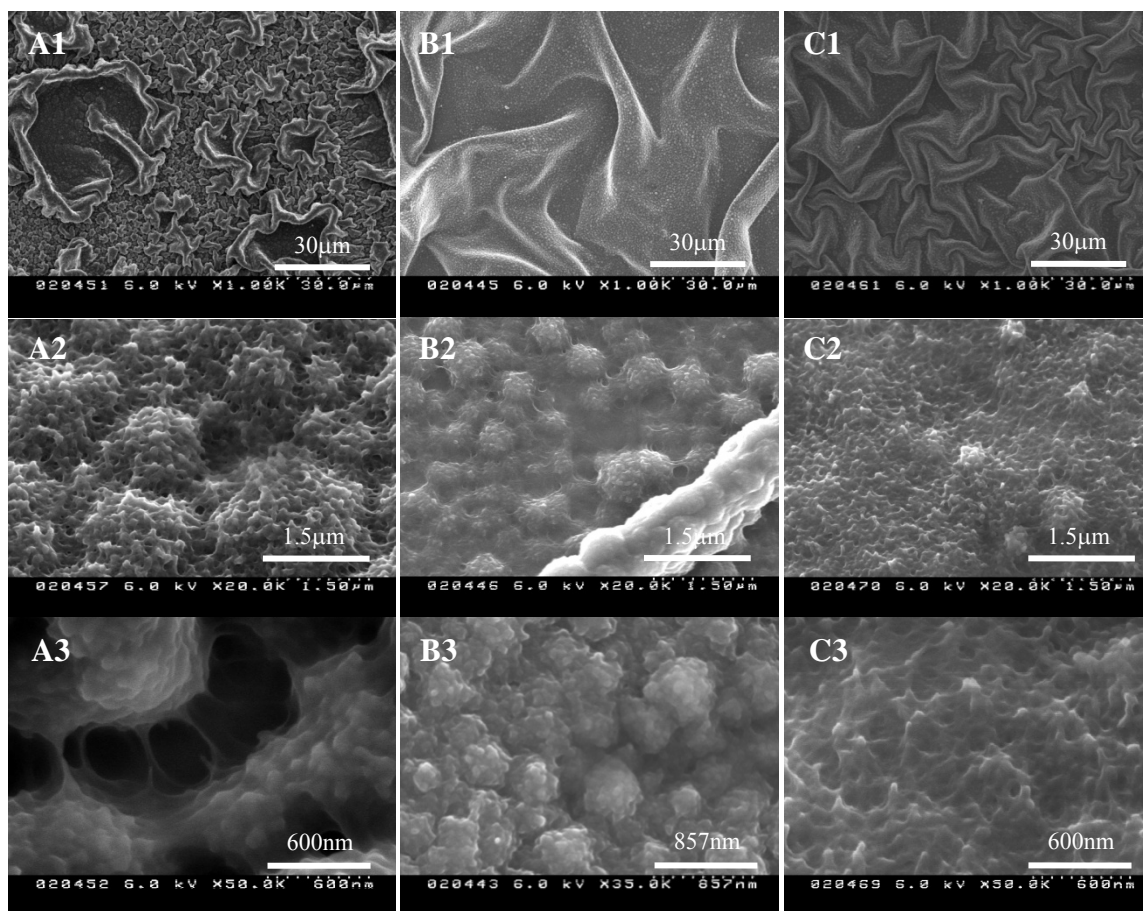


Figure 3-4. Scanning electron micrographs of PProDOP films on Au/Kapton, deposited at potentials A) before, B) at and C) after the  $E_{ox}$  of PProDOP in LiBTI/PC from low to high (A1 to A3, etc.) magnification.

The films prepared with LiBTI were found to be highly porous with a large interconnecting network of polymers, as revealed by SEM images shown in Fig 3-4. In order to observe the influence of the polymerization potential on the morphology of the resulting film, samples were deposited using various potentials. PProDOP films were deposited at the monomer oxidation peak potential ( $E_{p,m} = +0.65$  vs  $Fc/Fc^+$ ), plus 0.05V and minus 0.05V. Fig 3-4 presents SEM images for each polymerization potential from low magnification to high magnification

(A1 to A3, etc.). In the low magnification SEM images, the film resembles a folded blanket covering the electrode surface. For each polymerization potential the films were overlaid into ridges and valleys to varying degrees as seen in Fig 3-4 A1, B1 & C1. Increasing the magnification, the films prepared at the potentials below and above the monomer oxidation peak potential were found to be highly porous with a large interconnecting network of polymers, as revealed by SEM images shown in Fig. 3-4 A1&A2 and C1&C2, respectively. Clearly, there are a large number of micro and nano sized pores present in the network of PProDOP. This large surface area, highly porous structure provides easy access to the dopant ions. In Figure 3-4 B2&B3, the high magnification SEM images of the films prepared at the monomer oxidation peak potential are shown. In contrast with the other films, these films show less porous morphology, however, a large continuous network still exists. There was not any major difference observed between the cyclic voltammograms of these three PProDOP films prepared with LiBTI at different potentials.

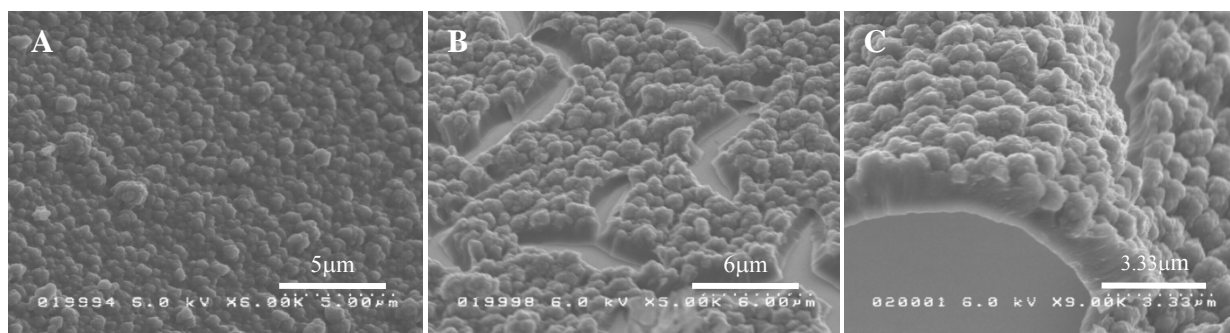


Figure 3-5. Scanning electron micrographs of PProDOP films on Au/Kapton, deposited in TBAP/PC at varied magnification.

Furthermore, the films prepared in the presence of TBAP are shown in Fig 3-6. These films are polymerized at a potential of the monomer oxidation peak potential plus 0.05V. SEM images of the resulting films revealed completely different morphology than PProDOP film prepared with LiBTI. The nature of the electrolyte used during the deposition strongly influences

the morphology of the resulting film as shown in Fig 3-4 & Fig 3-5. A more packed, nodular structured continuous layer of PProDOP-TBAP films relative to PProDOP-LiBTI films are immediately evident in Fig 3-6 A&B. One of the most likely causes for formation of this packed structure is the ion size and the interaction of these ions with the solvent swollen polymer during electropolymerization. Cracks that developed throughout the film during the drying process are evident. The splits in film reveal the smooth gold substrate surface underneath, which shows that the polymer film was not directly attached to the electrode surface at all points. The SEM image in Fig. 3-5C shows a magnification of the rising broken piece of ridge of the film. This packed texture, along with the poor attachment to the electrode surface, correlates with the electrochemical response of PProDOP-TBAP films shown in Fig 3-3. The resistant behavior seen on the cyclic voltammograms of the films with TBAP compared to LiBTI salt, especially at higher scan rates, is possibly due to this packed structure of the film preventing easy access of the ions, unlike the accessible porous morphology, and also likely influenced by the decreased electrical conductivity of the film. As a result, SEM analyses of the films prepared at various conditions indicate that the conditions during electrochemical polymerization method and the nature of the electrolyte strongly influence morphology.

### **Capacitances of the PProDOP Films on Gold Electrodes**

Besides obtaining smooth and homogeneous polymer films, one of the advantages of potentiostatic deposition technique is the control of the amount of charge passed during the deposition process. The charge density applied to the system during polymerization, given the electrochemical systems, reproduced with identical concentrations and compositions, determines the amount of PProDOP film deposited on the electrode. As mentioned earlier, the film deposition can be terminated once a certain amount of charge has passed, so the desired mass of the polymer can be conveniently controlled. In order to relate the deposition charge passed with

the resulting mass of the polymer, a simple calibration graph was prepared, as shown in Fig 3-6a. Moreover, another calibration plot that relates the capacitance obtained from varying amount (or thicknesses) of PProDOP with the corresponding mass of the films was prepared as shown in Fig 3-6B. The latter graph is more convenient for this work since the charge density monitored during the deposition process depends on several parameters like concentrations of species, temperature, etc. therefore, experimental errors are unavoidable. However, once the polymer films were obtained, the amount of capacitance is definite for the amount of material for various films. So when a certain capacitance value was obtained from any random PProDOP film, the amount of PProDOP would be easily determined from the calibration plot.

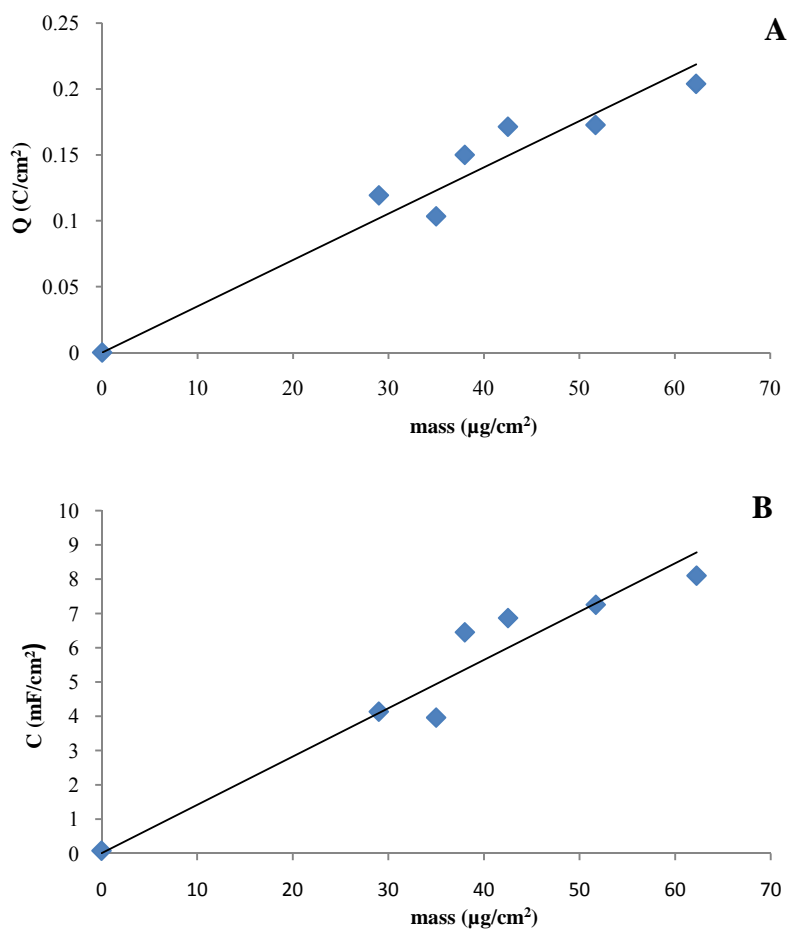


Figure 3-6. Calibration curves: A) Deposition charges of ProDOP and B) capacitances of PProDOP as a function of the mass of PProDOP on Au/Kapton substrates.

In theory, calibration curves would be expected to be linear and the capacitance ( $\text{mF}/\text{cm}^2$ ) would increase linearly with increasing mass of charge storage material. A linear relation was observed between the charge consumed for electropolymerization and also the capacitances of the resulting films and the mass of them. However, after a certain amount of material was deposited, the films became less stable and tended to delaminate from the gold surface after several switching cycles between oxidized and reduced states. This was not unexpected, as charging and discharging processes in redox reactions based on pseudocapacitive materials involve ion intercalation and depletion due to the electric neutrality requirement, which results in volume expansion and contraction of the conducting polymer systems. As a result, the film starts to delaminate from the electrode substrate as it gets progressively thicker. In conclusion, only relatively thin PProDOP films could be grown coherently, as further electropolymerization lead to poorly or non-adhered polymers films on the substrate.

In Fig 3-6B the capacitances ( $\text{mF}/\text{cm}^2$ ) obtained from the gold electrodes holding varying amount of PProDOP were demonstrated as a function of mass of PProDOP. A very small intercept of the plot arises from the double-layer charging of the bare gold electrode. The highest capacitance values obtained from PProDOP films on gold electrodes were found to have capacitance of  $8.1 \text{ mF}/\text{cm}^2$ . From the slope of the graph, the overall specific capacitance of PProDOP on gold electrodes was calculated as  $141 \text{ F}/\text{g}$ . Although PProDOP films displaying smaller capacitances than  $4 \text{ mF}/\text{cm}^2$  probably holding less than  $\sim 30 \mu\text{g}/\text{cm}^2$  were prepared, the mass values of those films could not be measured accurately due to the very small mass deposition. On the other hand, the films having larger amount of PProDOP were observed to delaminate from the electrode surface during the washing processes or upon several cycle switching.

The capacitance value of supercapacitor materials are usually reported in the literature as specific capacitance which is the capacitance per mass of the material (F/g). However, focusing only on the “mass specific capacitance” in the evaluation of supercapacitor electrode materials might be misleading.<sup>146</sup> As mentioned above, in theory the capacitance ( $\text{mF}/\text{cm}^2$ ) of an electrode would increase linearly with increasing the amount of the charge storage material. The charging and discharging processes of conducting polymers involve the insertion and expulsion of ion during the doping and dedoping processes. Besides the mass of the material, the thickness, the conductivity, the porosity of the polymer and the diffusion of the ions also play an important role in the kinetics of the charging and discharging process. Therefore, the switching process would become restricted by kinetics after certain amount (or thickness; the thickness of the material on an electrode substrate of a given surface area is directly proportional to the mass) of polymer has obtained. As a result, it is not always possible to gain higher capacitance values by just simply increasing the mass of the material after the thickness has reached the kinetic limit.

The specific capacitance of a certain mass of PProDOP with the ideal morphology, which is expected to exhibit doping and dedoping redox processes without any kinetic limitations, is calculated by using Equation 2-7. The theoretical specific capacitance of PProDOP is found as 173 and 208 F/g for the doping levels of 0.25 and 0.3, respectively. Accordingly the calculated theoretical capacitance of PProDOP was found to be somewhat larger than the experimentally obtained capacitance of 141 F/g, suggesting the presence of a portion of the polymer film that is incapable of undergoing the redox reactions, due probably to the partial lack of uniformity, open morphology or the presence of defects.

Ideally, the calibration curve relates “the area capacitance” ( $\text{F}/\text{cm}^2$ ) and the amount of the polymer would be expected to initially increase and after reaching the kinetics limits, to level out

(stabilized) at certain capacitance. On the other hand, the graph relates “the mass capacitance” (or specific capacitance) (F/g) and the amount of the polymer would be expected to be stable and decrease at the kinetic limit of the electrode. Consequently, evaluation of capacitance of a supercapacitor material must be done using by both mass and areal capacitance values. While mass capacitance gives intrinsic information about the material, the areal capacitance measures the practically accessible capacitance over a unit geometric area of the electrode substrate.<sup>147</sup> Hence, for device fabrication issues, “the areal capacitance” is of greater practical importance since its value reflects the utilization of the polymer material effectively on a certain electrode substrate.

### **Type I Supercapacitor Devices with Gold Substrate**

Fig 3-7 illustrates the Type I supercapacitor device design which utilizes the same p-doping conducting polymer in a symmetric configuration on both positive and negative electrodes.<sup>74</sup> It can be seen that Kapton-Au sheets (1cm<sup>2</sup>) were used as the current collector material and two of these substrates were coated with a film of PProDOP and sandwiched together using a gel electrolyte (LiBTI based) as the conductive media. A porous separator paper was used to prevent possible shorts between the electrodes in the devices. PProDOP films were made by electrochemical polymerization. One polymer film was initially set in the fully oxidized state and laminated with a fully neutralized film to establish the initial charge state of the capacitor. Subsequent discharging of the device causes half neutralization of the p-doped films proceeding with concurrent half oxidation of the cathode films in the device. For two-electrode systems, the quantity of charge that leaves one electrode is equal to that injected onto the other electrode charge. Therefore, it is essential to match charge capacity of each electrode, thus the amount of deposited polymers on each side prior to device construction in order to achieve

optimal and balanced switching, so no over accumulation of charges would occur when the device was switched between its charged and uncharged states.

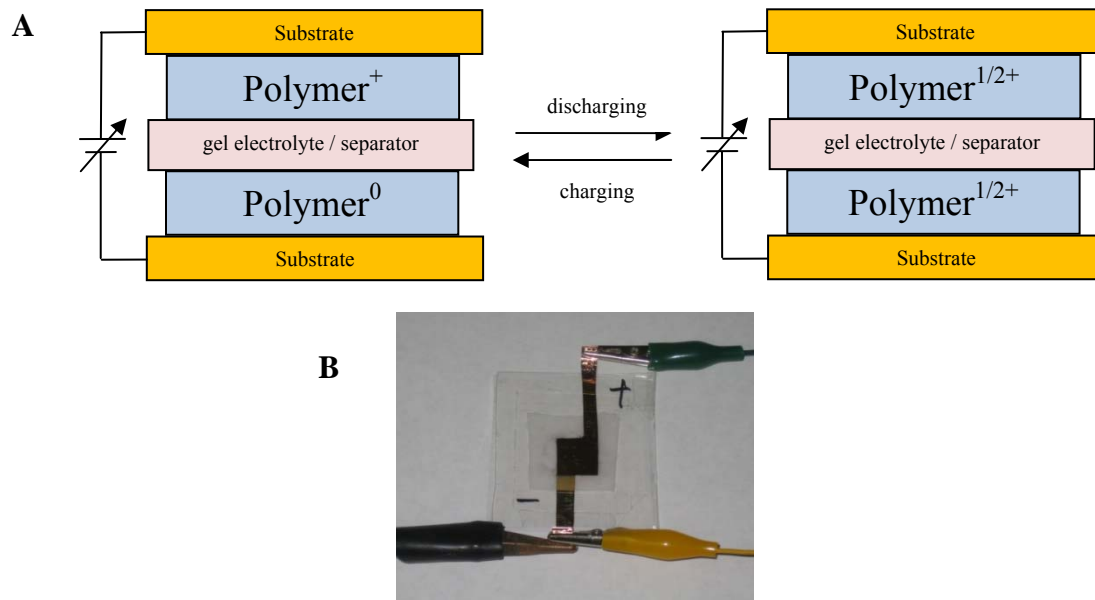


Figure 3-7. A) Schematic diagram of Type I supercapacitor configuration utilizing PProDOP switching between charged and discharged states and B) Photograph of Type I PProDOP supercapacitor with Au/Kapton substrate.

Fig 3-8 shows the linear sweep voltammograms and capacitance as a function of applied potential for the capacitor cells made using LiBTI gel electrolyte at different scan rates from 50 to 250mV/s with 50 mV intervals. The capacitance of the devices was calculated using the relationship:  $C=i/s$  (Equation 2-2). In the Type I device, there is a complete overlap between the voltage ranges of oxidation/neutralization of anode/cathode electrodes since both electrodes utilizes the same polymer. Thus, the cyclic voltammogram of an ideal Type I supercapacitors would typically have a rectangular or parallelogram shape, showing a constant current within the operating voltage window of the device. In the PProDOP based supercapacitors, the cyclic voltammograms taken at the sweep rates from 50 to 250mV/s are almost close to an ideal shape of rectangle as shown in Fig 3-8A. Such rectangular shape at a constant scan rates is a

characteristic of a potential independent constant capacitive behavior. The linear scan rate dependence is indicative of non diffusion limited redox switching and the good conduction with the gold substrate. Even for higher scan rates of 250mV/s as shown in Fig 3-8A, the rectangular behavior can be observed, which is the indicative of fast switching rate of ions at the sites of electrode/electrolyte interfaces. This result also shows that LiBTI based polymeric gel electrolyte act as good conductive media between the electrodes without any major resistive effect on the kinetics of the diffusion of ions. Moreover, the capacitance response of the device has been found to be independent of scan rates, as can be clearly seen from the Fig 3-6B, which is expected due to the equation of capacitance. In conclusion, these voltammograms demonstrate that PProDOP devices show excellent capacitive behavior with fast and efficient switching.

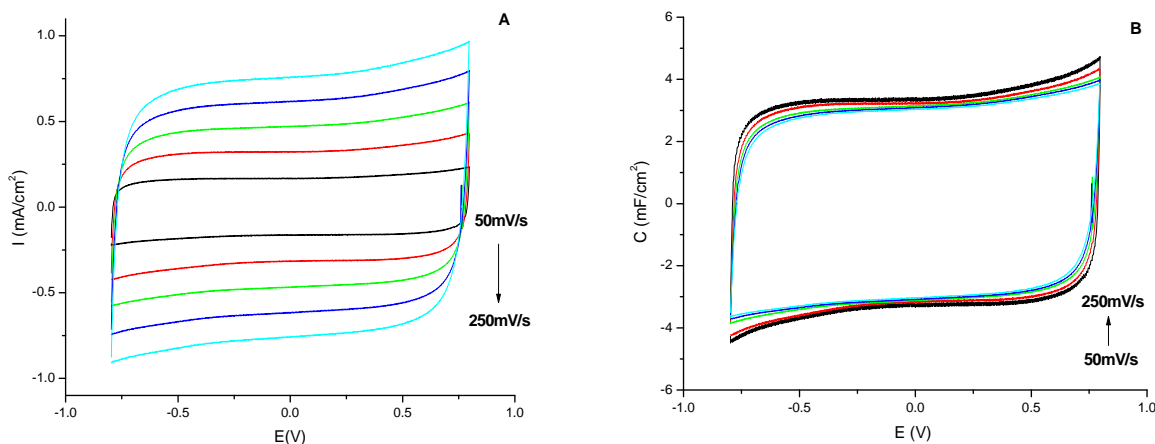


Figure 3-8. A) Cyclic voltammograms and B) capacitances as a function of applied potentials of Type I PProDOP supercapacitor with Au/Kapton substrates using LiBTI gel electrolyte at 50 to 250mV/s with 50mV/s intervals.

The capacitance obtained from a PProDOP supercapacitor was calculated as 3.2mF/cm<sup>2</sup>. The film capacitances are measured as 8.1mF/cm<sup>2</sup> and the corresponding mass value was calculated from the calibration plot. Finally the specific capacitance of the device was calculated by dividing the capacitance of 3.2mF/cm<sup>2</sup> to the total mass of PProDOP on both positive and negative electrodes. The specific capacitance of the device shown in Fig 3-8 was as 30F/g.

The equivalent circuit of a two-electrode supercapacitor consists of two electrodes connected in series, so the equivalent capacitance value is given by the reciprocal of the sum of the reciprocals of the individual capacitance values of the two electrodes. This relationship is shown in Eq 3-1 as follows:

$$C_{device} = \left[ \frac{1}{C_1} + \frac{1}{C_2} \right]^{-1} \quad (3-1)$$

where  $C_{device}$  is the capacitance of the device,  $C_1$  and  $C_2$  are capacitances of the positive and the negative electrodes, respectively. Since the systems presented in this work contain the same polymer on each side, the equation predicts that the specific capacitance of the device,  $C_{device}$  will be one half of the capacitance of the individual film electrodes. The measured capacitance ( $3.2\text{mF/cm}^2$ ) of the device was found to be in agreement with the expected value ( $4\text{ mF/cm}^2$ ). The difference between the measured and the calculated capacitance of the device was attributed to a substantial value of equivalent series resistance (ESR), present in real capacitors, especially using gel electrolyte systems as the conducting media.

Moreover, PProDOP supercapacitors can be biased in the reverse direction with respect to the positive electrode. As was mentioned in Chapter I, there is almost a complete overlap between the redox potentials of the anode and cathode redox processes in Type I devices. Therefore, the cyclic voltammogram of an ideal Type I supercapacitors would be a rectangular plot, so Type I supercapacitors can be reverse biased because there is no polarity between the electrodes. The voltammograms shown in Fig 3-8 demonstrates this phenomenon since the device was scanned between  $+0.8\text{V}$  and  $-0.8\text{V}$ , showing no difference in voltammograms between the anodic or cathodic scanning. The voltammograms show almost mirror images of each other in the positively and negatively biased directions.

The energy density of the device, shown in Fig 3-8, was calculated using the relationship; “ $E = \frac{1}{2} QV$ ” (Eq 1-2). The average charge density was determined from the cyclic voltammograms and the average voltage of the device was taken as the half of the potential difference between the electrodes at the initial charged state of the device (Equation 2-8) since this difference decays to 0V as the device discharges. The total mass of films on both electrodes were calculated from the calibration plot (Fig 3-6B). The energy density was found as 2.6Wh/kg. Moreover, the corresponding power density was determined using the relationship: “ $P = iV$ ” (Equation 2-9). The average current density was determined from the cyclic voltammograms. The power density of the supercapacitor was calculated as 584W/kg. Since conducting polymer based supercapacitors are analogous of battery systems, the energy and power densities calculated for PProDOP devices, match in the battery vicinity in the electrochemical supercapacitor region on the Ragone Plot (Fig 1-1).

### **Stability of Type I Supercapacitor Devices with Gold Substrate**

In a supercapacitor device, stability is of fundamental importance since one of the most important aspects of supercapacitors is the high number of reversible charging and discharging cycles. Some common applications require frequent cycling, with minimal change in the performance, including hybrid-electric vehicles for transient load leveling or capturing the energy used in braking, or starting diesel vehicles. The charging/discharging process in supercapacitors move charge and ions only and does not make or break chemical bonds unlike in a battery. Conducting polymer systems undergo volume expansion and contraction (swelling and shrinking phenomenon) when the oxidation level is changed due to the insertion and expulsion of ion during the redox doping and dedoping processes, respectively. The stability of the PProDOP based supercapacitor devices was examined by exposing the devices to continuous doping and dedoping processes by cyclic voltammetry in a 1V range at a scan rate of 200mV/s, as shown in

Fig 3-9A. A cyclic voltammogram of the device switching was recorded in every 100 switches up to a total of 32,767 switches. The average capacitance for each voltammogram was calculated and plotted as a function of number of cycles. In Fig 3-9B, capacitances are shown as a function of applied potential; very stable and almost constant values of capacitances have been observed for the overall voltage range of the device. Fig 3-9A shows a fast decrease (fluctuation) in anodic and cathodic current responses during the first several hundred cycles. This initial 20% of the capacitance loss is attributed to the so called “break-in” or “conditioning” period, which is typically observed for conducting polymers films, permitting permeation of the electrolyte ions into the polymer, and may be due to the some unavoidable irreversible charge consumption reactions of possible impurities or side reactions of some species. This break-in period is followed by a very slow decrease of capacitance by less than 2% loss of the total capacitance value with over 32,000 cycles. Consequently, the stabilities of the PProDOP devices were outstanding since the total capacitance decreased by less than 20% after few hundred cycles and less than 2% thereafter for over 32,000 cycles. Overall, the devices retained almost 80% of their electroactivity, even after 30000 switches, which is quite attractive for supercapacitors.

It should be noted that the all the experiments were conducted on a bench top at ambient conditions, and as can be seen from the photograph of a PProDOP supercapacitor in Figure 3-7B, no special procedures were applied to seal the device. Only regular adhesive tape was used to cover the corners of the transparency sheet that covered the electrodes. Since all components of the device system, from electrodes materials to separator papers, contribute to the overall stability, this high cyclic stability of the PProDOP supercapacitors even without an air-free sealing procedure indicate that a further optimization of each component of the device will allow even more stable switching with less loss of capacitance.

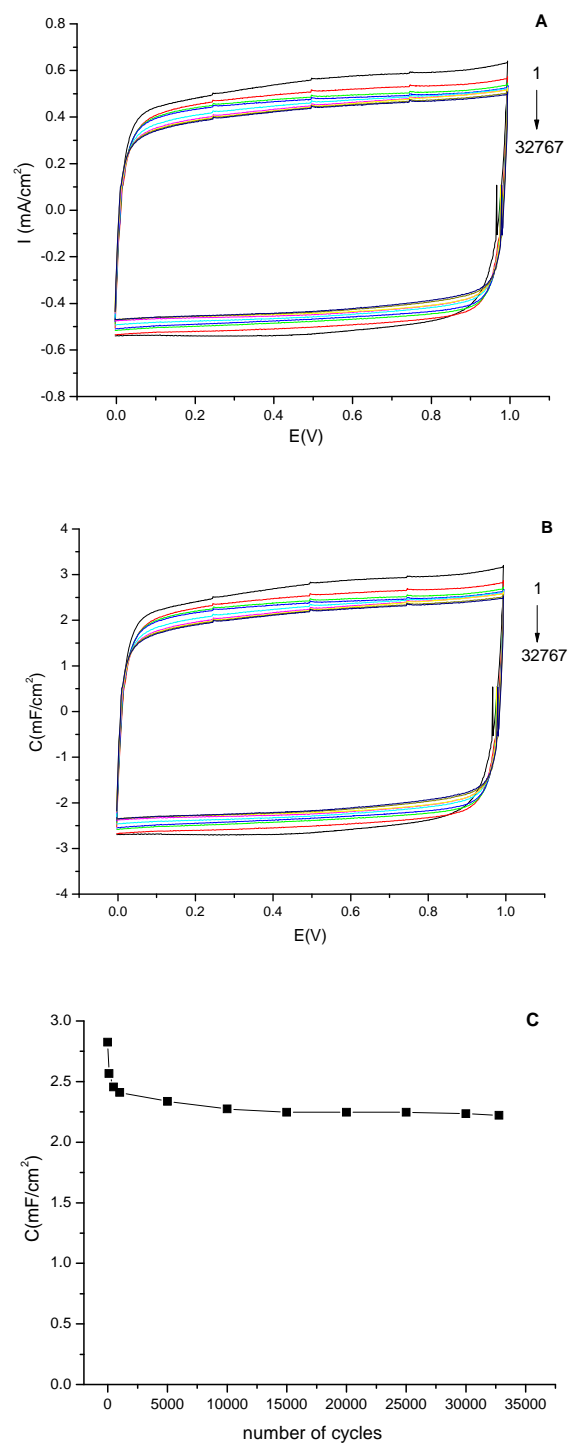


Figure 3-9. Stability of Type I PProDOP supercapacitors with Au/Kapton substrates using LiBTI gel electrolyte by non-stop cycling at 200mV/s; A) cyclic voltammograms, B) capacitances as a function of applied potentials and C) capacitances as a function of number of switching cycles (1<sup>st</sup>, 100<sup>th</sup>, 500<sup>th</sup>, 1000<sup>th</sup> and every 5000<sup>th</sup> cycle).

## SWNT Films as Electrode Substrates

Conventional conducting polymer based supercapacitor research has widely focused on metal substrates, for example; gold electrodes. As mentioned throughout the text, the long term stability of conducting polymers can be compromised by the delamination of the conjugated polymer from the metal surfaces as a consequence of strain cycling.<sup>148</sup> Swelling and shrinking of a conjugated polymer causes the polymer to pull itself from the surface, which leads to reduced electrochemical responses and eventually delamination and degradation of the polymer film during cycling.<sup>12</sup> Also, gold itself can easily delaminate from the surface of plastic substrates through solvation or stress. In a supercapacitor device, a higher the amount of material leads to a higher capacitance for the device. Therefore, in addition to a gold electrode, using a high surface area electrode with a porous structure seemed to be an effective approach toward deposition of higher amount of polymer material per unit area, thus improved capacitance. As such, single wall carbon nanotube films have the potential to replace and possibly outperform gold electrodes in supercapacitors due to their high conductivity, strong affinity for plastic and glass substrates, large surface area for charge injection into the polymer matrix, mechanical flexibility, chemical inertness, and large electrochemical potential windows.<sup>149, 150</sup> Since the polymer itself is a porous material, the three-dimensional SWNTs network would offer more active sites for the electroactive polymer matrix to penetrate, possibly leading to faster switching and more stable devices. The major motivation of this approach was to design optimal electrode material for supercapacitors, taking advantage of the porosity of SWNT network electrodes to obtain higher capacitances. The use of SWNT films as current collectors would allow effective switching of higher amount of CPs by increasing the adhesion of PProDOPs to the substrate within which the polymer is mechanically interlocked, as well as enhancing the stability of device. Previous research has involved the coating/wrapping of nanotubes with conjugated polymers to increase

the capacitances of SWNTs.<sup>16</sup> In this work, SWNT films were conceived to provide structural support (much as soil serves as a support to anchor plants via their roots) to deposit higher amount of PProDOP. Moreover, the supercapacitor electrodes are generally used as coatings of active material mixed with binders. In our approach of using porous network of SWNTs as current collector, the binding element is eliminated which has a negative effect on the overall capacitance due to the increased contact resistance between the active material and the current collector and also the increased total mass of the cell. In this work, SWNTs films are used as supportive electrodes and current collectors for the conductive polymer matrix for the first time.

### **SWNTs Film Preparation**

Single wall carbon nanotube films were prepared via a method developed in the group of Prof. Rinzler (UF Physics).<sup>41, 151</sup> SWNTs grown by laser ablation were used in this study. Purified SWNTs were suspended in an aqueous 1% Triton-X-100 solution with a nanotube density of 0.001 mg/mL by ultra-sonication. Triton X-100 solution acts as stabilizing agent to suspend the nanotubes. Then this dilute surfactant based well dispersed suspension of purified nanotube solution vacuum-filtered through a membrane (Millipore, VCWP, 100 nm pore) as illustrated in Fig 3-10. After the nanotube films were deposited evenly on the membrane surface, the films were washed away with DI water several times to remove the residual surfactants. The amount and thickness of the nanotube films were controlled by the density and the amount of the nanotube suspension solution used. Unless otherwise is indicated, the nanotubes used for this study were 80nm in thickness. Once these highly uniform films on the filtration membrane were dried, they were cut into desired shapes (area of 1cm<sup>2</sup> in this case) and the electrodes prepared by transferring these films to glass or plastic substrates. The ends of the substrates were previously coated with Cr/Pd as contact pads by either sputtering or thermal evaporation. This procedure is as follows: the membranes were applied to the substrates face to face in contact with Cr/Pd from

the edge of the nanotube films and then were placed onto a previously wetted Teflon block. They were sandwiched in between several filter papers for cushioning and pressed between two metal bricks by spring clamping and left in 80°C oven over night. As the water evaporates, the nanotube films firmly adhere onto the substrate. Finally, the dried substrates were removed away from press and the cellulose ester membranes were completely removed by dissolving in acetone vapor (or methanol) bath followed by washing repeatedly in 8 fresh acetone baths to ensure the removal of any residual cellulose ester on the film surfaces. The resulting films were highly uniform and electrically conductive, ranging from 600 to 6,000 S/cm. Moreover they were highly thermally and chemically stable. To minimize contamination from extraneous dust, this procedure was performed entirely in a Class 100 clean room.



Figure 3-10. Fabrication of SWNT Film. Vacuum filtration of a surfactant based suspension of SWNTs, forming the film as a cake on the porous filtration membrane.

As can be clearly seen from the AFM image of the obtained nanotube film shown in the Fig 3-11, they were highly porous and had a large surface area (high specific surface area). The randomly but homogeneously distributed nanotube bundles throughout the film provide sufficient overlapping of nanotubes to result in good electric conductivity. This highly uniform morphology of the films is ideal for use as the electric current collector in polymer based

supercapacitor devices. The porous nature of the films was expected to allow interpenetration of active polymer into the matrix, enhance the amount of deposited polymer and improve the adhesion of the polymer by interlocking the polymer within its matrix. Thus, deeper and faster switching of the devices would be possible. The low mass density of the films would allow higher specific surface capacitances by lowering the mass contribution of the electrode substrates of the device.

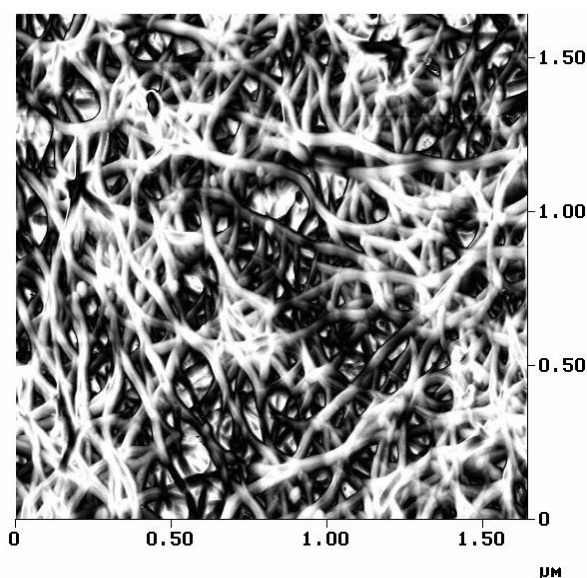


Figure 3-11. Atomic force micrograph of SWNTs film mounted on sapphire wafer.

### **Comparison of Gold and SWNTs Substrates in Device Performances**

After preparation of SWNTs film, ProDOP was electrochemically polymerized onto these substrates. As mentioned before, in order to obtain smooth uniform films of PProDOP as on flat gold substrates, a constant potential electrochemical polymerization method was applied. Moreover, different polymerization techniques of cyclic voltammetry and potentiostatic pulse electropolymerization (for the detailed explanation of this technique go to section 3.13) were applied as well. Once formed on the electrode, the polymer films were thoroughly soaked and rinsed with ACN and equilibrated with monomer free electrolyte solution. As was in gold electrodes, the capacitances obtained from SWNTs based electrodes were found to be in a linear

relation with increasing the PProDOP deposition charge (and number of deposition steps, and mass of the PProDOP). However, very similar to gold electrodes, as the PProDOP film became thicker, the film delaminated from the nanotube surfaces upon washing process. This was surprising since the PProDOP layer was expected to adhere onto the SWNTs substrate better than on the gold electrodes.

In Fig 3-12, cyclic voltammogram and the capacitance graph of the device prepared with SWNTs electrodes using LiBTI gel electrolyte, at scan rates from 50 to 250mV/s with 50 mV intervals are shown. The capacitance obtained with PProDOP on SWNTs electrode devices was found to be 3.8mF/cm<sup>2</sup>, only slightly higher than the gold electrode devices (3.2mF/cm<sup>2</sup>). The voltammograms of the device show typical rectangular shape as was in gold substrate devices. At higher scan rates, more than 100mV/s, the device did not show an efficient switching and a slight deviation from the rectangular shape of the voltammograms has been observed, which is attributed to a substantial value of equivalent series resistance (ESR). These results show that PProDOP probably does not diffuse into the porous network of SWNTs and probably interacts very poorly with the nanotube surfaces.

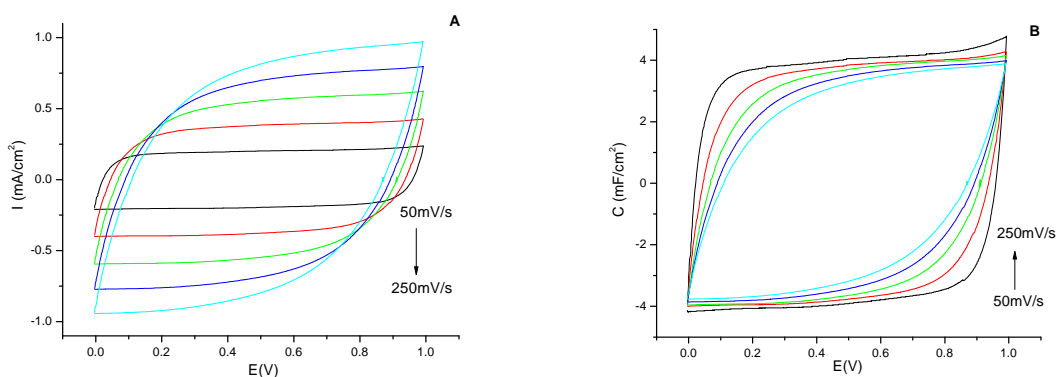


Figure 3-12. A) Cyclic voltammograms and B) capacitances as a function of applied potential of Type I PProDOP supercapacitor with SWNTs substrates in LiBTI gel electrolyte at 50 to 250 with 50mV/s intervals.

Besides linear sweep voltammetry, a constant current charge/discharge technique (chronopotentiometry) was also used to characterize the device performances. The devices were subjected to a cyclic square-wave galvanostatic current, and the voltage response was measured as a function of time. The discharge capacitance,  $C_d$ , was evaluated from the linear part of the discharge curves using the relation:  $C_d = i\Delta t/\Delta V$  (Equation 2-2), where  $i$  is the constant current and  $\Delta t$  is the time interval for the voltage change of  $\Delta V$ . Typical charge/discharge plot of a capacitor usually demonstrates a symmetric linear increase and decrease as a function of time.

Fig 3-13A&B, show the galvanostatic charging and discharging cycling of both gold and SWNTs film based devices, respectively. The devices were charged to 1.0V and discharged at a constant current density of 0.5mA/cm<sup>2</sup>. The IR drops upon discharging in both devices is due to the internal resistance of the supercapacitors. After the IR drop, the discharge behaviors of the devices are linear with respect to time. The capacitance values are calculated as 2.9mF/cm<sup>2</sup> and 3.5mF/cm<sup>2</sup> for gold and SWNTs based devices, respectively. These results are in agreement with the capacitances values calculated from the cyclic voltammograms of the devices. The IR drop observed for gold substrate devices, as shown in Fig 3-13, arises probably from the interfacial resistance between the electrode/electrolyte contacts and penetration of electrolyte into the polymer matrix. The doping and dedoping process is a relatively slow reaction compared to electronic charging. As a result the IR drop appears upon switching of the device, which is also seen in the cyclic voltammograms as the deviation of the shape with the increased scan rates. However in Fig 3-13B, the IR drop observed in the SWNTs based device is higher than the gold device, showing the higher internal resistance in the device. This internal resistance most probably arises because of the interfacial resistance between the charge storage material (PProDOP) and the electrode substrate (SWNTs film). Moreover, a decrease in the total

discharge time of the devices with the SWNTs substrate devices, compared to gold substrate devices, was observed for the same current density application. This feature can be attributed to increased accessible surface area of the substrate so the total electrode area in contact with PProDOP. As a result, SWNTs based devices respond faster to discharging, however create a high resistance inside the cell.

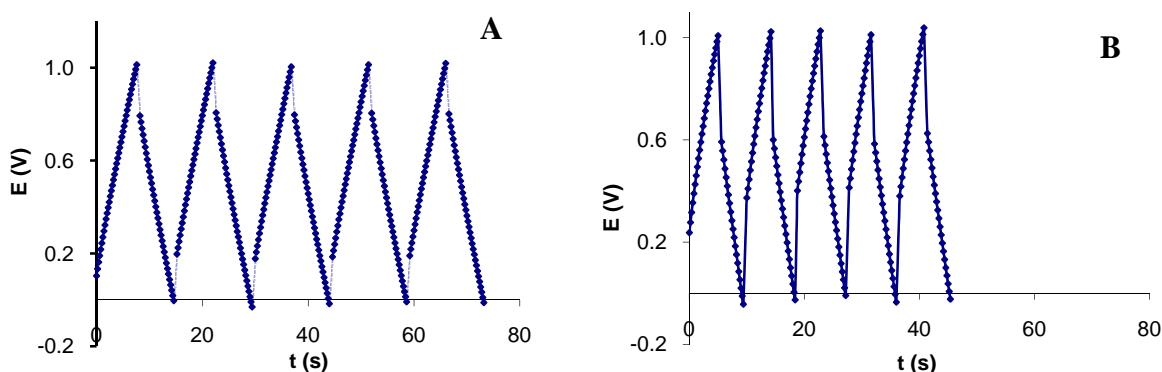


Figure 3-13. Constant current ( $0.5\text{mA}/\text{cm}^2$ ) charging/discharging of Type I PProDOP supercapacitor with A) Au/Kapton and B) SWNTs film substrates.

### Non-Covalent Modification of SWNT Surfaces with Sticky-PF

The delamination of the PProDOPs upon electropolymerization suggests that the coordinative interaction of the polymer with the electrode surface is poor, therefore it is surmised that the surface of carbon nanotubes, due to their low energy graphene nature, would only weakly interact with conjugated polymers through  $\pi$ -stacking interactions. Some recent research studies have also shown that conducting polymers exhibit poor adhesion and mixing with nanotube materials due to nanotubes' low energy graphene surfaces.<sup>152</sup> Furthermore, PProDOP is polar and mildly hydrophilic, whereas SWNTs are hydrophobic, and PProDOP is sterically encumbered due to the bulkiness of the alkylene bridge, so its interfacial adhesion via van der Waals interactions with the surface of a SWNT is poor. Due to this lack of affinity, shear stress, bending, other mechanical deformations, as well as electrochemically induced morphological

changes (which has been previously observed for polypyrrole and PProDOP)<sup>153</sup> induces poor adhesion of the polymer to the surfaces of nanotubes and finally delamination of the polymer from the nanotube film substrates, thus destroying the device.

The major motivation for using SWNT films as substrate was to increase the adhesion of higher amounts of PProDOP to the substrate within which the polymer is mechanically interlocked by taking advantage of the mesoporosity of SWNT network electrodes. In order to fully utilize the advantages of porous network of SWNTs, and also to realize the benefit of SWNTs as current collectors with high charge dynamics and long term stability in supercapacitor performance, it was necessary to electrically couple the active polymer strongly to the nanotube surface. Such electrical coupling requires intimate proximity between the organic layer and the nanotube surface. To accomplish this, we present a novel method of introducing an interfacial compatibilizer (a buffer layer) between the PProDOP and the SWNT surfaces, which would overcome the aforementioned interfacial challenges, and significantly improve polymer adhesion to the substrate and thus improve the device performance. This method involves non-covalent functionalization of carbon nanotube surfaces through polycyclic aromatic hydrocarbons, specifically pyrene derivatives to improve the interface between nanotube surfaces and organic molecule.<sup>154</sup> Such non-covalent interaction with the nanotubes permits association of other molecules with the nanotubes while minimally impacting their intrinsic electronic transport properties.<sup>155</sup> A polyfluorene derivative; poly (9,9-dioctylfluorene) with pyrene pendant groups (Sticky-PF)<sup>122</sup>, whose structure is illustrated in Fig 3-14 with the proposed non-covalent association on the surface of nanotube, was synthesized by Dr. Ryan Walczak in the Reynolds group. Thereby this compatibilizer layer would allow an increased association of the electroactive PProDOP to the SWNT electrode surface.

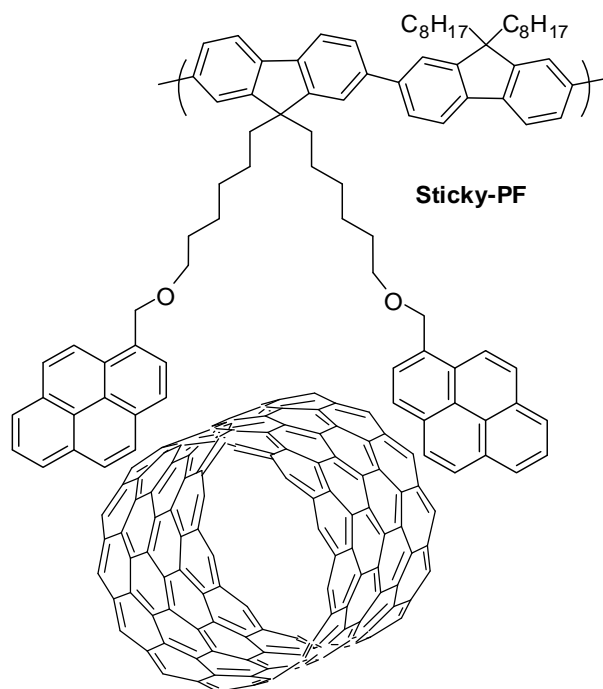


Figure 3-14. Structure of poly(9,9-dioctylfluorene) (Sticky-PF) and its proposed non-covalent association with a SWNT surface.

The utility of non-covalent functionalization, as opposed to irreversible covalent functionalization, is that small molecules or polymers can be associated with the nanotube surfaces without significantly altering the nanotubes' electronic properties. This non-covalent functionalization can be achieved by the attachment of a polycyclic aromatic hydrocarbon such as pyrene to the molecule desired for attachment.<sup>156</sup> Furthermore, Sticky-PF were designed to have sufficient plurality of polycyclic aromatic hydrocarbons as pendant groups along a polymer chain, so the association/dissociation kinetics attributed to single molecules would be sufficiently attenuated as to render the polymer association with the carbon nanotube side wall, for all intents and purposes, permanent. The octyl functionalities were coupled to the polyfluorene backbone to increase the solubility of the polymer in common solvents for ease of application processes.

The deposition of Sticky-PF was achieved by immersion of the bare SWNT films into a solution of Sticky-PF/Chloroform (0.5mg/mL) overnight, where the polymer would

spontaneously assemble onto the nanotubes, followed by subsequent soaking of the film in pure chloroform for several hours to remove unadsorbed material, then repetition of the same procedure one more time, followed by washing with methanol. These films were then used as electrodes for electrochemical deposition of PProDOP. To minimize contamination from extraneous dust, this procedure was performed entirely in a Class 100 clean room. To examine the attachment of Sticky-PF layer on the nanotubes, the surface topography of 7-nm thin nanotube film networks deposited on silicon wafers (witness chips) were measured with AFM. While the nanotubes appeared as thin and smooth bundles before the Sticky-PF coverage as can be clearly seen in the Fig 3-15A, rougher surface of bundles were observed after the solution dipping process of the film to Sticky-PF solution. As shown by AFM image in Figure 3-15B, the adsorption of Sticky-PF onto the SWNT surface was evident by the widened girth of the nanotube bundles, as well as some attached spheroid nanostructures. It is believed that this image demonstrates that a fairly homogeneous monolayer coating was deposited during the self-assembly process. It is also important that the Sticky-PF were adsorbed on the SWNTs only as a thin layer and did not fill up the porous structure between the bundles which would prevent the ProDOP diffusion into the porous network of SWNTs film. For the remainder of research presented in this chapter, all of the SWNT films used were coated with Sticky-PF unless otherwise specified.

In addition to AFM images, the absorbance spectra of self assembled Sticky-PF covered SWNT films are presented in Fig 3-16 with comparison to the solution spectra of Sticky-PF in chloroform. It is obvious that there is a self-assembled layer of Sticky-PF present on the naotubes film since both spectra show the same peaks belonging to the pyrene subunits.

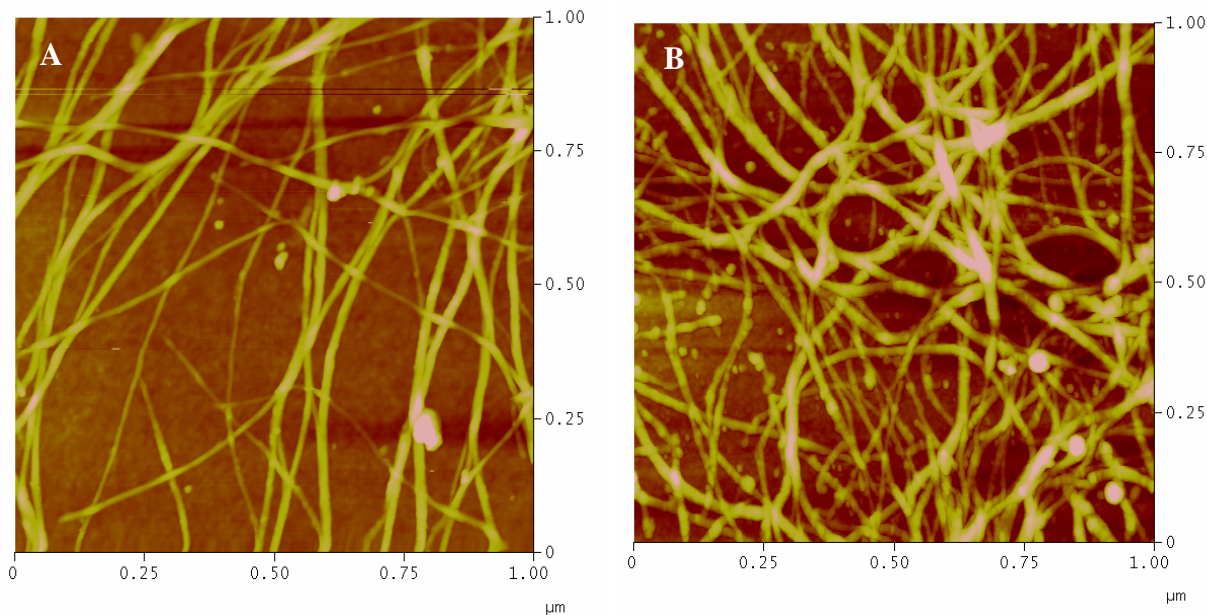


Figure 3-15. Atomic force micrographs of A) SWNTs film on Si wafers before Sticky-PF coating and B) SWNTs film after Sticky-PF coating.

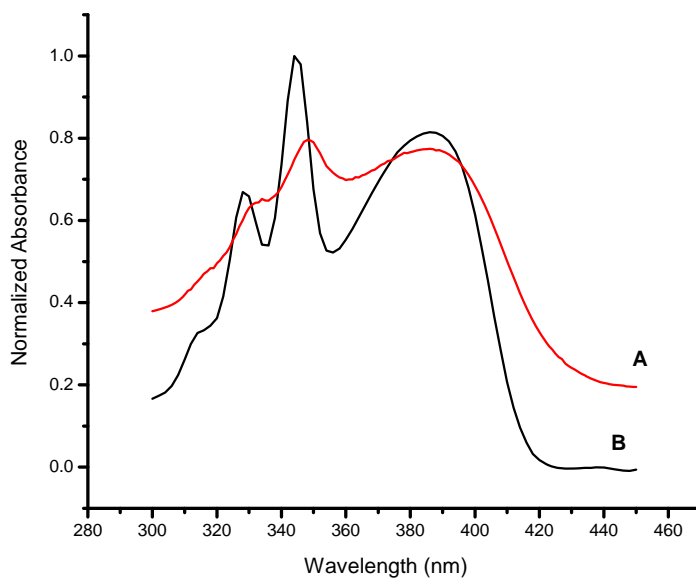


Figure 3-16. Absorbance spectra of A) Sticky-PF coated SWNT film and B) solution of Sticky-PF in chloroform.

The Sticky-PF would be expected to have a negative effect on the conductivity of the nanotubes film, since it is moderately insulating, however the sheet resistances of SWNTs film were found to be very similar as  $92 \Omega/\square$  before and after the Sticky-PF coverage,

respectively. These results show that coating SWNTs with Sticky-PF does not render the film electronically passivated and charge carriers can be tunnel through this very thin adsorbed layer of Sticky-PF. Accordingly, the non-covalent functionalization of carbon nanotube surfaces through pyrene units have minimal impact on the intrinsic electronic transport properties.

### Electropolymerization of ProDOP on Bare and Sticky-PF coated SWNT Films

Cyclic voltammetry offers a powerful method for the characterization of the monomer and polymer redox processes. Since the electropolymerization of ProDOP on gold substrates was already examined, it was necessary to observe this process on the Sticky-PF coated SWNTs electrodes. After coating of the SWNTs film with Sticky-PF using a solution-dipping process, ProDOP was electrochemically polymerized onto these substrates. Figure 3-17 demonstrates the representation of this process.

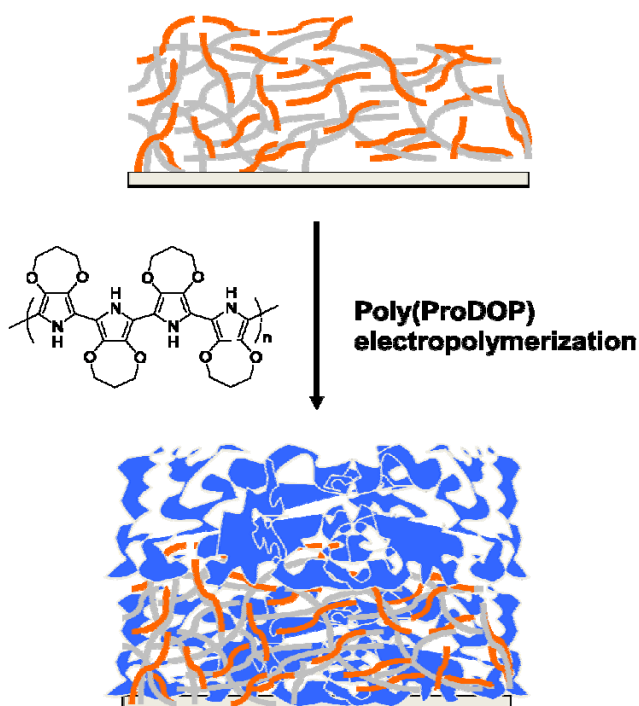


Figure 3-17. Schematic representation of PProDOP electrodeposition onto Sticky-PF|SWNTs film. (grey: SWNTs, orange: Sticky-PF, blue: PProDOP)

PProDOP films were synthesized electrochemically on both bare SWNT film and Sticky-PF coated SWNT film by linear sweep cyclic voltammetry. Fig 3-18 shows the voltammograms at a rate of 25mV/s of these processes on both substrates. Electrochemical polymerization processes are expected to differ slightly from each other when any of the parameters of the system, such as substrate electrodes or solution media are changed. As illustrated in the cyclic voltammograms in Fig 3-18, ProDOP behaves quite differently on a Sticky-PF coated SWNTs film than on a bare SWNTs film. Cyclic voltammogram of ProDOP on Sticky-PF coated SWNTs film show consistent behavior with the ProDOP deposited on gold (Fig 3-2), most notably the irreversible monomer oxidation peak with the absence of a reductive wave which is indicative of radical-radical coupling, and formation of polymeric material.

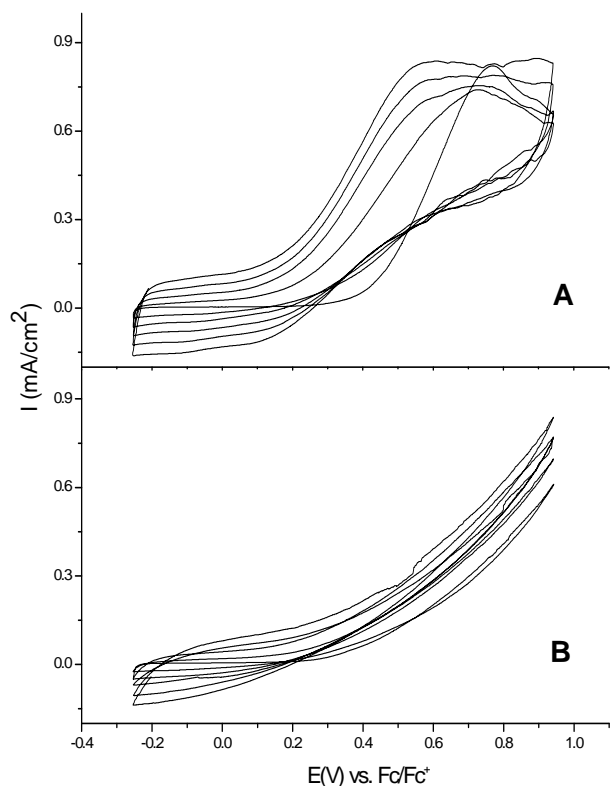


Figure 3-18. Electrochemical polymerization (first 5 cycles) of ProDOP by potential scanning in LiBTI/ACN on A) Sticky-PF|SWNTs and B) bare SWNTs at 25mV/s.

As was observed in electrodeposition of ProDOP on gold electrodes, a shift in the monomer oxidation potential was evident with the progression of each cycle in the case of Sticky-PF coated SWNTs. As explained in the previous sections, this shifting in the oxidation potential might be caused by a combination oxidation of monomers and coupling of soluble oligomers, which have more lower oxidation potential than monomers.<sup>142,143</sup> Moreover, the cyclic voltammetric system, after several repeated polymerizations occurring under identical conditions, the process of adding new polymer to the electrode surface chemically modifies the working electrode. These reasons combine to yield broader and shifted peaks appear with the progression of cycling in the case of Sticky-PF coated SWNTs. Not surprisingly, the oxidation potential of ProDOP ( $E_{p,m}$ ) on Sticky-PF coated SWNTs was found to be 0.76V vs. Fc/Fc<sup>+</sup>, a slightly higher potential than  $E_{p,m}$  on the gold electrode 0.65V vs. Fc/Fc<sup>+</sup>. While the actual process of coating of the SWNTs surfaces with Sticky-PF produces a chemically modified current substrate electrode covered with an essentially insulating polymer, the Helmholtz layer at the electrode surface was expected to be affected, thereby increasing the potential energy required for monomer oxidation due to the addition of a tunneling barrier.

On the other hand, there was no monomer oxidation peak observed on a bare SWNTs film as it was on the other electrodes, yet polymer films were formed on both bare and Sticky-PF coated SWNTs film substrates. As explained earlier, delamination of PProDOP film, when potentiostatically deposited on a bare SWNTs film, was observed during the redox cycling of the film in a monomer-free electrolyte solution. The polymer film was observed to fall from the electrode surface upon washing or after several switches and float in solution. As discussed above, this delamination was most likely due to the inability of the PProDOP film to adhere to the SWNTs to their low energy graphene surfaces.<sup>157</sup> The lack of both a well-defined monomer

oxidation peak and polymer waves in the CV of PProDOP deposition onto the bare SWNT films was probably due to this poor coordination of the molecules with nanotube surfaces. The increased currents due to the repeated scanning demonstrate the formation of a polymer film on both electrodes; however, the nucleation loop seen in the first scan of electropolymerization on Sticky-PF coated SWNTs, corresponding to the presence of adsorbed polymer increasing the working electrode surface area, and also the increased current densities, corresponding the polymer redox process in the case of Sticky-PF coated SWNTs, are indicative of a more efficient electropolymerization. These results were most likely due to the better interaction of the polymer molecules to the electrode surface through Sticky-PF as an interfacial compatibilizer.

As explained in the previous section, the conductivity of SWNTs film was not affected by Sticky-PF coverage. The voltammogram of the electropolymerization of ProDOP on Sticky-PF coated SWNTs film offer further proof that the non-covalent functionalization of carbon nanotube surfaces through pyrene units does not render the SWNTs electrochemically passivated. It is obvious that charge carriers can tunnel through the thin layer of adsorbed Sticky-PF, as shown in Figure 3-18A. Moreover, no polymer delamination was visually observed after subsequent electrodeposition of polymer film onto the Sticky-PF modified SWNTs. These results effectively demonstrate that Sticky-PF as an interfacial compatibilizer effectively enhances the interaction of PProDOP with the SWNT surface.

### **Electrochemistry of PProDOP Film on Sticky-PF coated SWNTs Film**

In order to obtain uniform films of PProDOP on the porous 3D-network structured SWNTs electrodes, the potentiostatic wave electropolymerization method was applied, in contrary to the constant potential electrochemical polymerization method that was used for the deposition of PProDOP on flat gold substrates. This method involves step-wise constant potential application at determined time intervals. The potential stepped between the monomer peak potential of

0.76V vs. Fc/Fc<sup>+</sup> plus 0.05V and a potential of -0.4V vs Fc/Fc<sup>+</sup> where the resulting polymer is in oxidized and neutral state, respectively. The potential stepping was repeated for 10s intervals until the desired amount of material was deposited. The solution was gently stirred during electropolymerization process to preserve the homogeneity of the monomer solution especially in the vicinity of the electrode. This method is somewhat analogous to the cyclic voltammetry deposition method and projected to be the most suitable synthetic method for any porous structured substrates like SWNTs film. Application of the oxidative and reductive (neutralization) potentials alternatively with time intervals would allow the constant potential polymerization and also permit sufficient time for the monomer species to diffuse through the channels of porous network in order to maintain the monomer-electrolyte concentration at equilibrium in the pores of the nanotube film to prevent diffusion limited polymerization to occur. On the other hand, this method allows for the reorganization of the already formed polymers in between the pores once the neutralization potential applied alternatively with the oxidative potential, to obtain smooth homogenous films of PProDOP. Once formed on the electrode, the polymer films were thoroughly soaked and rinsed with ACN and equilibrated with the monomer free electrolyte solution as explained in the previous sections and voltammograms of the switching of polymer films were then obtained.

To determine the extent of capacitance contribution from Sticky-PF which acts as a compatibilizer layer between the nanotubes and PProDOP, the voltammograms of PProDOP on a Sticky-PF coated SWNTs electrode were compared with the CV of Sticky-PF coated SWNTs electrode prior to PProDOP deposition as well as pristine SWNTs. As expected, no distinction was observed between the electrochemical response of pristine and Sticky-PF coated SWNT films, indicating that Sticky-PF did not appreciably perform as a charge storage material. The

capacitances obtained from those films were found to be  $0.09\text{mF/cm}^2$  due to the double layer charging of the surface. In the Figure 3-19, CVs of Sticky-PF coated SWNTs electrodes before and after PProDOP deposition are shown at a scan rate of  $50\text{mV/s}$  between  $-0.5$  and  $+0.5$  V vs  $\text{Fc}/\text{Fc}^+$ . It can be clearly seen that the capacitance contribution of the electrode before PProDOP deposition is negligible.

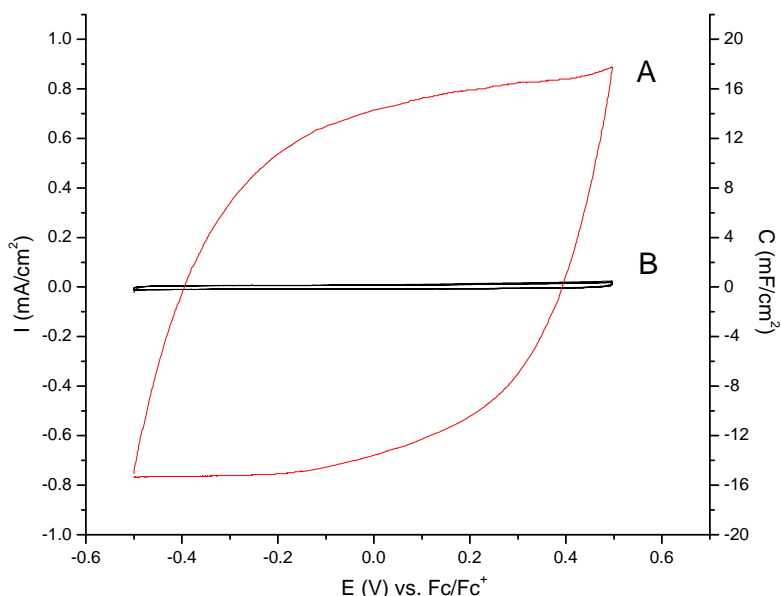


Figure 3-19. Cyclic voltammograms of A) PProDOP on Sticky-PF|SWNTs and B) bare Sticky-PF|SWNTs film in LiBTI/ACN at  $50\text{ mV/s}$ .

As in the case for PProDOP on gold electrode substrates, in order to relate the deposition charge and more importantly the capacitance values with the mass of PProDOP, calibration graphs were prepared for the films prepared on the Sticky-PF coated SWNTs film substrates. After the electrodes with varying amount of PProDOP were prepared, the capacitance values of the films and the mass of the polymer material were measured. The mass of the  $80\text{nm}$  thickness film of SWNTs was determined by using the density of the SWNTs. The mass of the SWNTs were subtracted from the measured mass of the PProDOP deposited substrates in order to accurately obtain the mass of PProDOP. As for PProDOP on gold electrode substrates, a linear relationship between the deposition charge for electropolymerization, shown in Fig3-20A, and

also the capacitances of the resulting films with the mass of the PProDOP, shown in Fig3-20B, were found. Unlike the PProDOP deposition on gold electrodes, or bare SWNTs films, after certain amount of PProDOP was deposited, oligomer formation, which was clearly observed by the coloration of the monomer solution, started to occur during deposition. After this point, the mass of the polymers deposited was difficult to determine accurately. In Fig 3-20 the capacitances as a function of the mass of PProDOP on Sticky-PF coated SWNTs film are shown. A very small intercept at the onset of polymerization originates from the double-layer charging of the Sticky-PF coated SWNTs electrodes. From the slope of the curve, the average specific capacitances of the PProDOP films were calculated as 105F/g. Although, areal capacitances ( $\text{mF}/\text{cm}^2$ ) of PProDOP are found to increase with Sticky-PF|SWNTs electrodes, compared to the Au electrodes (141F/g) the average mass capacitances of PProDOP were decreased by 26% with Sticky-PF|SWNTs. This is probably due to the morphological differences of PProDOP films formed on gold and SWNTs electrodes. As previously mentioned, the capacitance of the polymer strongly depends on the morphology of the polymer. The ion penetration ability through the channels of the porous network of the polymer restricts the capacitance of the material. As will be discussed below, PProDOP forms a more densely structured morphology when deposited on SWNTs than a flat metal surface. Therefore, a smaller percentage of the total mass of the charge storage material contributes to the overall capacitance, resulting decreased mass capacitances.

The cyclic voltammograms of the films with highest deposited amount of PProDOP with the scan rate dependence for the redox switching are shown in Figure 3-21. CVs of the films were taken at different scan rates from 50 to 250 mV/s between  $-0.5$  and  $+0.5\text{V}$  vs  $\text{Fc}/\text{Fc}^+$ . At slower scan rates of 50 and 100mV/s, the typical and previously obtained PProDOP's electrochemical response was observed. As the scan rate was increased, a deviation was

observed, which was attributed to slower ion diffusion through the polymer matrix with respect to the fast potential change. This deviation was expected due to the relatively thick polymer layer. As the scan rates were increased, the ability of ions to penetrate through this thick polymer layer was lowered, and as a result the overall resistivity of the electrode material increased and the maximum capacitance became restricted by electrolyte diffusion kinetics.

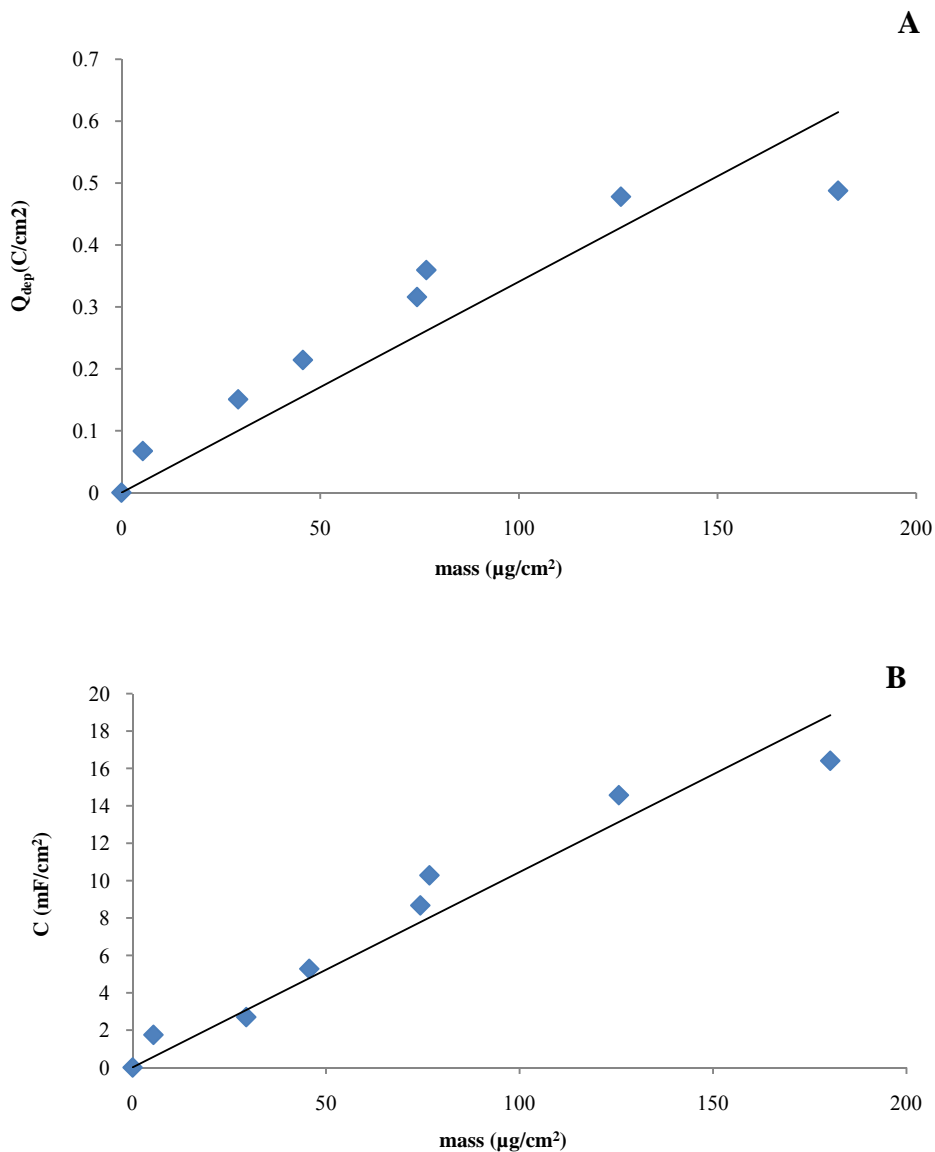


Figure 3-20. Calibration curves; A) Deposition charges of ProDOP and B) capacitances of PProDOP as a function of the mass of PProDOP on Sticky-PF|SWNTs substrates.

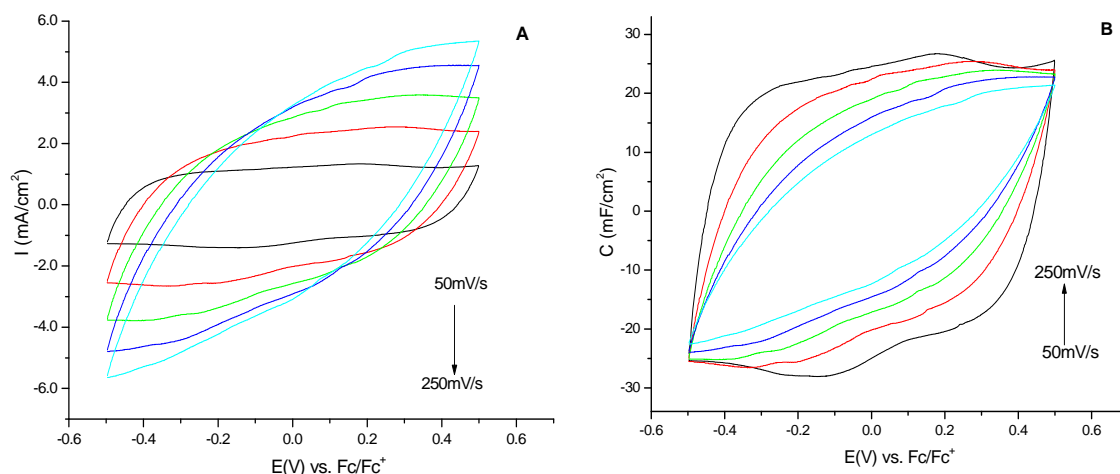


Figure 3-21. A) Cyclic voltammograms and B) capacitances as a function of applied potential of PProDOP films on Sticky-PF/SWNTs in LiBTI/ACN at 50 to 500mV/s with 50mV/s intervals.

The highest capacitance achieved with PProDOP films formed on Sticky-PF coated SWNT electrode reached a stable value of  $25\text{mF/cm}^2$  without degradation or delamination of the film. The cyclic voltammograms at different scan rates from 50 to 250mV/s with the capacitance graphs of this film are shown in Fig 3-21A and b respectively. The corresponding mass of these PProDOP films was calculated as  $239\mu\text{g/cm}^2$  from the calibration curve.

### Surface Analysis of PProDOP Film on Sticky-PF Coated SWNTs Film

The structure of the PProDOP films on Sticky-PF coated SWNTs electrodes were examined using a scanning electron microscope. A  $45^\circ$  tilted angle sample holder was used in order to obtain the highest quality resolution. In order to examine the growth morphology of PProDOP polymerization, films with varying amount of PProDOP were prepared as in the calibration curve. PProDOP was deposited in various amounts using a wave potentiostatic electrodeposition method. Fig 3-22 demonstrates this deposition morphology of PProDOP on Sticky-PF coated SWNTs.

The deposition of the film begins with the formation of an extremely thin uniform layer of PProDOP. This thin layer is a continuous layer of PProDOP directly attached to the nanotubes and fill up the pores of the three dimensional nanotube network. In Fig 3-22A, the noodle-like structure of the nanotube bundles can be easily realized underneath the thin layer of the polymer. Some irregularities formed, as seen in the SEM image of this early stage of film deposition. As the polymerization proceeded, the noodle-like structure of the SWNT film electrode could no longer be discerned since PProDOP layer became thicker. Further polymerization allowed thicker films of PProDOP to be formed. In Fig 3-22C, the SEM image of the cross section of a relatively thick film is shown and the nanotubes bundles that are broken off and sticking out of the polymer layer are clearly visible.

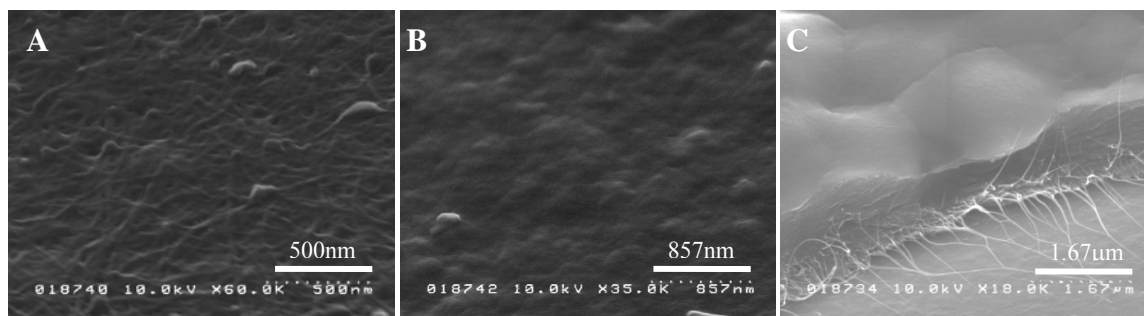


Figure 3-22. Scanning electron micrographs of PProDOP films on Sticky-PF|SWNTs substrates; A) at the start of the deposition, B) during the progress of the deposition and C) after formation of a thick film at varied magnification.

The films demonstrate more compact and dense morphologies when deposited onto the Sticky-PF coated SWNTs compared to deposition on gold. These structures show consistency with the calculated specific capacitance results. The polymers probably have a high affinity for the Sticky-PF coated porous nanotube substrate and interact well with (or diffuse into) the substrate, as shown in the Fig 3-22C. As predicted, the three dimensional network of SWNTs serves as a structural support for PProDOP layer, much like a plant anchors itself via roots in the soil. This change allowed the delamination of the polymer from the electrode surface to be

eliminated. Moreover, the conductivity of the SWNTs dispersed throughout the PProDOP structure must increase the electrical conductivity of the polymer film, so the charge injection into the charge storage medium (PProDOP) is greatly enhanced by the accessible surface areas of the SWNTs film, compared to that of flat surface electrodes.

### **Type I Supercapacitor Devices with Sticky-PF Coated SWNT Substrates**

The cyclic voltammograms and capacitance graphs of supercapacitors prepared using LiBTI gel electrolyte with PProDOP deposited on Sticky-PF coated SWNTs film, at the sweep rates from 50 to 250mV/s with 50 mV increments, are shown in Fig 3-23A&B respectively. As in supercapacitors with gold substrates, these supercapacitors also demonstrate shapes which are very close to the ideal parallelogram plot of Type I devices. Although a slight deviation in the parallelogram shape occurs as the scan rates increases, the device still shows an effective switching curve at higher scan rate of 250mV/s.

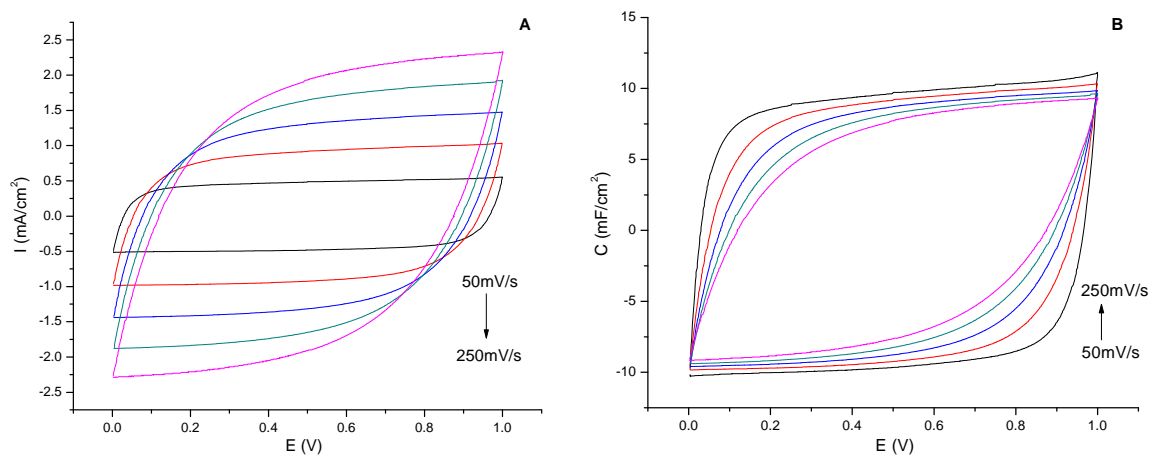


Figure 3-23. A) Cyclic voltammograms and B) capacitances as a function of applied potential of Type I PProDOP supercapacitor with Sticky-PF|SWNTs substrates using LiBTI gel electrolyte at 50 to 250mV/s with 50mV/s intervals.

The capacitance values achieved with PProDOP on Sticky-PF coated SWNTs were found to be 9.7mF/cm<sup>2</sup>. As stated above, the corresponding mass of PProDOP of this film (25mF/cm<sup>2</sup>) was calculated as 239μg/cm<sup>2</sup> from the calibration curve. So the specific capacitance of the device

was calculated by dividing the measured capacitance ( $9.7\text{mF}/\text{cm}^2$ ) to the mass of two electrodes ( $2 \times 239\mu\text{g}/\text{cm}^2$ ) and found as  $20\text{F}/\text{g}$ .

Since the capacitances of the device is expected to be the half of the capacitance of the film ( $25\text{mF}/\text{cm}^2$ ), as explained in the section 3.6. The capacitance of the device is  $9.7\text{mF}/\text{cm}^2$  and 77% of the expected value of  $12.5\text{mF}/\text{cm}^2$ . This result demonstrates that the difference between the measured and the calculated capacitance of the device can be attributed to a substantial value of equivalent series resistance, especially switching from solution-based measurements for films to gel electrolyte systems in case of devices.

The energy and power density of the device, shown in Fig 3-23, were calculated as  $1.3\text{Wh}/\text{kg}$  and  $466\text{W}/\text{kg}$ , respectively. Table 3-1 summarizes the areal and specific capacitances of PProDOP films, along with the energy and power densities determined for PProDOP Type I supercapacitors on gold and Sticky-PF coated SWNTs substrates discussed in this chapter in comparison to each other.

Table 3-1. Capacitances, energy and power densities of PProDOP films and devices.

<i>Substrate</i>	<i>Film</i>		<i>Device</i>			
	<i>C(mF/cm<sup>2</sup>)</i>	<i>C (mF/g)</i>	<i>C(mF/cm<sup>2</sup>)</i>	<i>C (mF/g)</i>	<i>E (Wh/kg)</i>	<i>P(W/kg)</i>
<i>Au Kapton</i>	8.1	141	3.2	30	2.6	584
<i>Sticky-PF SWNTs</i>	25	105	9.7	20	1.3	466

### **Stability of Type I Supercapacitors with Sticky-PF coated SWNTs Substrate**

The cyclic stability of the Sticky-PF|SWNT based devices were examined by continuous CV switching for over 32700 non-stop cycles at a scan rate of  $100\text{mV}/\text{s}$ , as shown in Fig 3-24. The corresponding voltammograms of films were shown in Fig 3-21, which are the highest capacitance values obtained with PProDOP on the Sticky-PF|SWNTs film substrates.

Voltammograms of the device switching were recorded in every 100 switches up to a total of 32767 switches. The average capacitance for each voltammogram was calculated and plotted as a

function of number of cycles. As mentioned in the previous sections, conducting polymers require a preconditioning period in order to obtain reproducible CVs, permitting complete permeation of the electrolyte into the polymer. The fast decrease of capacitance ( $\sim 1\text{mF}$ ) seen in the first several hundred cycles are due to this “break-in” period. There after the capacitance of the device continues to decrease slowly for the duration of the experiment. In contrast to gold devices, the Sticky-PF|SWNT devices show a steady loss of capacitance to about 35% of the original value.

As mentioned in the previous sections, swelling and shrinking of the polymer occur during doping and undoping processes. This phenomenon surmised to cause the polymer to peel off from the gold substrate, especially as the adhesion gets weaker with thicker polymer films. However using the porous structured SWNT film substrates prevented the poor adhesion issue particularly with thicker polymer layers. Nevertheless, the intrinsic swelling and construction had a negative effect on the overall stability, therefore performance constraint occurred especially with increased film thicknesses. Since each component of a device system from electrodes to separator paper contributes to the overall stability, further optimization is necessary to increase the stability of these Sticky-PF|SWNT based devices. These devices were prepared on a bench top at ambient conditions. The aim of this study was to prepare an electrode substrate that would allow higher amounts of PProDOP material to be deposited for switching. However, while the switching of the devices was not as stable as gold devices, the capacitance values achieved with Sticky-PF|SWNT based devices were initially almost four times of the capacitance of gold devices, and remained as high as three times even after 15000 cycles switching. Sticky-PF|SWNT based devices maintain a greater capacitance than the gold device for overall 32000 cycles, which is very encouraging.

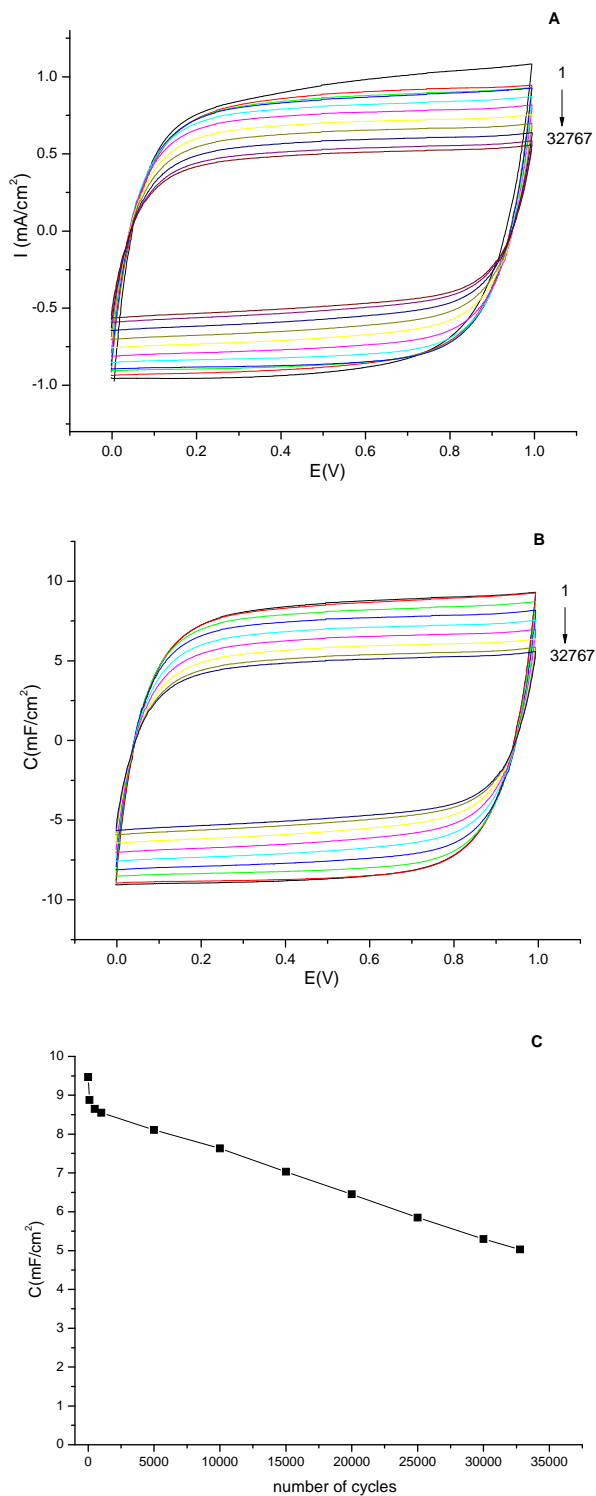


Figure 3-24. Stability of Type I PProDOP supercapacitors with Sticky-PF|SWNTs substrates using LiBTI gel electrolyte by non-stop cycling at 100mV/s scan rate; A) cyclic voltammograms, B) capacitances as a function of applied potential and C) capacitances as a function of number of switching cycles (1<sup>st</sup>, 100<sup>th</sup>, 500<sup>th</sup>, 1000<sup>th</sup> and every 5000<sup>th</sup> cycle).

## Conclusions and Perspective

In conclusion, this chapter presents the utilization of PProDOP as the charge storage material in Type I supercapacitors. While the ultimate goal of this chapter to demonstrate PProDOP as the charge storage material, different electrode designs have been attained and many key concepts and methods were also demonstrated and established.

The supercapacitor devices were constructed using two different current collector substrates: Kapton-Au sheets and SWNT films. In the latter project, the goal was to utilize the charge storage material on a porous structured substrate to realize the penetration of the material through it, thus to lead more loading of PProDOP per unit area. To the best of our knowledge, this is the first presentation of the use of SWNTs for such a purpose. Although a delamination problem was occurred between PProDOP and SWNTs layers, in order to overcome this problem, a non-covalent modification of the surface of carbon nanotubes have been conducted. On this purpose, a new polymer; “Sticky-PF” was synthesized. It has been observed that PProDOP electrodes containing porous substrates can provide a significant areal capacitance improvement over conventional non-porous flat metalized substrates. In summary, the non-covalently modified SWNT films with Sticky-PF are presented as a novel type of supercapacitor electrode substrate in this chapter. Any supercapacitor utilizing varying charge storage materials can benefit from this method.

All PProDOP films were deposited by electrochemical polymerization techniques in the presence of different supporting electrolytes. The electrochemical and morphological properties of the resulting films were investigated by using cyclic voltammetry, galvanostatic charging-discharging methods and also SEM and AFM techniques. PProDOP exhibit homogeneous morphology with porosities up to varying levels in the presence of different supporting electrolytes and current collector substrates. The results show that PProDOP exhibits almost

ideal rectangular CV behavior of a supercapacitor material with LiBTI as the supporting electrolyte. Moving from electrode substrates with flat metalized surfaces to the ones with porous structures were led to more than 3 fold increase in capacitances of PProDOP per unit area. On the other hand the specific capacitances (per total active material) show a 26% decrease.

Correspondingly the specific capacitance values of the supercapacitors were found to be diminished with Sticky-PF/SWNTs substrates compared to Kapton-Au substrates, however, the areal capacitances were calculated as  $3.2 \text{ mF/cm}^2$  and  $9.7 \text{ mF/cm}^2$  for the devices with Kapton-Au and Sticky-PF/SWNTs substrates, respectively. The devices with both of the substrates, but especially the ones based on Kapton-Au, showed excellent stability during long cycles with a moderate loss of charge.

Future directions for this work would include optimization of the device performances for varying intentions; this would entail determining the optimum amount of the polymer material (or thickness) for the highest capacitance performances. In further studies, SWNT films with increased porosity or a SWNT film template with particular order (perpendicularly aligned bundles) can be utilized in conducting polymer based supercapacitors in order to increase the polymer loading per unit area. Moreover, utilization of solution processable conjugated polymers would be a major advantage for construction of large area supercapacitors.

CHAPTER 4  
TYPE IV SUPERCAPACITORS: DONOR-ACCEPTOR-DONOR SYSTEMS

**Introduction**

Pseudocapacitance arises from an electrochemical Faradaic charge transfer processes, where the extent of the reaction  $Q$  is a function of the cell potential. During discharging of an ideal battery cell exhibiting a Nernstian cell potential, the progressively increasing charge is being added at a relatively constant voltage that remains ideally constant until all the reactant materials have been electrochemically consumed. Unlike this Nernstian behavior in batteries, in pseudocapacitance processes, the extent of Faradaically admitted charge depends almost linearly, on the applied voltage. In other words, the potential at which the charge is being passed is a continuous function of the charge accumulated. Consequently, a capacitive phenomenon occurs with the arising derivative of  $dQ/dV$  having the properties of a capacitance.

As introduced in Chapter I, the energy stored electrochemically in a battery is given as  $QV$ , where  $V$  is the voltage of the cell and  $Q$  is the cell charge capacity; the electrical charge transferred to the load during the chemical reaction. On the contrary, the energy of a capacitor charged to a potential difference of  $V$ , scales with the square of the cell voltage and can be calculated due to Eq 1-2;

$$E = \frac{1}{2} CV^2 = \frac{1}{2} QV$$

Hence, the energy stored in an electrochemical capacitor is half of the value for the equivalent charge stored in a battery<sup>14</sup> Therefore, the key to achieving higher energy densities in a electrochemical supercapacitor is to expand the cell voltage.

In conducting polymers, the redox pseudocapacitance arises from the doping and undoping processes of the material. As mentioned in the previous chapters, the versatility of the conjugated polymers enables different redox supercapacitor configurations. Among the different polymer

supercapacitor configurations proposed to date, the Type III and IV (n/p-type) devices are the most promising configurations in terms of having a high operating voltage for delivering all the doping charge during discharge at high potentials. The operating voltage of the cell can be increased up to 3V in these kinds of devices. Hence, the highest energy densities are possible with these designs. Besides providing the broadest cell operating voltages, Type III&IV supercapacitors can deliver all the doping charge during discharge at high potentials; consequently, high power densities can be demonstrated.

The Type III and IV supercapacitors are based on conducting polymers that can be p- and n- dopable. Devices utilize the n-dopable polymer as the negative electrode and the p-dopable polymer as the positive electrode. Type III supercapacitors uses the same polymer on both the positive and the negative electrodes while Type IV utilizes two different polymers. The anode p-dopable polymer is in the fully oxidized state and the cathode n-dopable polymer is in the fully reduced form when the device is charged. Both polymers neutralize with the discharging of the supercapacitor. By this means, the total charge capacity of both p- and n-dopable polymers contribute to the overall capacitance of the device.

The p-&n- type conducting polymer based supercapacitors are the most favorable configurations in terms of energy and power densities, but the difficulty of obtaining stable n-doping polymers is the largest obstacle for the development of these supercapacitors for real-world applications. While there have been some n-dopable polymers synthesized, most of their coulombic efficiency is low upon repetitive cycling in the reduced state. The bulk of conjugated polymer systems possess positive charge carriers (hole transport) exhibiting p-type doping. To obtain a truly n-type doped system that exhibit stable coulombic efficiency is still a challenge in the field of conducting polymers since the environmental stabilities of n-type dopable systems

are poor due to the high reactivity of the radical anion charge carriers to oxygen and water. The concept of “band-gap engineering” method allows one to modulate the electronic properties of a polymer by controlling both the electron donating and electron accepting abilities, thus the valence and conduction band levels of the polymer. Conjugated polymer systems having stable oxidation and reduction redox states with lowered band gaps are possible by incorporating donor-acceptor (D-A) units into a single polymer backbone. The D-A approach has been used in various combinations and has resulted in some of the most successful n-dopable conjugated systems to date.<sup>158-165</sup>

Several D-A type polymers were previously investigated in the Reynolds’ Group.<sup>158, 164, 166, 167</sup> Recently a family of D-A-D monomers based on alternating alkylendioxythiophene donors and nitrogen based heterocycle acceptors, whose structures are shown in Fig 4-1, were synthesized by Tim Steckler in the Reynolds’ Group.<sup>121</sup>

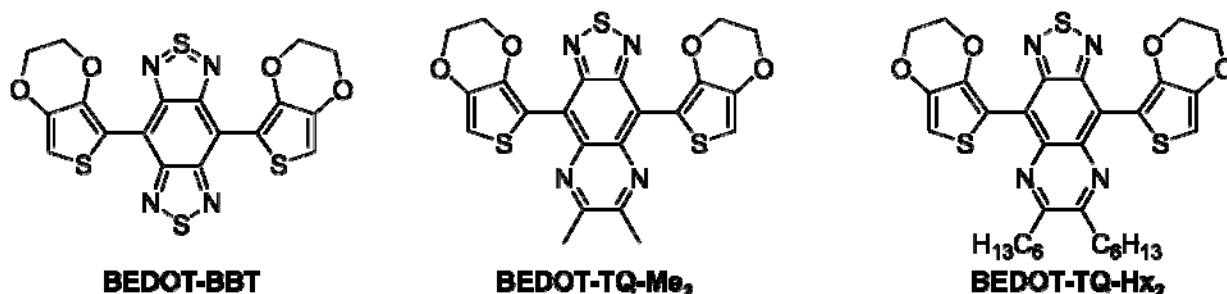


Figure 4-1. Structures of donor-acceptor-donor EDOT-benzobisthiadiazole and thiadiazole-quinoxaline monomers: BEDOT-BBT, BEDOT-TQ-Me<sub>2</sub>, BEDOT-TQ-Hx<sub>2</sub>.

The three D-A-D monomers based on alternating ethylenedioxythiophene (EDOT) as a donor along with benzobisthiadiazole and thiadiazole-quinoxaline acceptors will be referred to as follows throughout this chapter: BEDOT-BBT, BEDOT-TQ-Me<sub>2</sub> and BEDOT-TQ-Hx<sub>2</sub>. The Type IV supercapacitors utilizing PProDOP and this family of D-A-D systems are discussed in this chapter. In the supercapacitor devices, PProDOP were used as the p-dopable polymer on the

positive electrode and the D-A-D systems (Fig 4-1) were used as the n-dopable polymers on the negative electrodes.

### **Cyclic Voltammetric Deposition of DAD Systems**

Electrochemical polymerization of the monomers shown in Fig 4-1 were carried out via repeated scan cyclic voltammetry (CV) from a 5mM monomer, 0.1M electrolyte solution of TBAP or LiBTI in acetonitrile or propylene carbonate onto platinum button, gold button and Au/Kapton electrodes, respectively. Several drops of methylene chloride were added to achieve complete dissolution of the monomer due to their limited solubility in acetonitrile and propylene carbonate. All electrochemical experiments were performed in a glovebox filled with argon having both H<sub>2</sub>O and O<sub>2</sub> concentrations less than 1 ppm.

The best quality homogeneous films with good electrochemical response of these polymers were found as the ones synthesized through CV on Au button electrodes from TBAP/ACN solution. In Fig 4-2A, the first 10 complete scans of CV deposition of BEDOT-BBT at a scan rate of 50mV/s in TBAP/ACN is shown. Very similar deposition voltammograms of BEDOT-BBT were obtained for different electrolyte solution systems, but with very small current densities in LiBTI systems. As shown in the voltammograms in Fig 4-2A, BEDOT-BBT gives a peak oxidation potential at 0.5V vs. Fc/Fc<sup>+</sup>. Upon continued cycling an increase in current densities of the monomer oxidation peaks is observed and the formation of the as made polymer film on the gold electrode is easily evidenced by the increase in current densities of the peaks appearing between 0 and +0.3 V vs. Fc/Fc<sup>+</sup>, as indicated by the arrows.

In addition to gold button electrodes, Au/Kapton sheets were also used for the film deposition. The first 30 complete scans of CV deposition of BEDOT-BBT at a scan rate of 50mV/s in TBAP/PC on Au/Kapton (1cm<sup>2</sup>) sheets is shown in Fig 4-2B. Compared to the voltammogram of BEDOT-BBT deposition on Au button electrode that were shown in Fig 4-2A,

the results in Fig 4-2B on a larger electrode surface of Au/Kapton sheets are quite similar to each other in shape. However, in the case of Au/Kapton electrodes, the electrochemical polymerization leads to dramatically smaller current densities; almost an order of magnitude less. Hence, the efficiency of the film formation was low as seen in Fig 4-2B. This is probably due to the limited solubility of the monomer in propylene carbonate since the more soluble monomers can polymerize more easily, forming homogeneous films that provide better electrochemical results. For that reason, the experiments were conducted on Au button electrodes for the rest of the chapter.

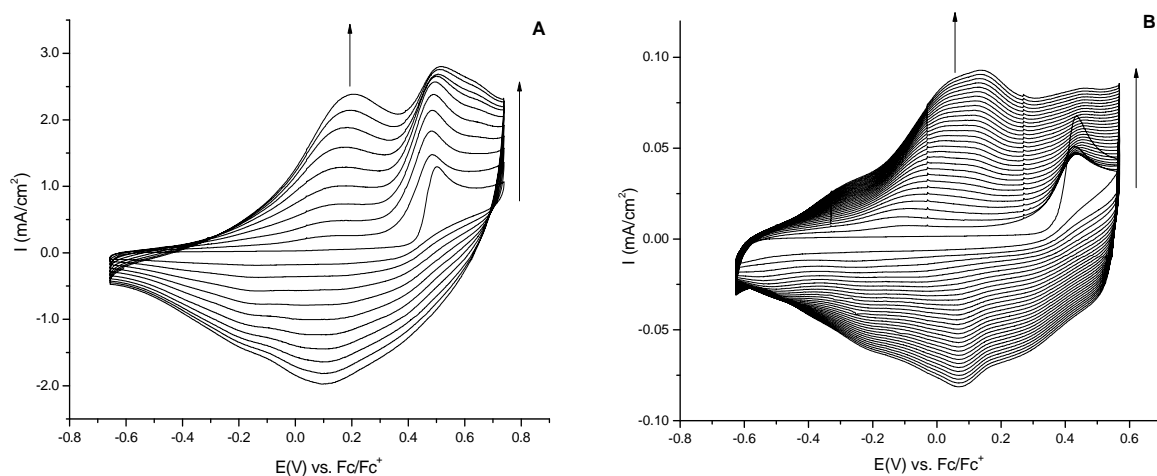


Figure 4-2. Electrochemical polymerization (first 10 cycles) of BEDOT-BBT by potential scanning on A) Au button ( $0.02\text{cm}^2$ ) in TBAP/ACN and on B) Au/Kapton ( $1\text{cm}^2$ ) in TBAP/PC at  $50\text{ mV/s}$ . (Several drops of methylene chloride were added to assist in complete dissolution of the monomers.)

The CV electropolymerization of BEDOT-TQ-Me<sub>2</sub> and BEDOT-TQ-Hx<sub>2</sub> were carried out using the same electrolyte solution; TBAP/ACN on Au button electrodes. The voltammograms are shown in Fig 4-3A and B respectively. Both of these monomers were polymerized forming electrochemical responses slightly different than the deposition of BEDOT-BBT but very similar to each other. As shown in Fig 4-3A and B, BEDOT-TQ-Me<sub>2</sub> oxidizes at  $0.57\text{V vs Fc/Fc}^+$  and BEDOT-TQ-Hx<sub>2</sub> oxidizes at  $0.67\text{V vs Fc/Fc}^+$ , respectively. The oxidation potential of BEDOT-

TQ- Hx<sub>2</sub> is found at a slightly higher potential than the E<sub>p,m</sub> of either BEDOT-BBT and BEDOT-TQ- Me<sub>2</sub>. Moreover, the second and third scans lead to slightly smaller current density of the monomer oxidation peak, which was previously seen for the electrochemical polymerization of similar types of monomer systems.<sup>129, 168</sup> The increase in the current densities of the peaks appearing between 0V and +0.5 V vs Fc/Fc<sup>+</sup> with the progression of cycling in both cases is due to the redox activity of the polymers being formed on the electrode surfaces. As a result of creating a chemically modified working electrode and forming dimers, the monomers' oxidation peaks become broader and negatively shift to 0.1V lower potential upon continued cycling. The overall current densities for the same number of cycles are higher in the case of BEDOT-TQ-Hx<sub>2</sub> than those of BEDOT-TQ-Me<sub>2</sub>. The results indicate that the electropolymerization and switching of BEDOT-TQ-Hx<sub>2</sub> is more efficient than BEDOT-TQ- Me<sub>2</sub>. One possible reason for this is the slightly more open morphology caused by bulkier hexyl pendant groups.

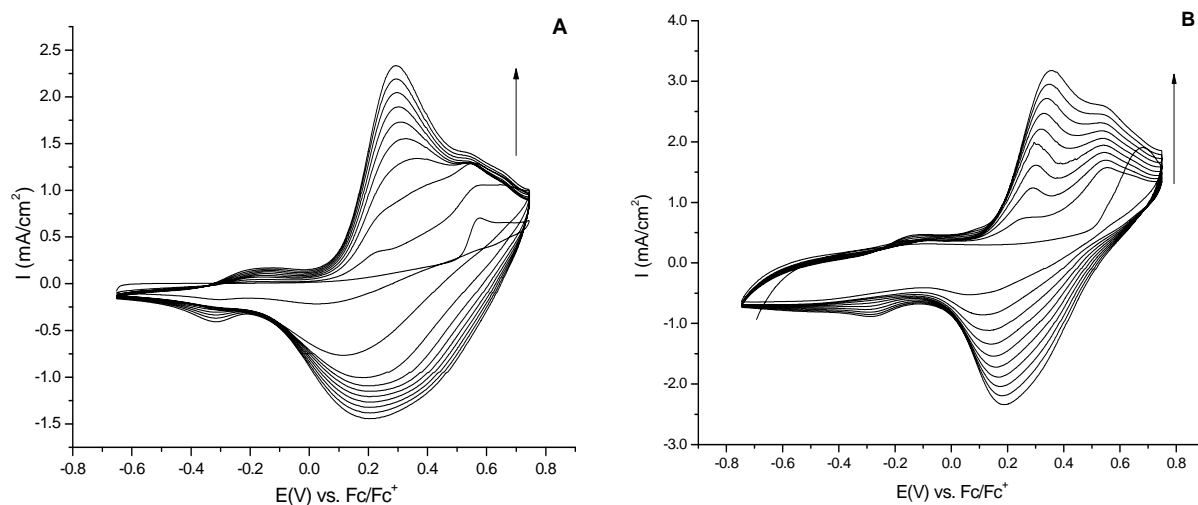


Figure 4-3. Electrochemical polymerization (first 10 cycles) of A) BEDOT-TQ-Me<sub>2</sub> and B) BEDOT-TQ-Hx<sub>2</sub> by potential scanning on Au button (0.02cm<sup>2</sup>) in TBAP/ACN at 50 mV/s. (Several drops of methylene chloride were added to assist in complete dissolution of the monomers in acetonitrile.)

Cyclic voltammograms of all of the three DAD monomers exhibit the irreversible monomer oxidation peak with the absence of a reductive wave which is indicative of radical-

radical coupling showing ease of formation of polymeric materials. The relatively low oxidation potentials of all three monomers can be attributed to the terminal 3,4-alkylenedioxythiophene (EDOT) units of the monomers, which are electron rich in character that allow easily accessible oxidation potentials for electrochemical polymerization.

### **Electrochemistry of P(DAD) Films**

The electrochemically synthesized polymer films from all three monomers were examined for their redox processes in TBAP/ACN, after being washed with copious amounts of acetonitrile to remove any residual monomers. These polymer films possess unique properties when reductively (or n-type) doped.

Introducing strong acceptor units of heterocycles containing nitrogens in between the terminal EDOTs within the polymer repeat unit lowers the LUMO level of the molecule since the nitrogen is more electronegative compared to the carbon.<sup>121, 169</sup> Subsequently, the reduction of the polymer occurs more easily. The benzobis(thiadiazole) and thiadiazole-quinoxaline units are strong acceptors. This helps to create relatively positive reduction potentials for the polymers, and enhance the reductive stability upon repetitive cycling due to the easy access to their reduced states.

The donor-acceptor character of these monomers and polymers allows stabilizing separated charges. Anion radical structures demonstrating the hypothetical reduction of PBEDOT-BBT are shown in Fig 4-4, as the representative of all three P(DAD) systems since PBEDOT-TQ-Me<sub>2</sub> and PBEDOT-TQ-Hx<sub>2</sub> can be envisioned to behave in a similar way. Introducing an electron to the polymer backbone forms a radical anion, in which the electron density is stabilized on the nitrogen on the thiadiazole ring of the acceptor unit as shown in the scheme. The first electron would be stabilized in the same way upon reduction of PBEDOT-TQ-Me<sub>2</sub> and PBEDOT-TQ-Hx<sub>2</sub> since the thiadiazole is a stronger acceptor unit than the quinoxaline unit. The next

introduced electron upon the second reduction of PBEDOT-BBT could occur in different ways. Only one of the hypothetical structures of the second reduction is shown in the Fig 4-4, where the electron density is stabilized on the other thiadiazole ring, indicating the ability of this acceptor unit to accommodate more than one negative charge density. Moreover, the resonance states of this structure would exhibit varying delocalization points for the two electron densities, distributed between the two thiadiazole rings. In the same way, the second electron density upon the second reduction of PBEDOT-TQ-Me<sub>2</sub> and PBEDOT-TQ-Hx<sub>2</sub> could be delocalized either on the thiadiazole or quinoxaline rings. Cyclic voltammograms of all three compounds showed two reductive doping peaks, which is consistent with the proposed structures in Fig 4-4.

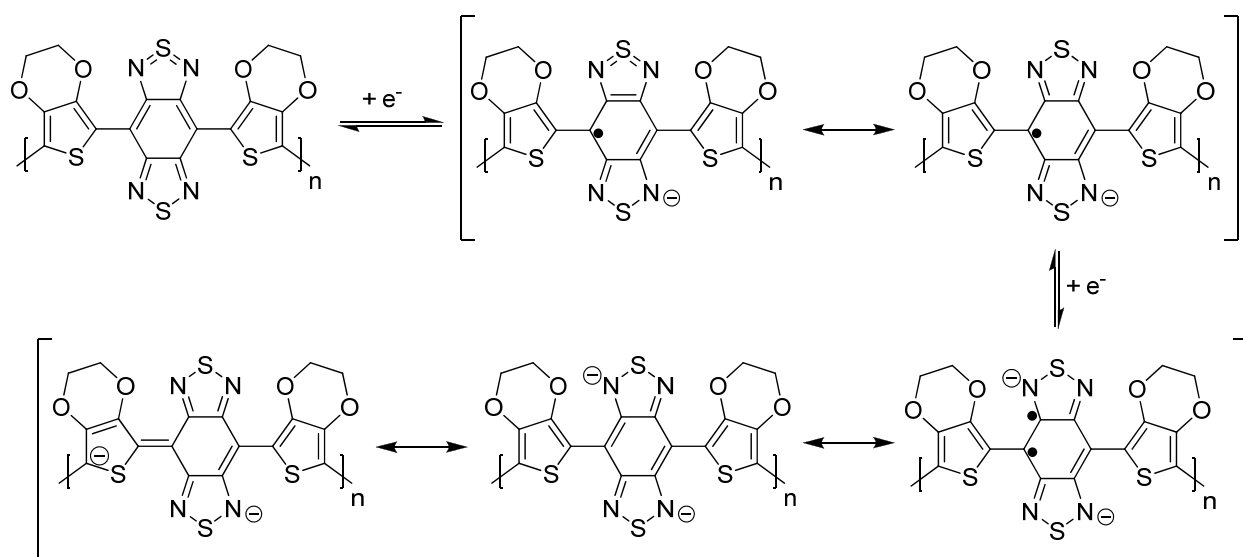


Figure 4-4. Anion radical structures demonstrating the hypothetical mechanism of the reductive doping (first and second reductions) of PBEDOT-BBT with the proposed resonance structures of the reduced forms of the polymer.

All P(DAD) systems could possess dual p-type and n-type doping with in a single polymer. In order to examine the n-type doping properties, only reductive doping experiments were performed separately from oxidative doping of the same polymer. Experiments conducted by repeatedly cycling between oxidized (p-doped) and reduced (n-doped) states can often lead to the

formation of peaks that may be misinterpreted as redox doping peaks which result from trapped charge carriers. Accordingly, the polymers were switched by repetitive potential scanning from neutral to reduced state for ten times to condition (break-in) the films until a reproducible CVs were obtained. The reductive cyclic voltammetry behaviors of the all three polymers, as a function of the scan rate between 50 and 500mV/s with 50mV increments are shown in Fig 4-5. As can be seen in the figure, the reproducible cyclic voltammetric behavior upon reduction of each polymer is similar to each other. Two reduction processes occur for each polymer due to the strong acceptor unit that allows for the insertion of two electrons per polymer repeat unit. The n-type doping electrochemistry shows sharp and discernible peaks.

In Fig 4-5A, PBEDOT-BBT exhibits two redox processes with  $E_{1/2}$  values centered at -0.98 and -1.78 V vs. Fc/Fc<sup>+</sup>. This demonstrates the high electron accepting ability of the polymer having two thiadiazole rings on the acceptor that it can stabilize two negative charges. Both of the reductive doping peaks exhibit comparable current densities, and the anodic to the cathodic peak charge ratios exhibits values close to the ideal ratio of 1, even at a scan rate as high as 500mV/s. This demonstrates the quasi-reversibility of both the first and second n-doping processes of PBEDOT-BBT. Moreover, the peak current densities in both peaks increase linearly as a function of scan rate up to 500mV/s, indicating that the electroactive sites are surface bound to the electrode and that the reduction processes are not diffusion limited.

PBEDOT-TQ-Me<sub>2</sub> and PBEDOT-TQ-Hx<sub>2</sub> systems contain thiadiazole-quinoxaline units as acceptor different than the benzobis(thiadiazole) unit in PBEDOT-BBT. Since quinoxaline based unit is a weaker acceptor than thiadiazole based unit, it is expected to observe noticeable changes in the voltammograms of these polymers in moving from the stronger to the weaker acceptor.

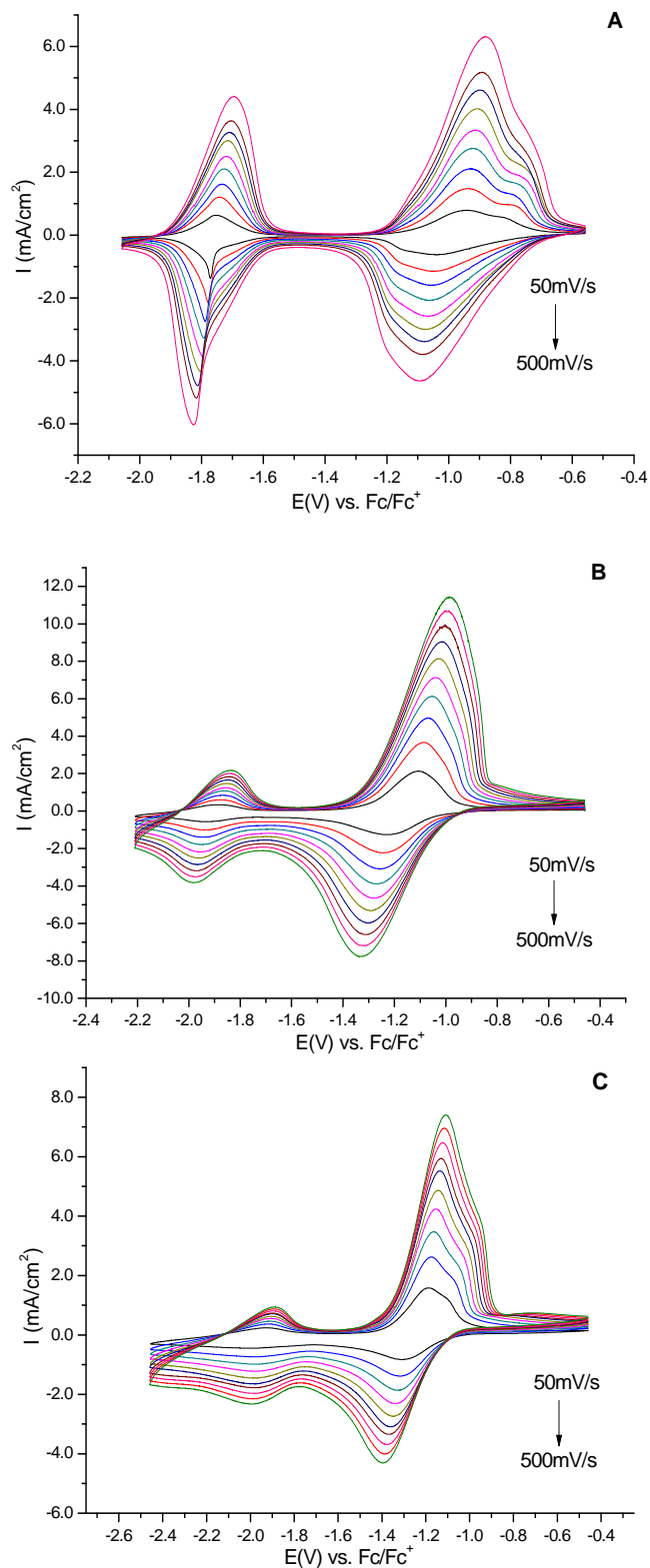


Figure 4-5. Reductive cyclic voltammograms of A) PBEDOT-BBT, B) PBEDOT-TQ-Me<sub>2</sub> and C) PBEDOT-TQ-Hx<sub>2</sub> at 50-500 mV/s on Au button electrode (0.02cm<sup>2</sup>) in 0.1 M TBAP/ACN solution.

In Fig 4-5B&C, PBEDOT-TQ-Me<sub>2</sub> and PBEDOT-TQ-Hx<sub>2</sub> exhibit an E<sub>1/2</sub> value at -1.2 V and -1.25 V for the first reduction, and an E<sub>1/2</sub> value at -1.9 V and -1.95V for the second reduction, respectively. The first reduction peaks of polymers are quite stable and quasi-reversible with adequate charge compensation of the anodic to the cathodic peak. On the other hand, the second reduction does not exhibit a similar behavior. The current densities of the first reduction peaks of these polymers are on the same order of magnitude with the first reduction of PBEDOT-BBT. However, the current densities observed for the second reduction processes of both PBEDOT-TQ-Me<sub>2</sub> and PBEDOT-TQ-Hx<sub>2</sub> are about 1/5 of the first peaks. These results confirm the strong ability of the thiadiazole ring to delocalize electron densities since the high coulombic efficiency of the second reduction of PBEDOT-BBT, compared to that for PBEDOT-TQ-Me<sub>2</sub> or PBEDOT-TQ-Hx<sub>2</sub> is evident. Most likely the second reduction of PBEDOT-TQ-Me<sub>2</sub> and PBEDOT-TQ-Hx<sub>2</sub> is stabilized on the quinoxaline ring, which is a weaker acceptor. Furthermore, the peak current densities of the first reductive doping peaks for both polymers increase linearly up to 500mV/s scan rate. Conversely, the current densities for the second peaks do not show a linear dependence on the scan rate. Although both the anodic and cathodic peak currents of the second reductive doping peaks increase with the increasing scan rate, the ratio of them to each other do not exhibit a stable number with the increasing scan rate. This illustrates the relatively low reversibility of the second reductive doping processes of these polymers.

Furthermore, the peak to peak separation in both the first and the second reductions of PBEDOT-TQ-Me<sub>2</sub> and PBEDOT-TQ-Hx<sub>2</sub> is much larger than in PBEDOT-BBT. This result is indicative of the structural differences in the morphologies of these polymers. Incorporating different (weaker) acceptor units in between EDOT units on the polymer backbone and also coupling the alkyl pendant groups on the polymer backbones may result in a more ordered

configuration of the polymer chains resulting in a more compact film, and making it harder for the supporting electrolyte to move in and out of the film.

Although the relative shape of the electrochemical responses of PBEDOT-TQ-Me<sub>2</sub> and PBEDOT-TQ-Hx<sub>2</sub> upon reduction is very similar; the difference of 0.05V between the E<sub>1/2</sub> values of the first reductions between two polymers exactly matches the difference between the E<sub>1/2</sub> values of the second reductions of these two polymers. These slightly different reduction potentials are likely due to the structural differences in the morphology of these polymers caused by the different methyl and hexyl pendant groups. Conversely, the more positive potentials observed for both first and second reductions of PBEDOT-BBT compared to PBEDOT-TQ-Me<sub>2</sub> and PBEDOT-TQ-Hx<sub>2</sub> is likely a consequence of the stronger benzobisthiadiazole acceptor lowering the valance conduction band level of the DAD polymer system.

### **Capacitances of P(DAD) Films**

In order to determine the achievable maximum capacitance from these polymers, the fresh films containing varying amounts of polymers were synthesized from the exact same electrochemical systems while varying the number of deposition cycles. Electropolymerizations were terminated once a certain amount of redox cycles had been reached. In this manner, the mass of the polymers is conveniently been controlled. Then the capacitance values obtained for these films containing varying masses of polymers were determined for all three of the DAD systems. The cyclic voltammograms at a scan rate of 50mV/s, and the capacitances (mF/cm<sup>2</sup>) as a function of applied potentials, are shown in Figs 4-6, 4-7, 4-8 A&B, respectively for the varying amount of P(DAD) systems. The charge examined by integrating the voltammograms of anodic and cathodic scans over the potential range during reductive switching of the polymers are also shown in Figs 4-6C, 4-7C, 4-8C as a function of time.

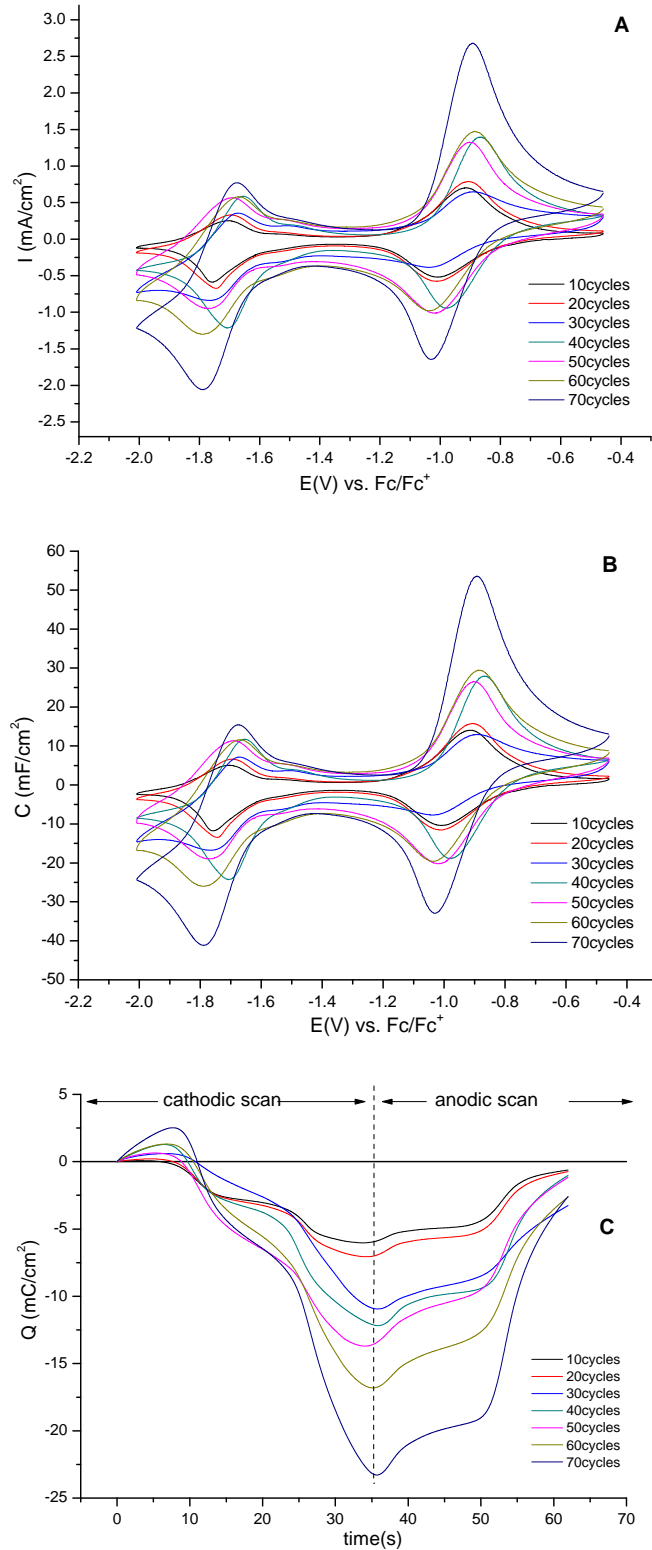


Figure 4-6. A) Cyclic voltammograms, B) capacitances as a function of applied potential and C) charge densities as a function of time of varying amounts of PBEDOT-BBT (deposition cycles) at 50mV/s.

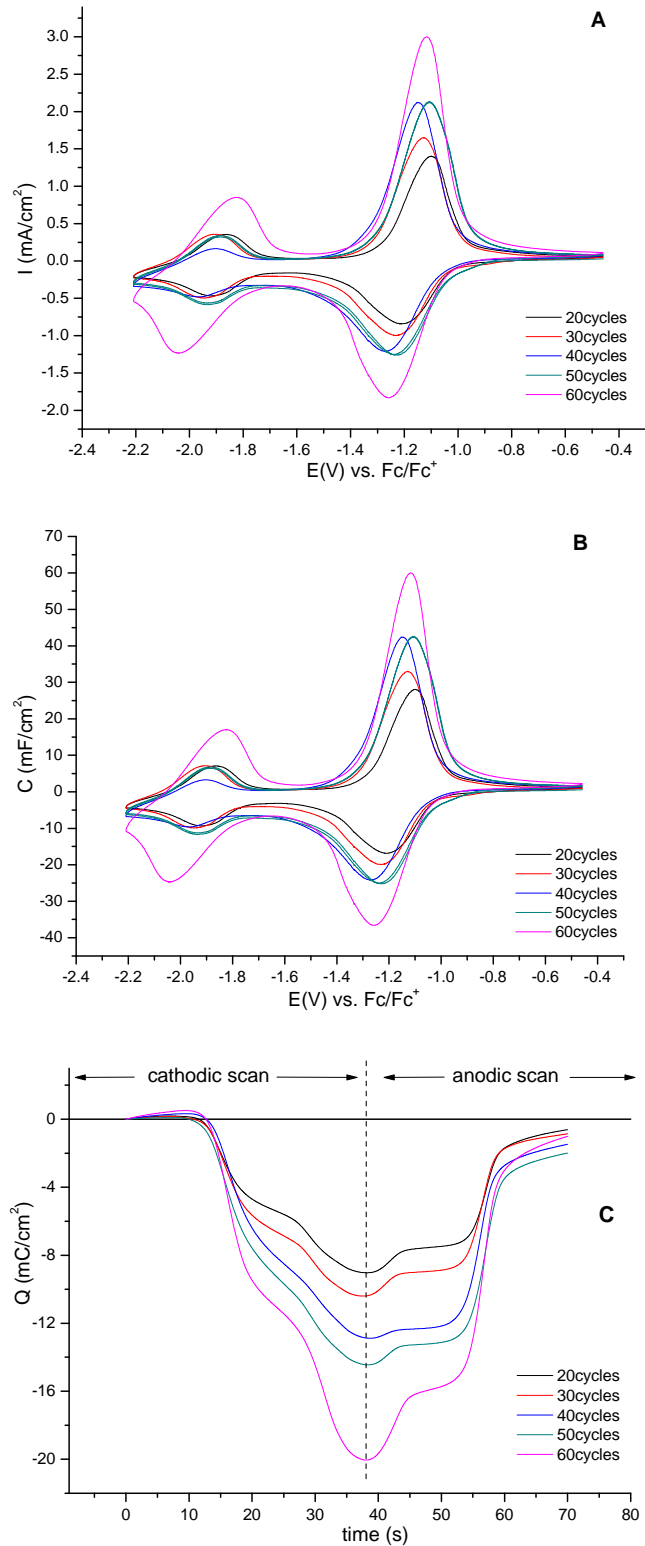


Figure 4-7. A) Cyclic voltammograms, B) capacitances as a function of applied potential and C) charge densities as a function of time of varying amounts of PBEDOT-TQ-Me<sub>2</sub> (deposition cycles) at 50mV/s.

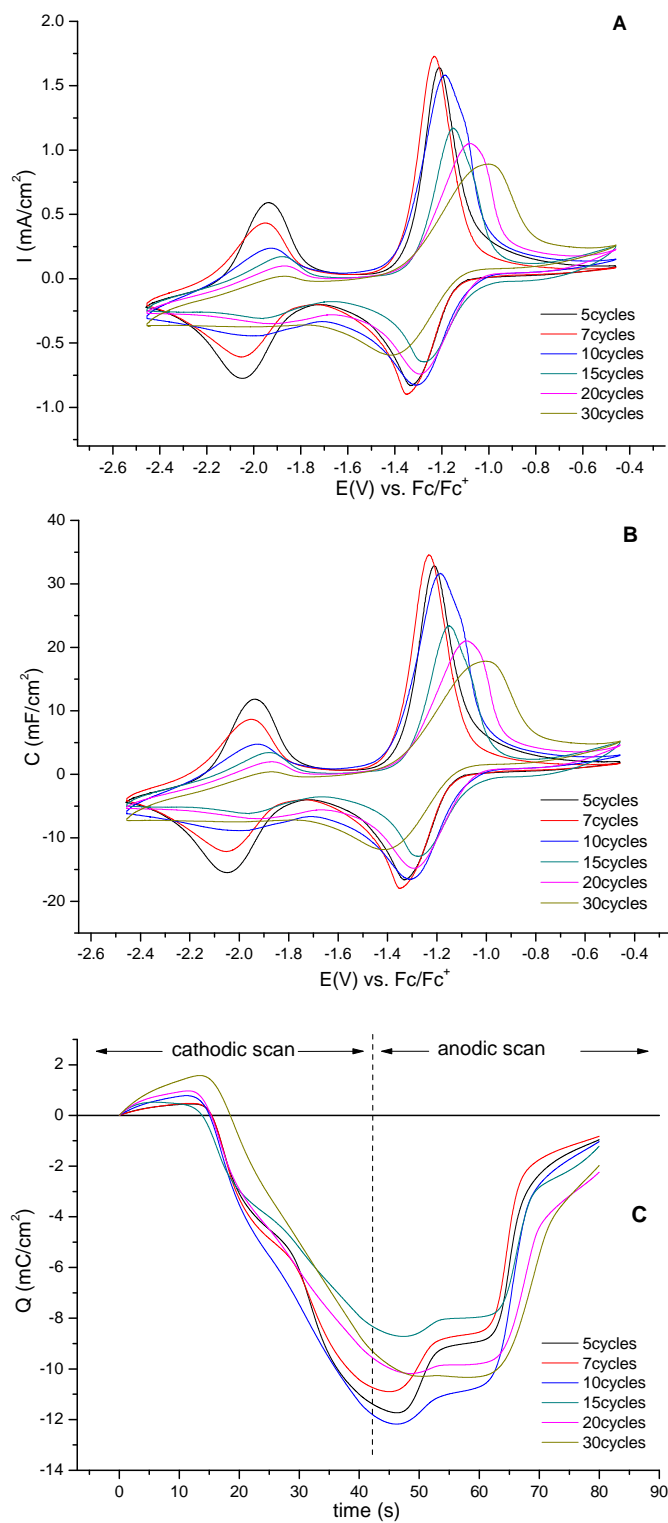


Figure 4-8. A) Cyclic voltammograms, B) capacitances as a function of applied potential and C) charge densities as a function of time of varying amounts of PBEDOT-TQ-Hx<sub>2</sub> (deposition cycles) at 50mV/s.

Table 4-1. Charge densities and capacitances of PBEDOT-BBT, PBEDOT-TQ-Me<sub>2</sub> and PBEDOT-TQ-Hx<sub>2</sub> with different deposition cycles.

# of dep. cycles	<b>PBEDOT-BBT</b> (1.5V)		<b>PBEDOT-TQ-Me<sub>2</sub></b> (1.75V)		<b>PBEDOT-TQ-Hx<sub>2</sub></b> (2.0V)	
	<i>Q</i> (mC/cm <sup>2</sup> )	<i>C</i> (mF/cm <sup>2</sup> )	<i>Q</i> (mC/cm <sup>2</sup> )	<i>C</i> (mF/cm <sup>2</sup> )	<i>Q</i> (mC/cm <sup>2</sup> )	<i>C</i> (mF/cm <sup>2</sup> )
<b>5cycles</b>					11.3	5.7
<b>7cycles</b>					10.5	5.2
<b>10cycles</b>	5.7	3.7			11.6	5.8
<b>15cycles</b>					8.1	4.1
<b>20cycles</b>	6.7	4.3	8.7	4.9	9.1	4.5
<b>30cycles</b>	10.8	6.9	9.9	5.7	9.3	4.7
<b>40cycles</b>	11.8	7.6	12.1	6.9		
<b>50cycles</b>	13.1	8.5	13.5	7.7		
<b>60cycles</b>	15.5	10.0	21.4	11.6		
<b>70cycles</b>	21.9	14.2	-	-		
<b>80cycles</b>	-	-				

In Table 4-1, the charge and the capacitance values with different amount of deposition cycles were summarized for all three DAD polymer systems. The average capacitance values were calculated from the voltammetric charges as follows;

$$C_p = (Q_a + Q_c)/2.E(V) \quad (4-1)$$

The capacitance values were expected to increase linearly with increasing number of deposition cycles, since the amount of charge consumed for each deposition is expected to be equal.

However, this was not observed for any of the polymers, likely due to the unavoidable experimental errors. In the case of PBEDOT-TQ-Me<sub>2</sub>, the highest amount of capacitance of 11.6mF/cm<sup>2</sup> was obtained with the 60 cycles of deposition. For the higher number of deposition cycles, the response of the reductive switching of the polymer resulted in voltammograms with the distorted shape. This was not surprising since the conducting polymer films lose their electrical response upon charging and discharging as the films get thicker, probably due to the kinetic limits of the ion intercalation and depletion processes. The same behavior was observed for PBEDOT-BBT with the maximum capacitance obtained 14.2mF/cm<sup>2</sup>. On the other hand, the

electrochemical responses of the PBEDOT-TQ-Hx<sub>2</sub> films were observed to be more sensitive to the loading of the polymer material. The highest capacitances obtained with PBEDOT-TQ-Hx<sub>2</sub> were calculated as 5.8mF/cm<sup>2</sup> for 30cycles deposition and the redox response of the polymers were decreased for the further deposition cycles. The slight inconsistency of the dependence of redox responses of all three polymers to the deposition cycles was probably caused by the difficulty to control all the electrochemical parameters for each experiment.

The environmental stabilities of n-type dopable systems are very poor due to the high reactivity of the radical anion charge carriers to oxygen and water. As such, obtaining a truly n-type doped system that exhibits reproducible coulombic efficiency with adequate stability is still a challenge in the field of conducting polymers.

The stability of n-type doping upon long-term charging and discharging is important for the use of these materials in device applications. As mentioned in the previous chapters, CPs undergo volume expansion and contraction when the oxidation level is changed due to the insertion and expulsion of ions during the redox doping and dedoping processes. Moreover, the stability of n-type doping is poor due to the high reactivity of the radical anion charge carriers to oxygen and water. Therefore, the stability of all three polymers were examined by exposing the films to nonstop continuous doping and dedoping processes by cyclic voltammetry in their potential range including both the first and second reduction processes at a scan rate of 50mV/s. The voltammograms of the films were recorded every 10 switches up to 1400 switches. The average charge consumed for anodic and cathodic scans in each voltammogram were calculated and the normalized charge values were plotted as a function of number of switching cycles for each P(DAD)s in Fig 4-9. Although the experiments were conducted in an argon-filled glove box (an oxygen and moisture free environment), a fast decrease in anodic and cathodic current

responses was observed. The capacitances of PBEDOT-BBT and PBEDOT-TQ-Hx<sub>2</sub> were dropped to 20% of the original values during the few hundreds of cycles. PBEDOT-TQ-Me<sub>2</sub> showed better stability than the other two DAD systems, however its capacitance also dropped to 20% of the original value after 1400 cycles. The instability of these polymers can be attributed to the less reversible second reductive doping process. Another reason might be the unavoidable trapped charges on the polymer system upon reductive doping causing the irreversible redox reactions, which are typically observed for conducting polymer systems. Consequently, the stabilities of the DAD polymers need to be improved.

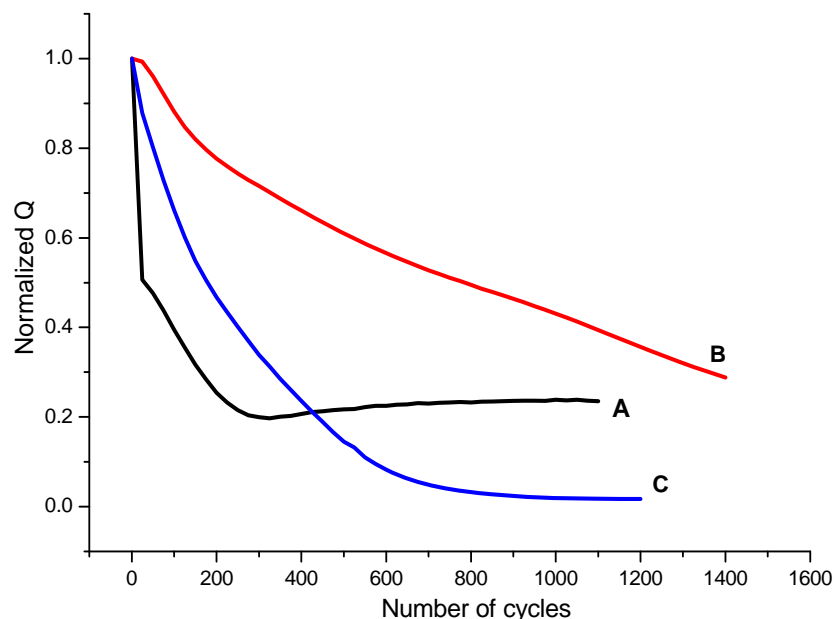


Figure 4-9. Stability of n-doping of A) PBEDOT-BBT, B) PBEDOT-TQ-Me<sub>2</sub> and C) PBEDOT-TQ-Hx<sub>2</sub> in TBAP/ACN by non-stop cycling at 50mV/s shown as normalized redox charges as a function of number of switching cycles.

### Type IV Supercapacitors

As was explained in the Introduction, the Type IV supercapacitors utilize conducting polymers that can be p- and n- dopable. They use an n-dopable polymer as the negative electrode and a p-dopable polymer as the positive electrode. During charging of the device, charges are being removed from the p-dopable polymer on positive electrode and are being transferred to the

n-dopable polymer on negative electrode. The created electron deficiency and the excess of electrons on the polymers were compensated by the appropriate counter ions; anions and cations from the electrolyte, respectively. Accordingly, when the anode p-dopable polymer is in the fully oxidized state and the cathode n-dopable polymer is in the fully reduced form, the device is in the fully charged state. Upon discharging of the device, both polymers neutralize and the ions are released back to the electrolyte solution. Consequently, it is very important to match redox (switching) charges of the two complementary polymers, prior to device construction for a balanced switching.

Type IV devices have an asymmetric configuration since they utilize two different polymers on the positive and the negative electrodes. In this study, the three DAD systems discussed so far, were combined with PProDOP as the negative and the positive electrode materials, respectively, in a Type IV supercapacitor device configuration. As was mentioned earlier, the aim of this study was to expand the cell voltage to achieve higher energy density in a polymer based electrochemical supercapacitor since the energy of a capacitor scales with the square of the cell voltage. Utilizing the DAD systems with PProDOP in a Type IV configuration expands the operating voltage range of the devices up to 3V. In Fig 4-10 the cyclic voltammograms of positive doping of PProDOP and the negative doping of PBEDOT-TQ-Me<sub>2</sub> as the representative of DAD systems, in TBAP/ACN at 50mV/s, are shown in the same potential scale. This figure demonstrates the extended operating voltage of the cell up to 2.75V. The voltage ranges for PBEDOT-BBT, PBEDOT-TQ-Me<sub>2</sub> and PBEDOT-TQ-Hx<sub>2</sub> were approximately found as 1.6V, 1.75V and 2V, respectively. Hence, the combination of these polymers with a 1V range of PProDOP in a Type IV configuration result in a total of 2.6V, 2.75 and 3V device working potential ranges.

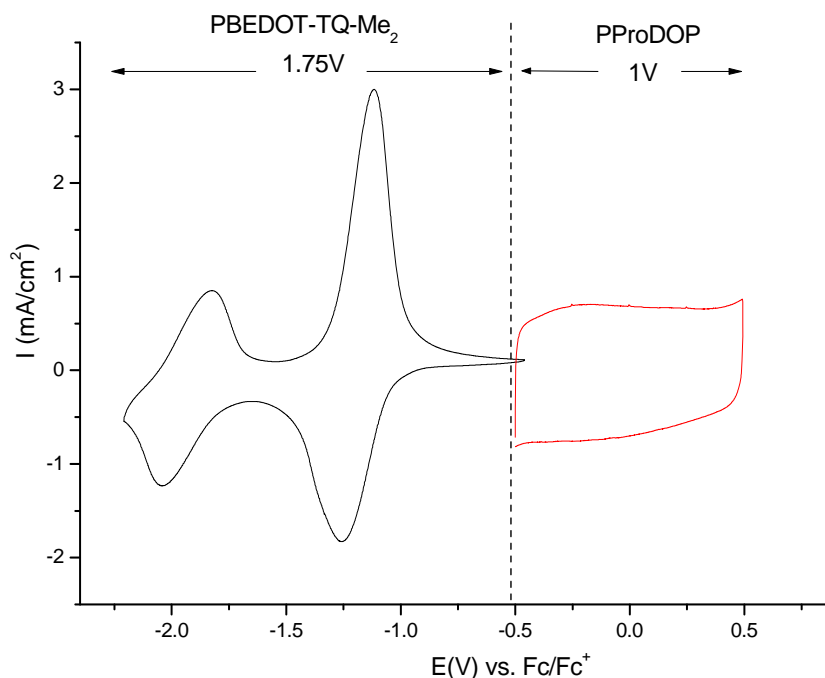


Figure 4-10. Expanding cell voltage of Type IV supercapacitor by combining PProDOP with PBEDOT-TQ-Me<sub>2</sub>. Positive doping of PProDOP and negative doping of PBEDOT-TQ-Me<sub>2</sub> in TBAP/ACN at 50mV/s.

The devices were fabricated using the films of each of three DAD systems that possessed the maximum capacitance values. To the best of our knowledge, the charging and discharging of conducting polymer based Type IV supercapacitors with two redox peaks, shown by cyclic voltammograms were not reported in the literature before. In order to examine the switching behavior of the two terminal device systems, the electrochemically deposited DAD films were combined with PProDOP films containing different amount of material into a device using TBAP/ACN as the conductive media between the electrodes. The PProDOP films were chosen as to display the redox charges upon switching in an excess, equal and limited amounts compared to the redox charges exhibited by P(DAD) of interest. In Figs 4-11, 4-12 and 4-13, the related experimental results were shown for each of the DAD systems. First, the redox switching charges of the DAD systems and of the varying PProDOPs were monitored during cathodic and anodic scans in a three-electrode cell containing 0.1M TBAP/ACN and were shown in the same

graph. In order to plot the switching charges of the polymers in the same scale, the normalized times were used. Additionally, the cyclic voltammograms at a scan rate of 50mV/s and the capacitances ( $\text{mF}/\text{cm}^2$ ) as a function of applied potentials of the TypeIV supercapacitors were also shown in the figures. Furthermore, the redox charges examined by integrating the voltammograms of devices over the entire potential range were also monitored and plotted as a function of time as shown in the following figures.

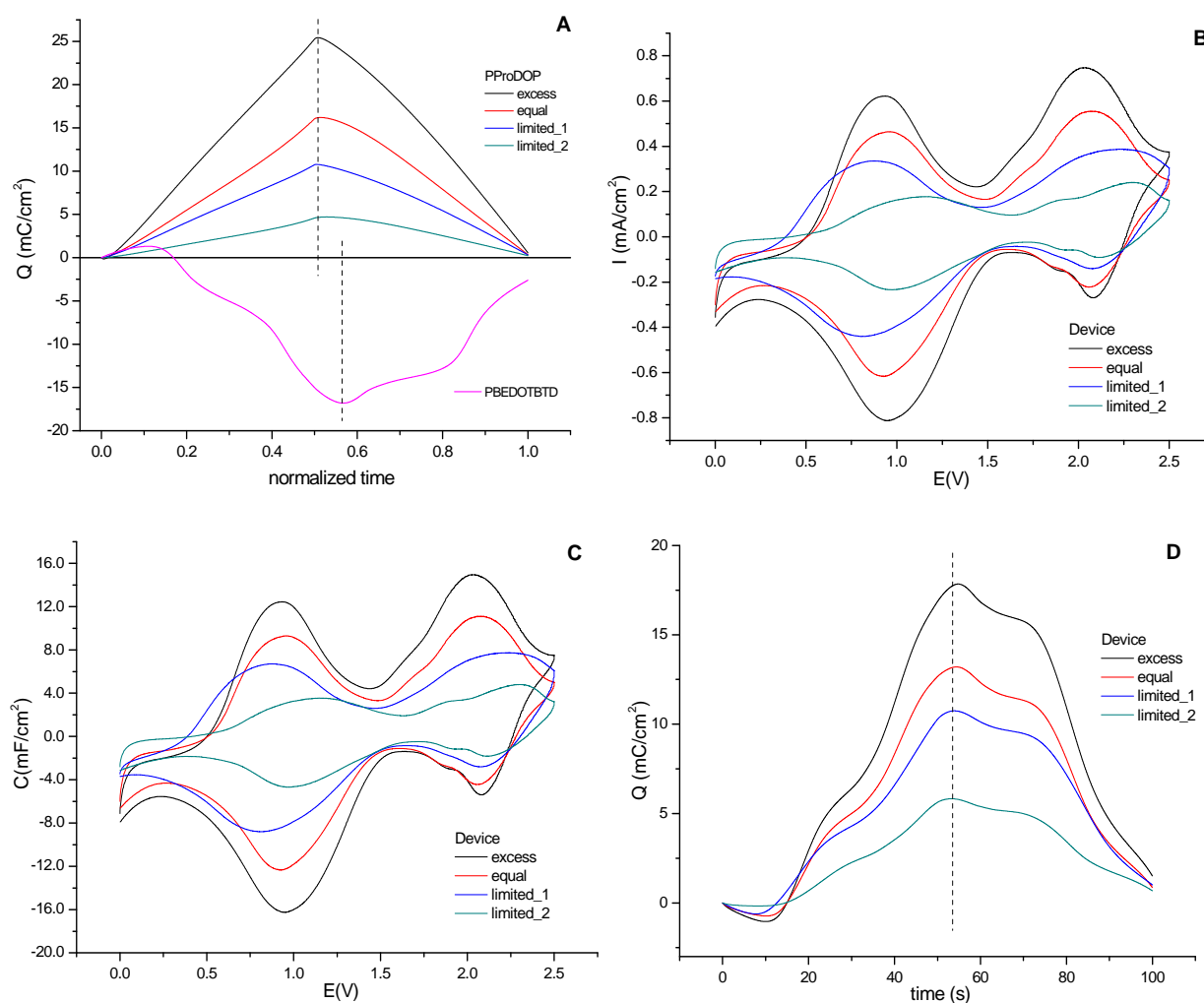


Figure 4-11. A) Charge densities as a function of time of PBEDOT-BBT and varying amount of PProDOPs in TBAP/ACN at 50mV/s. B) Cyclic voltammograms, C) capacitances as a function of applied voltage and D) charge densities as a function of time of the corresponding devices in TBAP/ACN at 50mV/s.

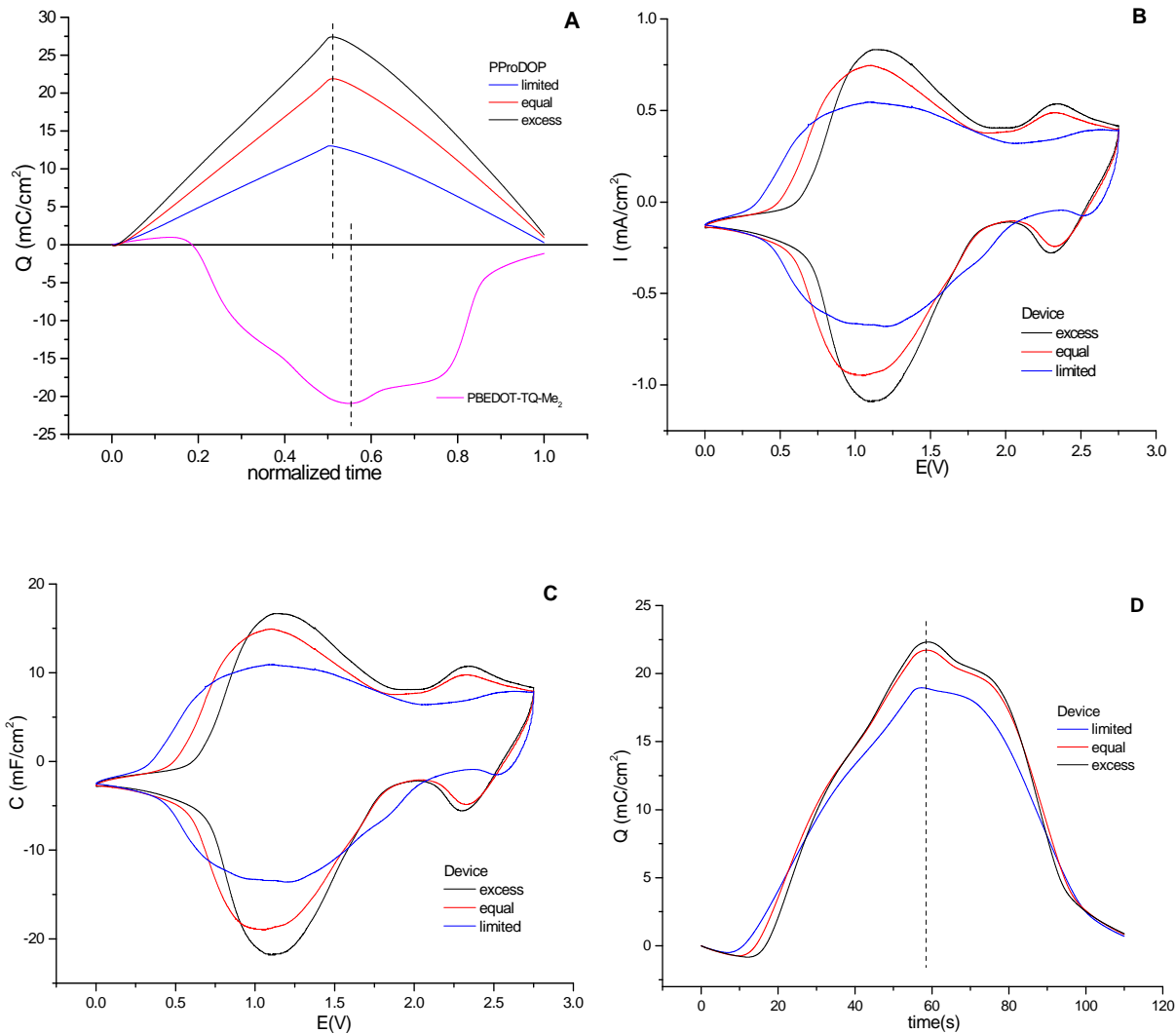


Figure 4-12. A) Charge densities as a function of time of PBEDOT-TQ-Me<sub>2</sub> and varying amount of PProDOPs in TBAP/ACN at 50mV/s. B) Cyclic voltammograms, C) capacitances as a function of applied potential and D) charge densities as a function of time of the corresponding devices in TBAP/ACN at 50mV/s.

The average capacitance values for supercapacitors containing different (excess, equal and limited) amounts of all P(DAD) systems were calculated from the redox charges obtained from the integrated voltammograms using Equation 4-1. The anticipated capacitances of devices were also calculated using the following equation with the capacitances of PProDOP and P(DAD) systems that were previously measured experimentally;

$$C_{Device} = \left[ \frac{1}{C_{PProDOP}} + \frac{1}{C_{P(DAD)}} \right]^{-1} \quad (4-2)$$

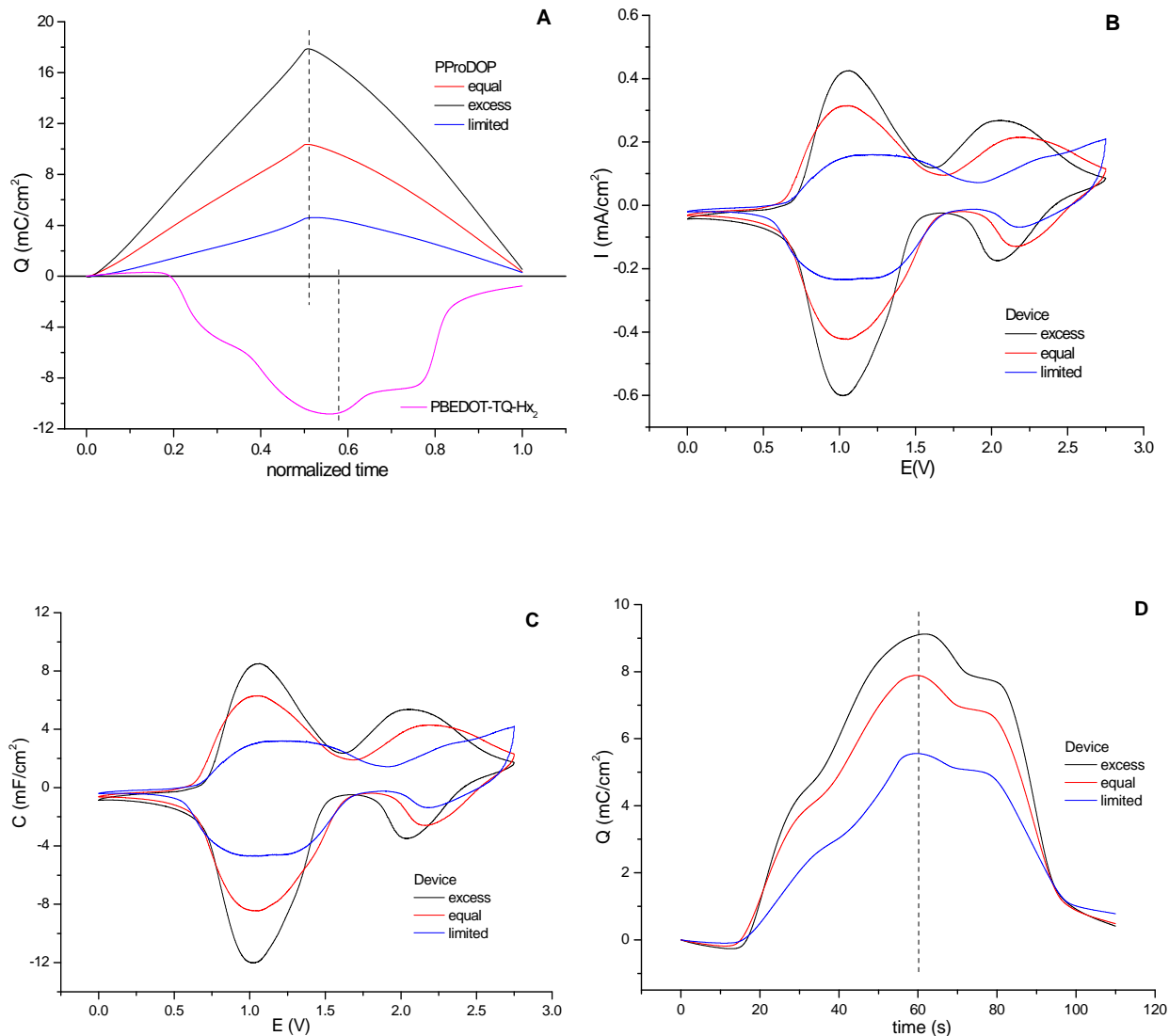


Figure 4-13. A) Charge densities as a function of time of PBEDOT-TQ-Hx<sub>2</sub> and varying amount of PProDOPs in TBAP/ACN at 50mV/s. B) Cyclic voltammograms, C) capacitances as a function of applied potential and D) charge densities as a function of time of the corresponding devices in TBAP/ACN at 50mV/s.

In Table 4-2, the results of Figs 4-11, 4-12 and 4-13 were summarized. The overall redox charges involved in the electrochemical processes of the DAD films of interest were reported in the first column with the name of P(DAD). In the second column, the redox charges exhibited by the chosen PProDOP films were presented. Finally, the redox charges displayed by the devices were shown along with the calculated capacitances of the devices.

During the charging and discharging process of the device, the charges are being released and loaded from one electrode to the other. As a result, the devices containing the equal and the excess amount of PProDOP were expected to show a similar cyclic voltammogram behavior to P(DAD) systems with two distinct redox processes. This is expected because the amount of charge needed by P(DAD) of interest will be compensated by the complementary PProDOP. In Figs 4-11B, 4-12B and 4-13B, the cyclic voltammograms of the supercapacitors exhibit two distinct redox processes, similar to the voltammograms of P(DAD) films measured in a three-electrode cell. These redox charges calculated for the devices were expected to be equal to the redox switching charges calculated for P(DAD)s. For example, the redox charges calculated for PBEDOT-TQ-Me<sub>2</sub> based devices containing equal (21.9mC/cm<sup>2</sup>) or excess (27.4mC/cm<sup>2</sup>) amount of PProDOP compared to P(DAD), demonstrated 21.7 and 22.3mC/cm<sup>2</sup> redox charges, as shown in Fig 4-12. These values are found to be quite close to 21.4mC/cm<sup>2</sup> which is observed originally for the switching of PBEDOT-TQ-Me<sub>2</sub>.

Alternatively, the devices containing the limited amount of PProDOP compared to the P(DAD) of interest were exhibited cyclic voltammogram similar to PProDOP for the first reduction for each system. The second reduction was observed to exhibit a distorted shape like an over oxidation peak generally observed for the conducting polymer systems. This was not surprising at all since there were not sufficient charges exhibited by PProDOP to compensate the charges needed for the full switching of P(DAD) of interest. As a result, the voltammograms show first reduction similar to switching of PProDOP itself with probably a combination of a compressed peak of the second reduction of P(DAD) and extended over oxidation peaks for PProDOP. However, it is very hard to predict the exact electrochemical processes occurring in the devices containing the unbalanced positive and negative charges.

Table 4-2. Charge densities and capacitances of devices prepared by PBEDOT-BBT, PBEDOT-TQ-Me<sub>2</sub> and PBEDOT-TQ-Hx<sub>2</sub> with different amount of PProDOP films.

	<i>PProDOP</i> <i>Q (mC/cm<sup>2</sup>)</i>	<i>Device</i> <i>Q (mC/cm<sup>2</sup>)</i>	<i>Device</i> <i>C=Q/V (mF/cm<sup>2</sup>)</i>	<i>Anticipated Capacitance</i> <i>1/C = 1/C<sub>PProDOP</sub> + 1/C<sub>P(DAD)</sub></i>
<i>p</i> (BEDOTBBT) <i>Q</i> =16.1mC/cm <sup>2</sup>	25	17.1	6.8	7.1
	16.0	12.8	5.1	6.2
	10.0	10.2	4.1	5.6
	4.6	5.4	2.2	3.1
<i>p</i> (BEDOT-TQ-Me <sub>2</sub> ) <i>Q</i> =21.4mC/cm <sup>2</sup>	13.0	18.9	6.5	6.1
	21.9	21.7	7.6	7.5
	27.4	22.3	8.1	8.0
<i>p</i> (BEDOT-TQ-Hx <sub>2</sub> ) <i>Q</i> =10.5mC/cm <sup>2</sup>	4.5	5.2	1.9	2.4
	10.1	7.7	2.8	3.5
	17.6	8.9	3.2	4.0

The experimentally observed average capacitance values were calculated for each device from the voltammetric charges over the operating voltage ranges as in the case of films. As seen in Table 4-2, the capacitances for the devices that were experimentally observed and the ones that were calculated from the separate film values are all in agreement with each other. The differences were most likely due to the unavoidable experimental errors. The highest amounts of capacitances, were observed as 6.8, 8.1 and 3.2mF/cm<sup>2</sup>, for PBEDOT-BBT, PBEDOT-TQ-Me<sub>2</sub> and PBEDOT-TQ-Hx<sub>2</sub>, respectively.

The difference between the cyclic voltammograms of the Type IV supercapacitors compared to Type I devices discussed in Chapter 3 is apparent. No current flow was observed until the potential of the device reached a certain point (which is about 0.7V) during switching of

Type IV supercapacitors, alternatively to the immediate increase observed for Type I supercapacitors. This was caused by the design of the Type IV configuration. All of the charge is delivered at higher voltages for Type IV devices upon discharging, while the voltage decays to 0V in the case of Type I supercapacitors. Therefore, higher power densities were predicted for Type IV device configurations.

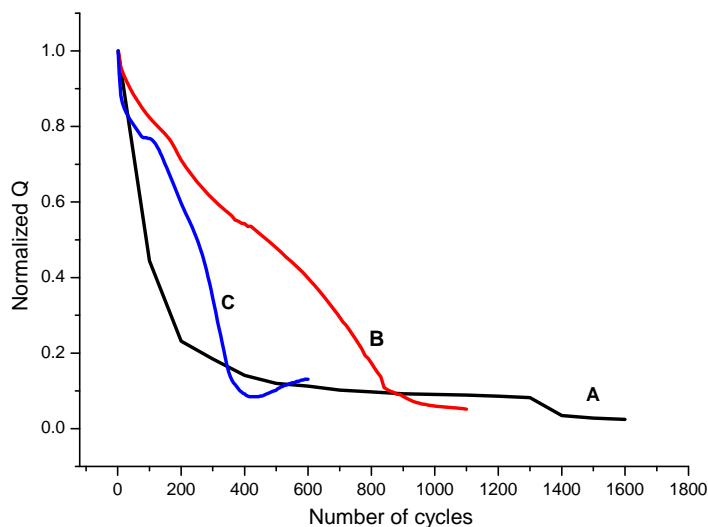


Figure 4-14. Stabilities of Type IV supercapacitors of A) PBEDOT-BBT, B) PBEDOT-TQ -Me<sub>2</sub> and C) PBEDOT-TQ-Hx<sub>2</sub> in TBAP/ACN at 50mV/s.

In regards to the films, the stability of devices upon long-term charging and discharging is very important. The cyclic stability of of all three supercapacitor systems containing the materials possessing equal amounts of charge upon switching, that were summarized in Table 4-2, were examined by continuous cyclic voltammetry at a scan rate of 50mV/s. The voltammograms of the films were recorded in every 10 switches until the films lost 90% of original capacitance. Here again the experiments were conducted in an oxygen and moisture free environment. The average redox charges involved in anodic and cathodic scans in each voltammogram were calculated and the normalized charge density values were plotted as a function of number of switching cycles for each supercapacitor system in Fig 4-11. The stability

of the devices are similar to the stabilities of the of P(DAD) films. Unfortunately, a fast decrease in anodic and cathodic current responses was observed. In almost 1000 cycles, devices lost 10% of the original capacitances. Among three P(DAD) based supercapacitors, the best stability was obtained for the PBEDOT-TQ-Me<sub>2</sub> based device.

### **Conclusions and Perspective**

In conclusion, this chapter presents the utilization of a new family of n-dopable electroactive polymers synthesized in the Reynolds' group, along with PProDOP in Type IV supercapacitors. This family includes BEDOT-BBT, BEDOT-TQ-Me<sub>2</sub> and BEDOT-TQ-Hx<sub>2</sub> which were designed based on an alternating donor and acceptor units. The energy stored in an electrochemical capacitor scales with the square of the cell voltage. Therefore, the key to achieving higher energy densities in an electrochemical supercapacitor is to expand the cell voltage. In Type IV supercapacitors, PProDOP were used as the p-dopable polymer on the positive electrode and DAD systems were used as the n-dopable polymers on the negative electrodes, which lead the operating voltage ranges of the devices to be enhanced up to 3V.

In this work, all the electroactive films have been electrochemically deposited on gold button electrodes. Further work to be conducted after this dissertation is anticipated to focus on optimizing the proper combination of these materials on larger scale electrodes. In order to achieve higher voltage ranges, ionic liquids can be a good candidate as the conducting media in between the electrodes.

## CHAPTER 5 HYBRID SUPERCAPACITORS: RUTHENIUM OXIDES|PProDOP

### Introduction

The materials studied for supercapacitor applications have focused on carbon, metal oxides and conducting polymers. As mentioned in Chapter 1, the electrochemical capacitors based on pseudocapacitance (or redox-capacitors) involving metal oxides and conducting polymers can provide higher energy density than conventional double layer capacitors based on carbon.<sup>1, 6, 14, 15, 24, 170, 171</sup> It has been demonstrated that PProDOP is a highly electron rich system having a quite low oxidation potential, easy to charge/discharge and show superior stability, especially when prepared as thin films. PProDOP is a promising energy storage material with a potential to be utilized in commercial supercapacitor devices. Although conducting polymers offers significant advantages as supercapacitor electrode materials, including fast and efficient switching between redox states, high electrical conductivity, suitable morphology, especially lightweight nature; their intrinsic degree of doping is limited to capacitance values of 100-250F/g.

On the other hand, metal oxides are attractive electrode materials for supercapacitors due to their high specific capacitance and low resistance. Among the transition metal oxides, hydrous ruthenium oxide ( $\text{RuO}_x \cdot n\text{H}_2\text{O}$ ) with a microporous structure has been recognized as the most promising supercapacitor material due to its intrinsic high electrochemical reversibility<sup>1</sup>, fast charge/discharge ability, ultrahigh specific pseudocapacitance, and excellent cycle life in acidic electrolyte solutions of  $\text{H}_2\text{SO}_4$ .<sup>55, 172, 173</sup> Depending on preparation procedures and measurement conditions, the specific capacitance ranges reported to date for hydrous ruthenium oxide have been between 600 to 860 F/g.<sup>54, 55, 172-183</sup> Recently a specific capacitance of 1340 F/g at a potential scan rate of 25 mV/s was reported for sol-gel derived ruthenium oxide nanodots loaded

on activated carbon.<sup>184</sup> Although the best charge storage capabilities of any capacitor reported to date have been achieved with hydrous ruthenium oxides, the high cost of ruthenium prevents its large-scale use.

The high capacitance density of  $\text{RuO}_x \cdot n\text{H}_2\text{O}$  has been attributed to the mixed protonic-electronic conduction. The charge storage process in ruthenium oxide electrodes is surface limited and progresses in several one electron steps, resulting in a broad range of capacitance values. It has been proposed that the hydrous regions within the nanoparticles allow facile proton permeation into the bulk material for efficient charge storage while the interconnected ruthenium oxide region accounts for the electronic conduction.<sup>55, 185</sup> Thus, a constant pseudocapacitance occurs over the full operating voltage range.

Combinations of conducting polymer materials with metal oxides have been prepared for different purposes in the literature. Composites of polyaniline doped with layered transition metal halides ( $\text{IrCl}_3 \cdot n\text{H}_2\text{O}$ )<sup>186</sup> have been synthesized to increase the stability of polymer material and improve its electrochemical properties to a level suitable for practical applications. Moreover, polypyrrole| $\text{RuO}_x \cdot n\text{H}_2\text{O}$  composite material have been synthesized by in situ chemical polymerization.<sup>187</sup> In one study, electrodes made by electrochemically deposited ruthenium oxide on conducting PEDOT were studied for supercapacitor applications and it has been observed that PEDOT| $\text{RuO}_x \cdot n\text{H}_2\text{O}$  composite electrodes exhibited large capacitance in acidic electrolytes. There have been some studies attempting to improve the capacitance of carbon nanotube materials by introducing metal oxides into their surfaces. The nanotubes have high conductivity, large surface areas and a 3D porous structure, and serve as a substrate for ruthenium oxide deposition.<sup>21, 188</sup> This work focuses on combining PProDOP with  $\text{RuO}_x \cdot n\text{H}_2\text{O}$  in order to improve energy storage capabilities of each component in the composite.

PProDOP, with its 3D porous structure, good conductivity, excellent reversible charge/discharge characteristics and superior stability, was expected to provide an ideal substrate for the deposition of ruthenium oxide.

In a composite material, it is essential for the working potentials of each material to match in order to take the advantage of the capacitance contribution of both materials. This was another reason to combine PProDOP which has a potential range from -0.4 to +0.6V vs. Ag/Ag<sup>+</sup> and RuO<sub>x</sub>·nH<sub>2</sub>O which exhibits redox processes between -0.2 and 1V vs. Ag/AgCl. It has been previously calculated that;

$$E_{1/2}(Ag/Ag^+) = E_{1/2}(Ag/AgCl) - 0.30V \quad (5-1)$$

Therefore, both these materials exhibit redox processes, resulting in high pseudocapacitance, in a similar potential range. As a result, the high charge storage ability of PProDOP, unlike bare nanotube substrates, would contribute to the overall capacitance of the composite material resulting in enhanced charge storage capabilities. Therefore, both the utilization of the ruthenium oxide on a specific area and the capacitance of the substrate itself would be improved by introducing a composite of PProDOP and RuO<sub>x</sub>·nH<sub>2</sub>O into an electrochemical capacitor of high quality.

### **Cyclic Voltammetric Deposition of Hydrous Ruthenium Oxide**

Hydrous ruthenium oxide was electrochemically prepared using cyclic voltammetry on the three different substrates: Au plate, Pt plate and SWNTs film. Electrodeposition was carried out on different substrates by potential cycling between -0.2V and 1.1V vs. Ag/AgCl at a scan rate of 50 mV/s, from an aqueous solution 5 mM RuCl<sub>3</sub>·xH<sub>2</sub>O, 0.1 M NH<sub>4</sub>Cl, and 0.01M HCl, with a pH of 2. The cyclic voltammograms of the deposition of RuO<sub>x</sub>·nH<sub>2</sub>O of 300 cycles on bare SWNTs are shown in Fig 5-1A.

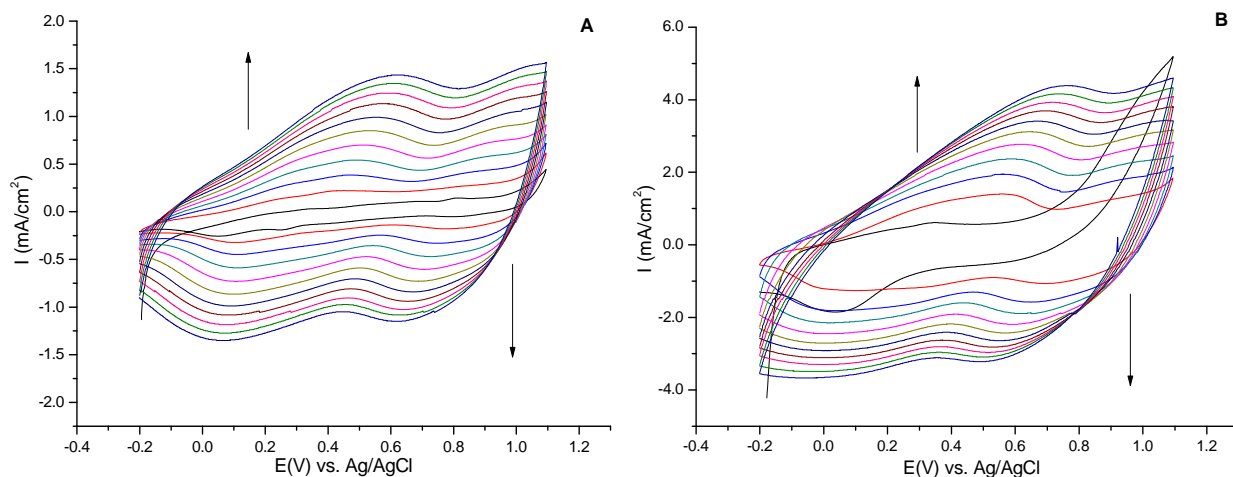


Figure 5-1. Electrochemical deposition (300 cycles) of  $\text{RuO}_x \cdot n\text{H}_2\text{O}$  from 5 mM  $\text{RuCl}_3 \cdot x\text{H}_2\text{O}$ , 0.01 M HCl, and 0.1 M  $\text{NH}_4\text{Cl}$  (pH=2) on A) bare SWNTs film and B) PProDOP|Sticky-PF|SWNTs substrate at 50mV/s.

From the voltammogram of ruthenium oxide deposition on bare SWNTs in Fig 5-1A, the presence of at least two redox couples at 0.3 and 0.9 V are apparent. The cathodic peaks at 0.05V on the negative sweeps is due to the reduction of Ru(III) species as it is deposited on the substrate. The peak at approximately 0.4V indicate the oxidation of already deposited ruthenium species (Ru metal and/or oxy-chloro-ruthenium species) to hydrous oxides ( $\text{RuO}_x \cdot n\text{H}_2\text{O}$ ) and then further oxidation to a higher oxidation state (i.e., hydroxyl Ru(VI) species) at 1V on the positive sweeps. Finally these further oxidized hydrous ruthenium oxides are reduced back to hydroxyl Ru(IV) species on the negative sweeps, then gradually reduced to lower oxidation states at more negative potentials. With the progression of the electrodeposition more  $\text{RuO}_x \cdot n\text{H}_2\text{O}$  is deposited onto the electrode which is evident by the increasing current densities as the CV cycles continue. However, a gradual distortion of the voltammograms of both redox processes occurs with increasing CV cycles. This shows that the reversibility of both redox processes decreases gradually since the peak potential differences increases by the progression of the CV deposition. This is attributed to the IR drop that occurs on more thickly deposited ruthenium

oxide layers due to an increased proton diffusion path/barrier. The redox behavior of  $\text{RuO}_x \cdot n\text{H}_2\text{O}$  also exhibits hysteresis with increasing CV cycles.

Fig 5-1B shows the voltammograms of ruthenium oxide deposition on PProDOP which had been previously deposited on Sticky-PF coated SWNTs films. The initial capacitance of this PProDOP layer was measured as  $8\text{mF}/\text{cm}^2$ . Compared to Fig 5-1A, the two redox peaks at 0.3 and 0.9 V are not as distinct as they appear on Fig 5-1A. The general appearance of the voltammogram in Fig 5-1B resembles the voltammograms on Fig 5-1A with positively shifted anodic and negatively shifted cathodic peaks. These peaks are broader probably, due to the PProDOP layer undergoing capacitive charging/discharging as  $\text{RuO}_x \cdot n\text{H}_2\text{O}$  is deposited. Therefore the peaks appear as a combination of the redox peaks due to the deposition of  $\text{RuO}_x \cdot n\text{H}_2\text{O}$  with the ox/red peaks of the PProDOP layer. The two distinct cathodic peaks can still be observed as in Fig 5-1A with a negative shift of approximately  $-0.1\text{V}$ . The cathodic peak at  $-0.05\text{V}$  is the indication of the deposition of  $\text{RuO}_x \cdot n\text{H}_2\text{O}$  as the Ru(III) species reduced and the cathodic peak at  $+0.5\text{V}$  is indicative of the reduction of the already oxidized hydrous ruthenium oxides to hydroxyl Ru(IV) species as it does in Fig 5-1A. The positive and negative shifts seen in anodic and cathodic scans respectively are due to the more resistive modified electrode surface with PProDOP.

Besides being shifted and broader, the voltammogram peaks in Fig 5-1B show higher current densities compared to those in Fig 5-1A by almost 3 times. The progression of the anodic peak current densities of the ruthenium oxide deposition at  $0.6\text{V}$  on bare SWNTs and at  $0.7\text{V}$  vs. Ag/AgCl on PProDOP|Sticky-PF|SWNTs with the deposition cycle numbers up to 300 cycles are shown in Fig 5-2A and B, respectively. The peak current density for the oxide deposition process on both substrates shows logarithmic increase with increasing deposition

cycle number. The amount and rate of ruthenium oxide deposition on PProDOP is clearly faster than its deposition on bare SWNTs, resulting higher current densities for the same value of the deposition cycle numbers and higher slope in the graphs. The higher initial current density observed in Fig 5-2B is due to the capacitive response of the already existing PProDOP layer. These results likely indicate the deposition of more ruthenium oxide due to the increased surface area of the electrode. The rough and porous surface of PProDOP possibly allows ruthenium oxide deposition throughout the volume of the polymer layer.

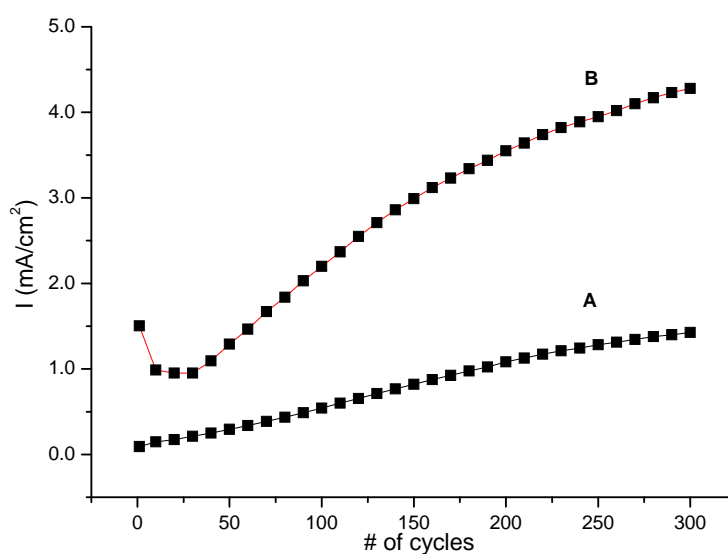


Figure 5-2. Peak current densities of  $\text{RuO}_x \cdot n\text{H}_2\text{O}$  deposition on A) bare SWNTs film at  $0.6\text{V}_{\text{Ag}/\text{AgCl}}$  and on B) PProDOP ( $8\text{mF}/\text{cm}^2$ ) on Sticky-PF|SWNTs substrate at  $0.7\text{V}_{\text{Ag}/\text{AgCl}}$  as a function of number of deposition cycles.

## Characterization of $\text{RuO}_x \cdot n\text{H}_2\text{O}$ and Composite Films of $\text{RuO}_x \cdot n\text{H}_2\text{O}$ with PProDOP

### Electrochemical Characterization

Cyclic voltammetry was used to determine the electrochemical properties of electrochemically prepared ruthenium oxide films and composites of ruthenium oxide and PProDOP. In order to determine the capacitance of PProDOP before the deposition of ruthenium oxide, it is essential to look at the CV behavior of PProDOP in an acidic medium compared to its

voltammograms in acetonitrile. In Fig 5-3A and B, the voltammograms and capacitances as a function of applied voltage of PProDOP deposited on Sticky-PF coated SWNTs film, respectively, first in LiBTI/ACN, then in 0.5M H<sub>2</sub>SO<sub>4</sub> solution and finally again in LiBTI/ACN media are shown to confirm the reproducibility of the CV behavior of PProDOP in an acidic medium. The differences between the CV behavior and the capacitance values of PProDOP in these two different media were found to be insignificant as seen in the Fig 5-3.

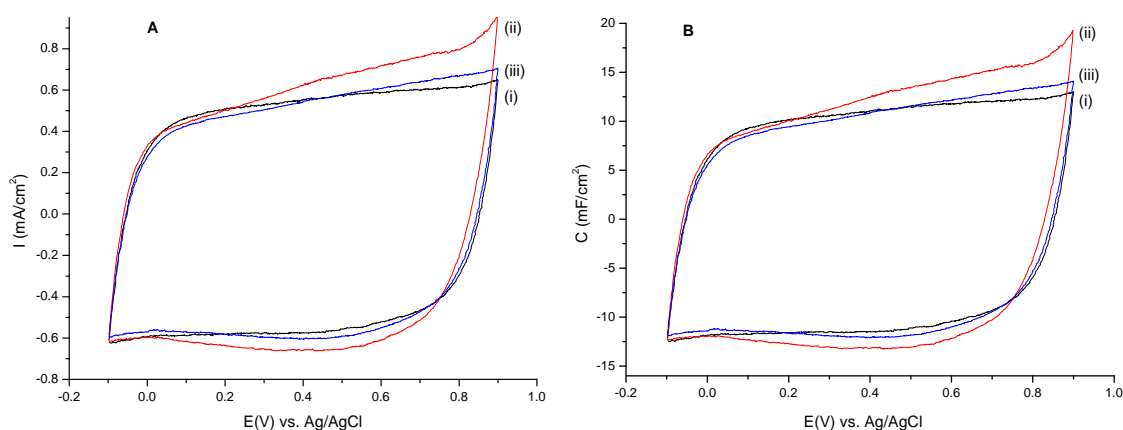


Figure 5-3. A) Cyclic voltammograms and B) capacitances as a function of applied voltage of PProDOP on Sticky-PF/SWNTs first in (i) LiBTI/ACN, then in (ii) 0.5M H<sub>2</sub>SO<sub>4</sub> and finally again in (iii) LiBTI/ACN. (Note that LiBTI/ACN experiments vs Ag/Ag<sup>+</sup> reference was adjusted to Ag/AgCl reference for comparison of the voltammograms in the same scale.)

Typical CV diagrams measured in a 0.5 M H<sub>2</sub>SO<sub>4</sub> solution at potential scan rates from 10 to 50mV/s of electrochemically prepared RuO<sub>x</sub>·nH<sub>2</sub>O/SWNTs film and RuO<sub>2</sub>·nH<sub>2</sub>O |PProDOP|Sticky-PF|SWNTs film electrodes are shown in Fig 5-4A and C, respectively. The respective deposition of RuO<sub>x</sub>·nH<sub>2</sub>O was halted at the equivalent of 300cycles on both substrates. In Fig 5-4A, voltammograms exhibit typical pseudocapacitive behavior of ruthenium oxide. The voltammograms maintained their shape at all potential scan rates from 10 to 50mV/s as shown in Fig 5-4A, revealing the reversible high-power characteristics of ruthenium oxide. The current densities of the redox peaks in the potential region of 100 to 800 mV of each voltammograms at

different potential scan rates are linearly proportional to the scan rate. This result implies that the redox transitions between the oxyruthenium species at various oxidation states are not diffusion limited at these scan rates. Slight gradual distortions of the CV curves with the increase in peak potential differences of the redox pairs were observed which can be attributed to more resistive switching as the potential scan rate increases. However, the pseudocapacitive electrochemical response of ruthenium oxide was still quite reversible.

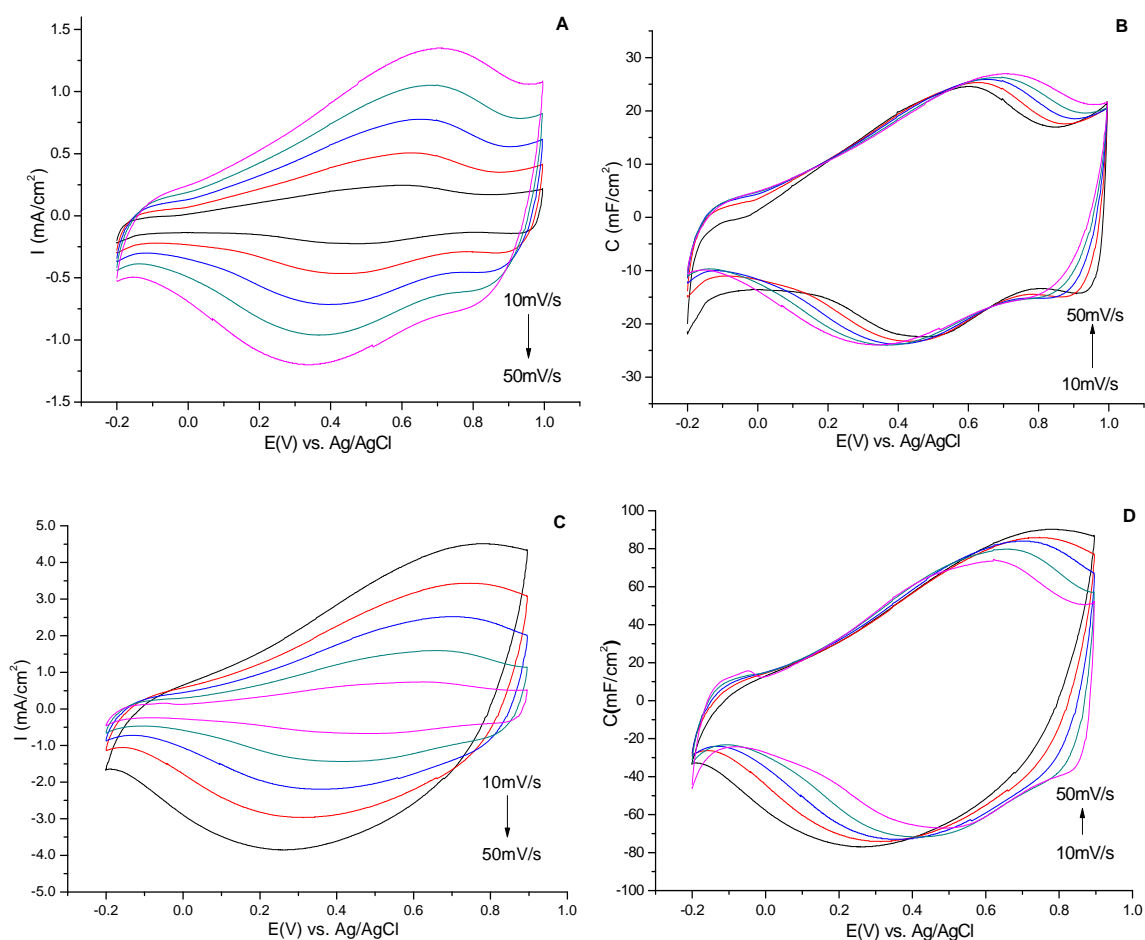
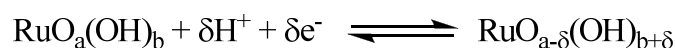


Figure 5-4. A&C) Cyclic voltammograms and B&D) capacitances as a function of applied potential of  $\text{RuO}_x \cdot n\text{H}_2\text{O}$  (300 deposition cycles) on A&B) bare SWNTs film and B&D) PProDOP|Sticky-PF|SWNTs substrates in 0.5M  $\text{H}_2\text{SO}_4$  at 10 to 50mV/s with 10mV/s intervals.

The high capacitive characteristics of the hydrous ruthenium oxides are due to the redox transitions of the surface sites on the very large surface area of the material. Although the charge

storage mechanism of ruthenium oxide is not yet fully understood, the interfacial electroactive oxyruthenium species at various oxidation states present redox transitions by exchanging protons with the electrolyte H<sub>2</sub>SO<sub>4</sub> solution corresponding to the following nonstoichiometric equation:<sup>173, 189</sup>



The broad redox peaks seen in the potential region of 100 to 800 mV in Fig 5.3A can be attributed to the combination of redox processes due to the transitions of Ru(IV)/Ru(III)/Ru(II) and Ru(VI)/Ru(IV) redox couples in H<sub>2</sub>SO<sub>4</sub> media.<sup>189</sup>

In Fig 5-4C, voltammograms of the composites of RuO<sub>x</sub>·nH<sub>2</sub>O with PProDOP exhibits mostly featureless very broad redox peaks in both anodic and cathodic scans resembling a combination of a typical CV behavior of PProDOP itself and RuO<sub>x</sub>·nH<sub>2</sub>O itself in Fig 5-4A. The peak potentials were found to be shifted and the differences between the redox peak potentials are found to be greater than RuO<sub>x</sub>·nH<sub>2</sub>O itself as was explained for the electrochemical deposition process of the ruthenium oxide on PProDOP. In addition, the gradual distortion of the CV curves with increasing scan rate resembles the voltammograms of RuO<sub>x</sub>·nH<sub>2</sub>O itself as seen in Fig 5-4A. Since all voltammograms in Fig. 5-4C show electrochemically reversible behavior in the H<sub>2</sub>SO<sub>4</sub> solution, the conductivity of these composite films must be significant. The current densities of the redox peaks in each voltammograms at different potential scan rates are again linearly proportional to the scan rates, revealing that the redox transitions of the composite material are not diffusion limited even at these scan rates. Accordingly, there is no significant proton diffusion barrier on composite films. Overall, the composites exhibit voltammograms that are more rectangular in shape than those of RuO<sub>x</sub>·nH<sub>2</sub>O itself, which is indicative of ideal pseudocapacitive behavior.

Fig 5-4B and d show the capacitance as a function of applied potential of  $\text{RuO}_2 \cdot n\text{H}_2\text{O}|\text{SWNTs}$  film and  $\text{RuO}_x \cdot n\text{H}_2\text{O}|\text{PProDOP}|\text{Sticky-PF}|\text{SWNTs}$  film electrodes at different potential scan rates from 10 to 50mV/s in 0.5M  $\text{H}_2\text{SO}_4$ , respectively. The average capacitance values are calculated from the voltammetric charges examined by integrating the anodic and cathodic scans over the potential ranges;  $C_p = (Q_a + Q_c) / 2 E$ .

The effect of the substrates on the utilization of the ruthenium oxide is obvious from the current densities and capacitance values shown in Fig 5-4C and D, respectively. The capacitances of  $\text{RuO}_2 \cdot n\text{H}_2\text{O}$  calculated at 50mV/s for the films deposited on bare SWNTs film (Fig 5-4B) and on porous PProDOP (Fig 5-4D) were found to be 18mF/cm<sup>2</sup> and 45mF/cm<sup>2</sup>, respectively. A comparison of these capacitances of the analogous 300 cycle-deposition of ruthenium oxide on these two substrates shows that the capacitance increased by a factor of 2.5 with  $\text{RuO}_2 \cdot n\text{H}_2\text{O}$  on PProDOP. This indicates the high charge storage capability of the  $\text{RuO}_2 \cdot n\text{H}_2\text{O}|\text{PProDOP}$  composite film electrodes.

An increase in the capacitance value of the composite material of  $\text{RuO}_2 \cdot n\text{H}_2\text{O}|\text{PProDOP}$  compared to the  $\text{RuO}_x \cdot n\text{H}_2\text{O}$  itself is expected assuming that there would be a contribution from the PProDOP to the total capacitance. However, the contribution ratio of the capacitance of PProDOP to the composite is important. In Fig 5-5A and B, the voltammogram and the charges as a function of the applied potential taken from the same voltammograms of PProDOP before ruthenium oxide deposition and the voltammogram of the composite material (Fig 5-4C) at 50mV/s in 0.5M  $\text{H}_2\text{SO}_4$  are shown. As mentioned before, the capacitance of PProDOP was determined to be 8mF/cm<sup>2</sup> before ruthenium oxide deposition and 45mF/cm<sup>2</sup> after ruthenium oxide deposition. The capacitance of PProDOP increased by 5.6 times with the introduction of  $\text{RuO}_2 \cdot n\text{H}_2\text{O}$  to the matrix.

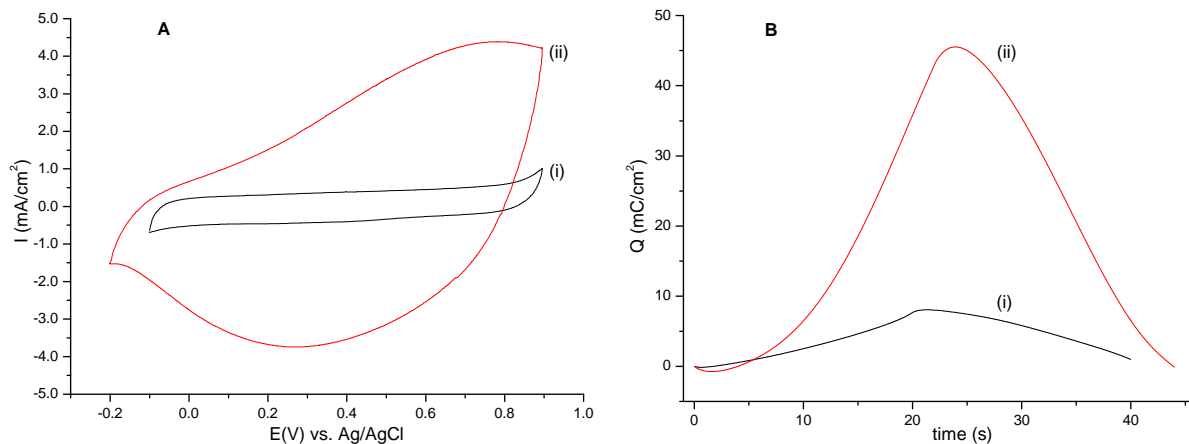


Figure 5-5. A) Cyclic voltammograms and B) charge densities as a function of time of (i) PProDOP before the  $\text{RuO}_x \cdot n\text{H}_2\text{O}$  deposition and of (ii) composite films in 0.5M  $\text{H}_2\text{SO}_4$  at 50mV/s.

In the assumption of the total capacitance of the composite material to be the sum of the individual capacitances exhibited by each material; ( $C_{\text{Composite}} = C_{\text{PProDOP}} + C_{\text{RuOx}}$ ), it is essential to calculate the contributions of each components. In order to determine the capacitance of ruthenium oxide, the capacitance of PProDOP itself ( $8\text{mF}/\text{cm}^2$ ) measured before the ruthenium oxide deposition was subtracted from the final capacitance of the composite material ( $45\text{mF}/\text{cm}^2$ ). The contribution of only ruthenium oxide is found to be  $37\text{mF}/\text{cm}^2$ . Compared to the capacitance values of the ruthenium oxide for same 300 cycles of deposition on bare SWNTs electrode ( $18\text{mF}/\text{cm}^2$ ), the capacitance of the ruthenium oxide increased by 100% on PProDOP substrates, which indicates extremely high electrochemical utilization of ruthenium oxide on a polymer substrate, even with the assumption that the that the whole  $8\text{mF}/\text{cm}^2$  capacitance of PProDOP, exhibited before the ruthenium oxide deposition, contributed to the final capacitance of the composite.

The results in Fig 5-2 and 5-5 indicate that the introduction of ruthenium oxide into the PProDOP matrix greatly enhance the capacitive response of composite material. Moreover, the utilization of ruthenium oxide is greatly improved through the introduction of a polymer

substrate with a porous structure compared to relatively thin layer of SWNTs film. As determined for the PProDOP supercapacitors in Chapter 3, here the capacitance of ruthenium oxide is also found to depend strongly on the substrate employed.

To follow the pathway of ruthenium oxide deposition on PProDOP, with each sample having near the same amount of ruthenium oxide; a 300cycles worth was deposited on different amount of PProDOP electrodes. In Fig 5-6, the resulting capacitances of the composite material were plotted as a function of the initial capacitance of the PProDOP layer before the ruthenium oxide deposition. The different capacitance values of PProDOP are reasonably indicative of the different film thicknesses. In Fig 5-6, with increasing PProDOP mass, the capacitance of the composite film increases linearly, stabilizes at a level of about  $\sim 45\text{mF/cm}^2$  and then drops slowly to a value almost equal to the initial PProDOP capacitance. As mentioned above, the increase in the capacitance of the composite material is expected with the increase in the amount of PProDOP, considering the contribution of PProDOP to the total composite capacitance. However, it is obvious from the Fig 5-6 that the ruthenium oxide deposition becomes ineffective with increased PProDOP thickness.

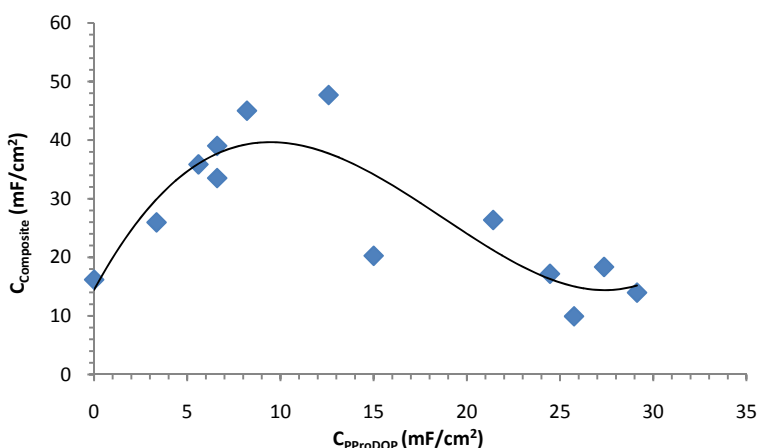


Figure 5-6. Capacitances of the composite ( $\text{RuO}_x \cdot n\text{H}_2\text{O}$  and PProDOP) as a function of the initial capacitance of PProDOP before the ruthenium oxide deposition.

Moreover, the capacitance of  $\text{RuO}_x \cdot n\text{H}_2\text{O}$  (deposited for 300cycles) calculated by subtraction of the capacitance of the initial PProDOP (before the ruthenium oxide deposition) from the total capacitance of the composite material is plotted as a function of the capacitance of PProDOP and is shown in Fig 5-7. The negative values found for  $\text{RuO}_x \cdot n\text{H}_2\text{O}$  (for the values beyond  $15\text{mF}/\text{cm}^2$  in Fig 5-6) are not included in Fig 5-7. An increase in the capacitance of  $\text{RuO}_x \cdot n\text{H}_2\text{O}$  with the increasing PProDOP thickness, up to a certain point, is observed, as seen in the total capacitance of composite in Fig 5-6. This result indicates that the deposition of the  $\text{RuO}_x \cdot n\text{H}_2\text{O}$  increases with the increasing PProDOP amount. Therefore it is obvious that the increase in the total capacitance of the composite material is not solely due to the contribution of the increased amount of PProDOP.

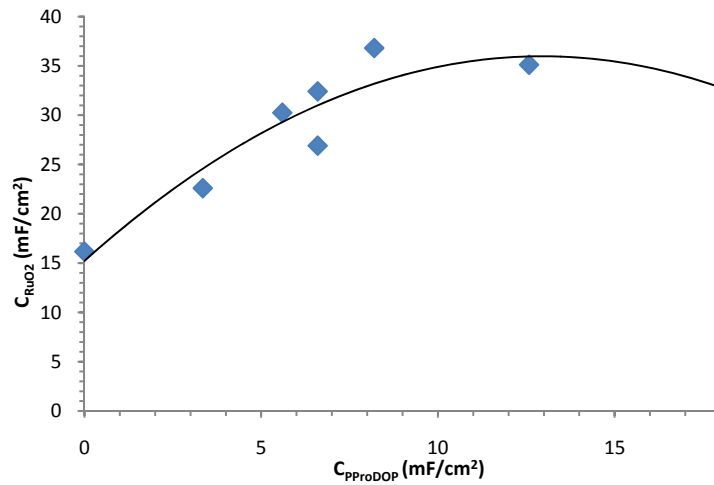


Figure 5-7. Capacitances of the  $\text{RuO}_x \cdot n\text{H}_2\text{O}$  (in the composite) as a function of the initial capacitance of PProDOP before the ruthenium oxide deposition.

The results in Fig 5-6 and 5-7 show that ruthenium chloride species diffuse through the polymer matrix to the current collector substrate and formation of  $\text{RuO}_x \cdot n\text{H}_2\text{O}$  occurs throughout the polymer matrix, probably covering the polymer surface. Therefore, the initial linear dependence of the capacitance of the composite to the relatively thinner PProDOP layers (up to  $12\text{mF}/\text{cm}^2$ ) is observed in Fig 5-6. If  $\text{RuO}_x \cdot n\text{H}_2\text{O}$  were to be forming only as a top layer on the

surface of PProDOP but now diffusing through the matrix, the capacitance of ruthenium oxide would be expected to show a stable dependence instead of linear increase with the increasing PProDOP thickness since there would be no significant difference between the surfaces of the polymer layer with different thicknesses. Accordingly, a barrier occurs in the diffusion of ruthenium chloride species through the polymer matrix to the current collector substrate as the PProDOP layer gets thicker. Therefore, there is a low or almost inhibited deposition of ruthenium oxide occurring on thicker layer of PProDOPs, resulting in the lower capacitances of the final composite. In conclusion, optimization of the thickness of the conducting polymer film layer to a certain amount of ruthenium utilization is necessary to realize large specific capacitance from the composite material.

Furthermore, either the ruthenium deposition rate changes or some portion of deposited ruthenium oxide must be not participating in the electrochemical response of the composite material, in the range where the capacitance stabilizes with increasing PProDOP thickness, which would eventually reduces the specific capacitance. Consequently, the electrochemical utilization of ruthenium oxide is confined to the thin films of PProDOP.

The mass of the composite material with the capacitance ( $45\text{mF}/\text{cm}^2$ ) was measured by directly weighing the material and found as  $68\mu\text{g}/\text{cm}^2$ . Consequently, the maximum specific capacitance of the composite film was calculated as  $660\text{F}/\text{g}$ . However, an inconsistency arises compared to the mass of the PProDOP before the  $\text{RuO}_2 \cdot n\text{H}_2\text{O}$  deposition. These results reasonably direct to the conclusion that the most of PProDOP is being dissolved into the solution during the deposition of  $\text{RuO}_x \cdot n\text{H}_2\text{O}$ , yet PProDOP still increases the deposition amount of  $\text{RuO}_2 \cdot n\text{H}_2\text{O}$  per unit area, compared to the deposition of  $\text{RuO}_x \cdot n\text{H}_2\text{O}$  on bare SWNTs.

## SEM Analysis

The surface morphologies of the composites of  $\text{RuO}_x \cdot n\text{H}_2\text{O}$  and PProDOP were examined by SEM. The SEM images of  $\text{RuO}_x \cdot n\text{H}_2\text{O}$  deposited for 300 cycles on bare SWNTs film and on PProDOP/Sticky-PF/SWNTs film electrodes are shown in Fig 5-8A and B respectively.

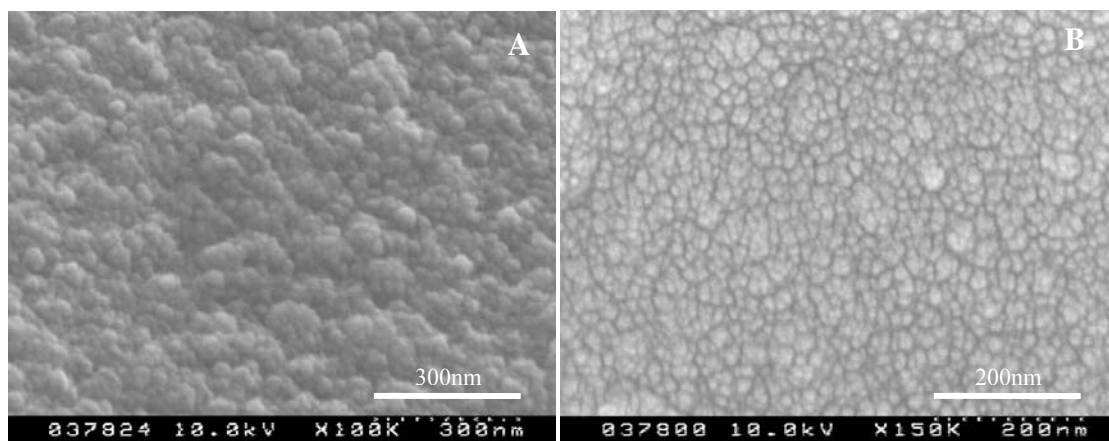


Figure 5-8. Scanning electron micrographs of  $\text{RuO}_x \cdot n\text{H}_2\text{O}$  (300 deposition cycles) on A) bare SWNTs film and B) PProDOP|Sticky-PF|SWNTs substrates.

The SEM images of both films have demonstrated homogeneous morphologies. Compared to the AFM image of SWNT film in Fig 3-15, it is clear in Fig 5-8 that  $\text{RuO}_x \cdot n\text{H}_2\text{O}$  layer forms a sufficiently thick layer to cover the surface of SWNTs since the noodle-like structure of the nanotube bundles cannot be realized underneath this layer. In general the surface images of both films;  $\text{RuO}_x \cdot n\text{H}_2\text{O}$  only and the composite of  $\text{RuO}_x \cdot n\text{H}_2\text{O}$  with PProDOP shown in Fig 5-8A&B, respectively, reveal similar nodular structures showing spherical grains in various sizes with a compact morphology. There have been several cracks observed under SEM throughout the both films. Since the pseudocapacitance of ruthenium oxide is directly proportional to its active surface area and the electrochemical response of these films were observed to be very reversible, the micropores must be distributed in between the grains in order to support the efficient proton diffusion. This morphology might be due to the collapsing of the porous structured films forming

a compacted structure during the drying processes used to evaporate the residual solvent trapped inside the matrix of the films. There also no distinctive trends that were observed from the cross section of the films. The surface morphologies of these films also show similar structures compared to that of PProDOP alone (Fig 3-22) which probably have a less rough surface. These images also support the hypothesis that  $\text{RuO}_x \cdot n\text{H}_2\text{O}$  deposits are distributed throughout the matrix of the PProDOP film and also covering the surface.

### **XPS Analysis**

For the elemental inspection of the prepared composite film, the XPS spectra of films both with and without  $\text{RuO}_x \cdot n\text{H}_2\text{O}$  were taken as shown in Fig 5-9A and B, respectively. In both spectra the peaks due to C, N, and S along with the advantageous oxygen peak observed. Since the binding energies of Ru 3d and C 1s, which is the dominant element in the composite material, interfere with each other, it was necessary to examine Ru 3p1 and 3p3 peaks as the evidence of the  $\text{RuO}_x \cdot n\text{H}_2\text{O}$  existence in the spectrum of the composite. The peaks at binding energies of both Ru 3p1 and 3p3 are broad which indicates that the oxide film are consists of mixed hydroxyl ruthenium species in various oxidation states. From the comparison of the Ru 3p3 with N 1s peaks, the percentages of these species were found to be 52.3% and 47.5, approximately in 1:1 ratio. The absence of any F 1s peak in the spectra of the composite as in the spectra of PProDOP|Sticky-PF|SWNTs electrode and also the increased percentage of S 2s and 2p3 peaks in the spectrum of the composite compared to that of PProDOP|Sticky-PF|SWNTs electrode indicate that the PProDOP is probably doped with  $\text{SO}_4^-$  or  $\text{HSO}_4^-$  instead of  $(\text{N}_2(\text{SO}_2\text{CF}_3))^-$  dopant anion. However, it is difficult to make an exact quantitative analysis since there were small impurities found on both samples. Accordingly, XPS results only show the existence of the mixed oxidation states of ruthenium oxide species in the composite.

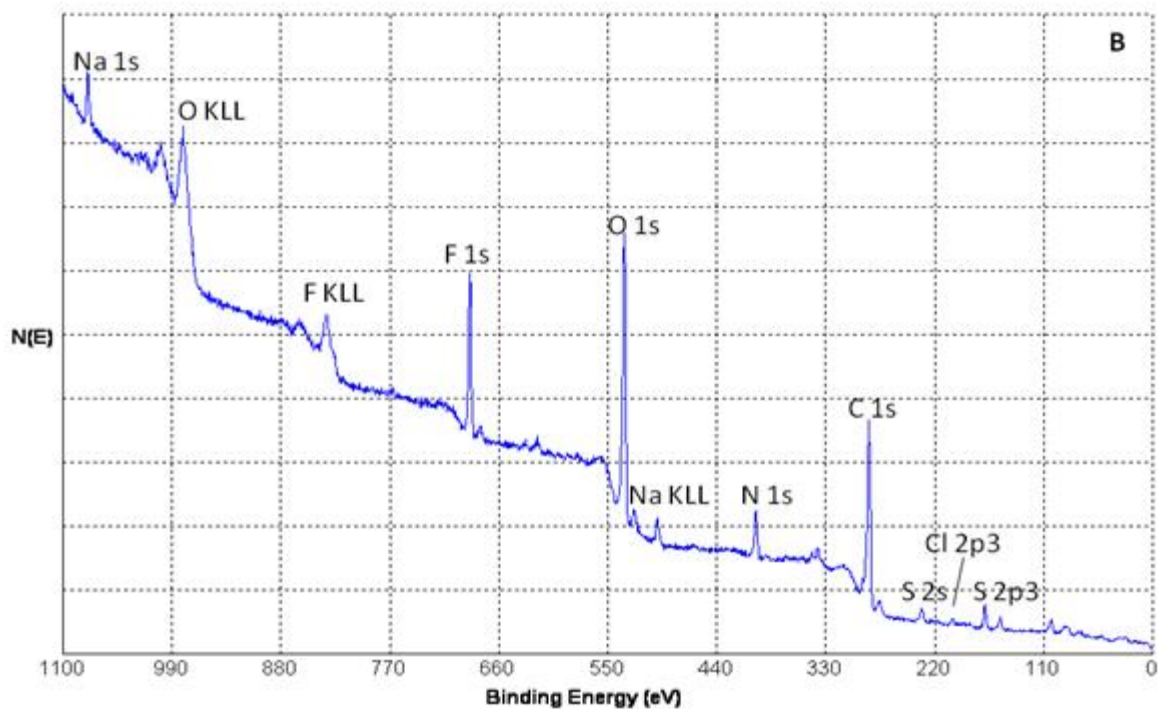
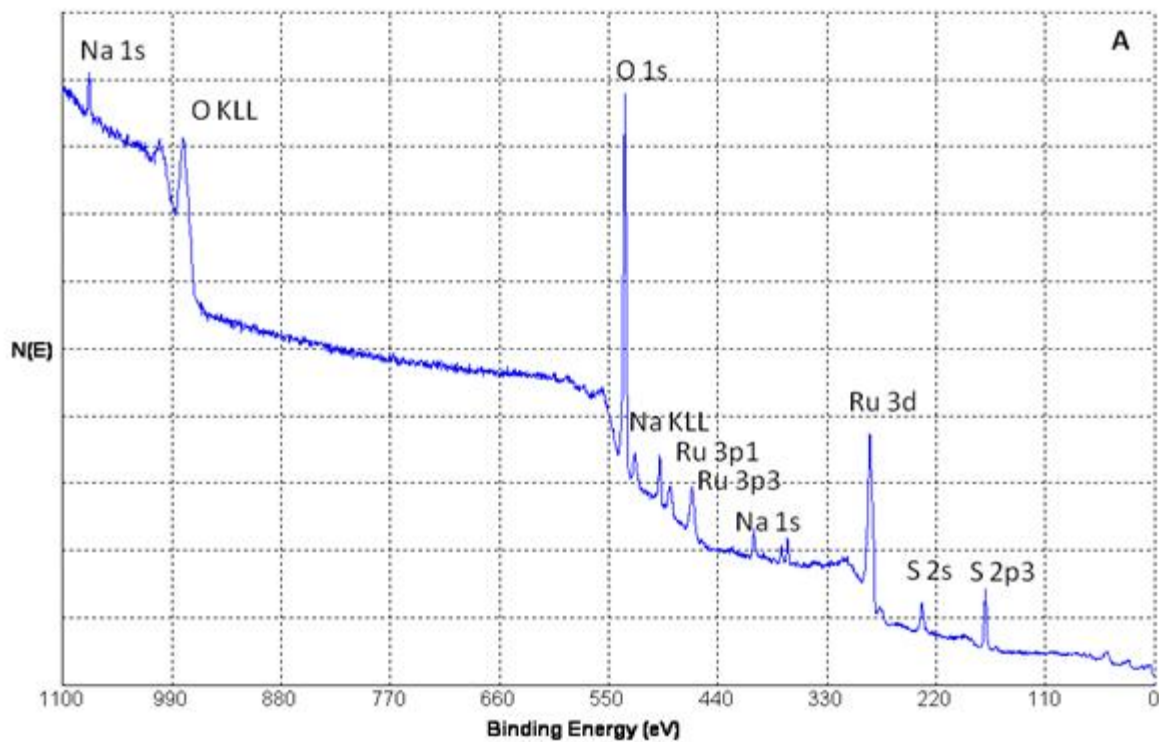


Figure 5-9. XPS survey scans of A) RuO<sub>x</sub>·nH<sub>2</sub>O|PProDOP|Sticky-PF|SWNTs film and B) PProDOP|Sticky-PF|SWNTs films.

## Characterization of the $\text{RuO}_x \cdot n\text{H}_2\text{O}|\text{PProDOP}$ Supercapacitor

The supercapacitor devices were constructed utilizing the same composite of  $\text{RuO}_x \cdot n\text{H}_2\text{O}$  and PProDOP materials in a symmetric configuration on both positive and negative electrodes. Sticky-PF coated SWNTs films ( $1\text{cm}^2$ ) were used as current collector substrates and  $0.5\text{M H}_2\text{SO}_4$  was used as the conductive electrolyte media. As was in the polymer-only Type I devices, one of the electrodes was initially set in the fully oxidized state and the other in the fully neutralized form to establish the initial charge state of the device. Subsequent discharging of the device causes neutralization of the p-doped PProDOP and reduction of oxyruthenium species proceeding with concurrent oxidation of the cathode PProDOP films with the oxidation of the ruthenium oxide film in the device. Since the quantity of charge that leaves one electrode must be equal to that injected onto the other electrode in two-electrode systems, the charge capacity of each electrode prepared by electrodeposition of first PProDOP and then  $\text{RuO}_x \cdot n\text{H}_2\text{O}$  (so that the amount of materials), was matched carefully before switching to the two-electrode system. Accordingly, no over accumulation of charges could have occurred when the device was switched between its charged and uncharged states, achieving optimal and balanced switching.

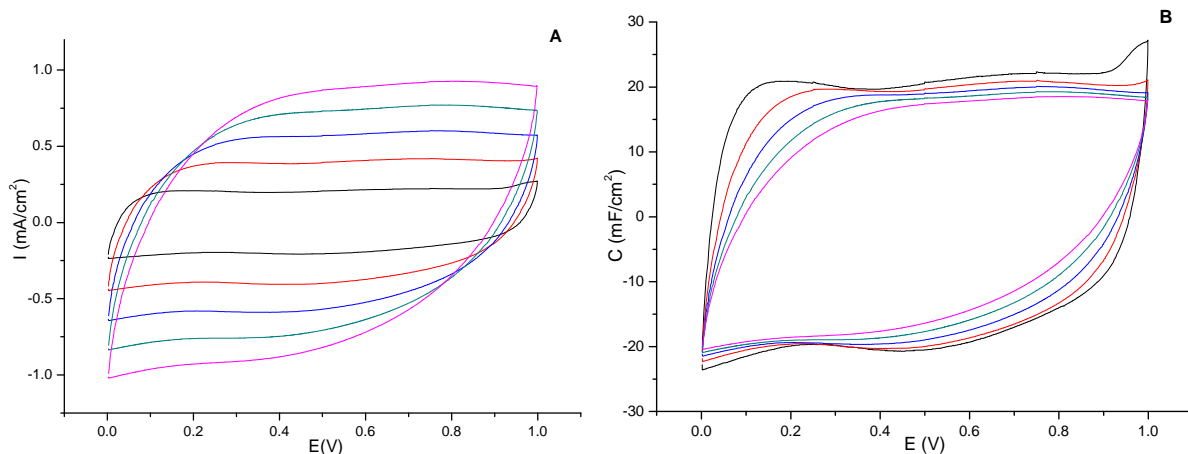


Figure 5-10. A) Cyclic voltammograms and B) capacitances as a function of applied potential of TYPE I Hybrid  $\text{RuO}_x \cdot n\text{H}_2\text{O}|\text{PProDOP}$  supercapacitor with Sticky-PF|SWNTs substrates using  $0.5\text{M H}_2\text{SO}_4$  at 10 to  $50\text{mV/s}$  with  $10\text{mV/s}$  intervals.

Fig 5-10A and B shows the cyclic voltammograms and the capacitance as a function of applied potential of the supercapacitor device at different scan rates from 10 to 50mV/s with 10 mV intervals in a 1V potential range, respectively. As in PProDOP-only Type I devices, here again there is a complete overlap between the electrochemical responses of anode and cathode electrodes since same material is utilized on both electrodes. Thus, the shape of the cyclic voltammogram of the supercapacitors would typically be a rectangular or parallelogram plot, showing a constant current within the operating voltage window of the device. As mentioned earlier, the matching working-potential windows of  $\text{RuO}_x \cdot n\text{H}_2\text{O}$  and PProDOP materials become critical here. As seen in Fig 5-10A, as expected, the voltammograms present the near-rectangular shape. The voltammograms indicate almost mirror images in between the anodic or cathodic scanning. A slight deviation in the voltammograms taken at relatively fast scan rates of 40 and 50mV/s, compared to slower scan rates of 10mV/s was observed.

As seen in the voltammograms of the electrodes in a three-electrode system, here again, the linear dependence of the current density on the scan rate was observed, indicative of the non-diffusion limited redox switching. The voltammograms demonstrate that  $\text{RuO}_x \cdot n\text{H}_2\text{O}$  |PProDOP composite devices show reproducible, relatively fast and efficient switching.

The capacitance graphs of the devices shown in Fig 5-10B were calculated using the relationship: " $C=i/s$ " (Equation 2-2). The capacitances show a constant value that is independent of the applied potential for the larger portion of potential ranges as dictated by the equation. Similar deviation were observed in the voltammograms taken at the relatively faster scan rates of 40 and 50mV/s, compared to slower scan rates of 10mV/s were also seen in the capacitance graphs.

The average capacitance values were calculated from the anodic and cathodic voltammetric charges, which were examined by integrating the voltammograms in the working potential range as had been performed for each of the film electrodes. Each electrode separately presented a capacitance of  $34\text{mF/cm}^2$ . The capacitance values obtained from the supercapacitor device was calculated as  $16.9\text{mF/cm}^2$  as shown in Fig 5-10B. Since the configuration of the device consisting of the composite material was very similar to polymer-only Type I devices, the relationship between the capacitance values of the device was expected to be one half the capacitances of the two individual electrodes connected in series in a two electrode device system, as explained in Chapter 3. Therefore, the capacitance of the device was expected to be  $17\text{mF/cm}^2$ , which exactly matches to the observed value of  $16.9\text{mF/cm}^2$ . The corresponding mass value was calculated as  $103\mu\text{g/cm}^2$  for both positive and negative electrodes and the specific capacitance of the device was determined to be  $165\text{F/g}$ . Although there was not any stability experiments were conducted, the films and devices were switched at least 50 cycles to collect the presented data and exhibit stable and reproducible performance.

The energy density of the device, shown in Fig 5-10, was calculated using the relationship; “ $E = \frac{1}{2} QV$ ” (Equation 1-2). The average charge density was determined from the cyclic voltammograms and the average voltage of the device was taken as the half of the potential difference between the electrodes at the initial charged state of the device. The energy density was found as  $11\text{Wh/kg}$ . The average power density was determined using the relationship: “ $P = iV$ ” (Equation 2-9). The average current density was determined from the cyclic voltammograms taken at different scan rates and the average power density was calculated as  $2289\text{W/kg}$ . Compared to PProDOP devices in Chapter 3, the energy density was increased 4.3 folds and power density was increased 4 folds. These energy and power densities are comparable with the

battery and electrochemical capacitors values estimated in the Ragone Plot (Fig 1-1). Table 5-1 summarize the areal and specific capacitances of the composite film of  $\text{RuO}_x \cdot n\text{H}_2\text{O}|\text{PProDOP}$  and device shown in Fig 5-10, along with the energy and power values.

Table 5-1. Capacitances, energy and power densities of the film and devices of  $\text{RuO}_x \cdot n\text{H}_2\text{O}|\text{PProDOP}$  composite.

<i>Film</i>		<i>Device</i>			
$C(\text{mF}/\text{cm}^2)$	$C(\text{F}/\text{g})$	$C(\text{mF}/\text{cm}^2)$	$C(\text{F}/\text{g})$	$E(\text{Wh}/\text{kg})$	$P(\text{W}/\text{kg})$
45	660	17	165	11.3	2289

### Conclusions and Perspective

In summary, this chapter demonstrates a novel device design utilizing a composite of conducting polymer and hydrous metal oxide as the charge storage material in Type I supercapacitors. A two step all electrochemical method for preparation of interpenetrating PProDOP and hydrous ruthenium oxide composite was introduced. In this method, PProDOP films have been electrochemically deposited on SWNT films covered by Sticky-PF, and then these films have been used as the scaffolds on which amorphous ruthenium oxide could be electrodeposited. The control of the electrochemical parameters allow some control of the thickness of the component and hence the porosity. The electrochemical properties of the corresponding films were investigated by using cyclic voltammetry and galvanostatic charging-discharging methods. The results show that ruthenium oxide deposition was increased 100% in capacitance per unit area on PProDOP compared to bare SWNT films. The method introduced in this chapter effectively demonstrated the contribution of each composite materials to the final capacitance outcome of the film. The morphological properties of the resulting films were investigated by using SEM and the images of the composite film were compared with the SEM images of SWNTs substrate itself and also the PProDOP itself on SWNTs substrate. Moreover, the elemental inspection of the composite film was investigated by XPS and the spectra of

PProDOP films before and after ruthenium oxide deposition were taken. In all electrochemical, morphological and elemental analysis indicate the synergy effect between the components of the composite film with increased capacitance values.

It is expected that further work to be conducted after this dissertation will focus on optimizing the proper combination of materials and electrode/device designs to achieve the best performance for varying intentions.

In further morphological studies of these sponge-like electrode materials, ESEM (Environmental Scanning Electron Microscope) that operates in a gaseous environment in the specimen chamber, rather than in vacuum like all other electron microscopes, could provide enormous advantages to investigate the porosity of the composite film.

## LIST OF REFERENCES

1. Conway, B. E. *Electrochemical Capacitors: Scientific Fundamentals and Technological Applications*; Kluwer Academic/Plenum: New York, NY 1999.
2. Becker, H. E. *Low voltage electrolytic capacitor*; General Electric Co, U. S. Patent 2,800,616, 1957.
3. Rightmire, R. A., *Electrical energy storage apparatus*, U. S. Patent 3,288,641, 1966.
4. Endo, M.; Takeda, T.; Kim, Y.J.; Koshiba, K.; Ishii, K. *Carbon Science* **2001**, 1, 117.
5. High Capacitance Capacitors [Internet]. NEC-Tokin Corporation; [cited 2009 Feb 02]. Available from: <http://www.nectokin.net/product/hypercapacitor/outline02.html>
6. Conway, B. E. *Journal of the Electrochemical Society* **1991**, 138, 6, 1539.
7. Conway, B. E.; Kozłowska, H. A. *Accounts of Chemical Research* **1981**, 14, 2, 49.
8. Jordanov, S. H.; Kozłowska, H. A.; Vukovic, M.; Conway, B. E. *Journal of the Electrochemical Society* **1978**, 125, 1471.
9. Galizzioli, R.; Tantardini, F.; Trasatti, S. *Journal of Applied Electrochemistry* **1974**, 4, 57.
10. International Energy Agency, *Report on the first phase of the IEA implementing agreement for hybrid electric vehicle technology and programmes 1993-1999*; International Energy Agency, Paris 1999.
11. The charge of ultracapacitors. [Internet]. Shindall, Joel; Institute of Electrical and Electronics Engineers *Spectrum*; [cited 2009 Jan 15]. Available from: <http://www.spectrum.ieee.org/nov07/5636>
12. Kotz, R.; Carlen, M. *Electrochimica Acta* **2000**, 45, 15-16, 2483.
13. Winter, M.; Brodd, R. J. *Chemical Reviews* **2004**, 104, 10, 4245.
14. Conway, B. E.; Birss, V.; Wojtowicz, J. *Journal of Power Sources* **1997**, 66, 1-2, 1.
15. Burke, A. *Journal of Power Sources* **2000**, 91, 1, 37.
16. Hughes, M.; Chen, G. Z.; Shaffer, M. S. P.; Fray, D. J.; Windle, A. H. *Chemistry of Materials* **2002**, 14, 4, 1610.
17. Niu, C. M.; Sichel, E. K.; Hoch, R.; Moy, D.; Tennent, H. *Applied Physics Letters* **1997**, 70, 11, 1480.
18. Mund, K.; Richter, G.; Weidlich, E.; Fahlstrom, U. *Pacing and Clinical Electrophysiology* **1986**, 9, 1225.

19. Sawai, K.; Ohzuku, T. *Journal of the Electrochemical Society* **1997**, 144, 3, 988.
20. Rossier, J. S.; Girault, H. H. *Physical Chemistry Chemical Physics* **1999**, 1, 15, 3647.
21. An, K. H.; Kim, W. S.; Park, Y. S.; Choi, Y. C.; Lee, S. M.; Chung, D. C.; Bae, D. J.; Lim, S. C.; Lee, Y. H. *Advanced Materials* **2001**, 13, 497.
22. Conway, B. E. *Progress in Surface Science* **1984**, 16, 1, 1.
23. Conway, B. E.; Pell, W. G. *Journal of Solid State Electrochemistry* **2003**, 7, 9, 637.
24. Sarangapani, S.; Tilak, B. V.; Chen, C. P. *Journal of the Electrochemical Society* **1996**, 143, 11, 3791.
25. Burke, A.; Arulepp, M. *Electrochemical Society Proceedings* **2001**, 21, 576.
26. Barbieri, O.; Hahn, M.; Herzog, A.; Kotz, R. *Carbon* **2005**, 43, 6, 1303.
27. Zhou, H.; Zhu, S.; Hibino, M.; Honma, I. *Journal of Power Sources* **2006**, 122, 219.
28. Sevilla, M.; Alvarez, S.; Centeno, T. A.; Fuertes, A. B.; Stoeckli, F. *Electrochimica Acta* **2007**, 52, 9, 3207.
29. Li, L.; Song, H.; Chen, X. *Electrochimica Acta* **2006**, 51, 5715.
30. Fernandez, J. A.; Morishita, T.; Toyoda, M.; Inagaki, M.; Stoeckli, F.; Centeno, T. A. *Journal of Power Sources* **2008**, 175, 1, 675.
31. Salitra, G.; Soffer, A.; Eliad, L.; Cohen, Y.; Aurbach, D. *Journal of the Electrochemical Society* **2000**, 147, 7, 2486.
32. Vix-Guterl, C.; Frackowiak, E.; Jurewicz, K.; Friebe, M.; Parmentier, J.; Beguin, F. *Carbon* **2005**, 43, 6, 1293.
33. Janes, A.; Permann, L.; Arulepp, M.; Lust, E. *Electrochemistry Communications* **2004**, 6, 3, 313.
34. Chmiola, J.; Yushin, G.; Gogotsi, Y.; Portet, C.; Simon, P.; Taberna, P. L. *Science* **2006**, 313, 5794, 1760.
35. Frackowiak, E.; Beguin, F. *Carbon* **2001**, 39, 6, 937.
36. Pandolfo, A. G.; Hollenkamp, A. F. *Journal of Power Sources* **2006**, 157, 1, 11.
37. Shukla, A. K.; Sampath, S.; Vijayamohan, K. *Current Science* **2000**, 79, 12.
38. Wang, J.; Zhang, S. Q.; Guo, Y. Z.; Shen, J.; Attia, S. M.; Zhou, B.; Zheng, G. Z.; Gui, Y. S. *Journal of the Electrochemical Society*. **2001**, 148, 6, D75.

39. Nelson, P. A.; Owen, J. R. *Journal of the Electrochemical Society* **2003**, 150, 10, A1313.
40. Moore, V. C.; Strano, M. S.; Haroz, E. H.; Hauge, R. H.; Smalley, R. E.; Schmidt, J.; Talmon, Y. *Nano Letters* **2003**, 3, 10, 1379.
41. Wu, Z. C.; Chen, Z. H.; Du, X.; Logan, J. M.; Sippel, J.; Nikolou, M.; Kamaras, K.; Reynolds, J. R.; Tanner, D. B.; Hebard, A. F.; Rinzler, A. G. *Science* **2004**, 305, 5688, 1273.
42. Lee, K.; Wu, Z.; Chen, Z.; Ren, F.; Pearton, S. J.; Rinzler, A. G. *Nano Letters* **2004**, 4, 5, 911.
43. Frackowiak, E.; Jurewicz, K.; Delpoux, S.; Beguin, F. *Journal of Power Sources* **2001**, 97, 822.
44. Frackowiak, E.; Beguin, F. *Carbon* **2002**, 40, 10, 1775.
45. Barisci, J. N.; Wallace, G. G.; Chattopadhyay, D.; Papadimitrakopoulos, F.; Baughman, R. H. *Journal of the Electrochemical Society* **2003**, 150, E409.
46. Shiraishi, S.; Kurihara, H.; Okabe, K.; Hulicova, D.; Oya, A. *Electrochemistry Communications* **2002**, 4, 7, 593.
47. Talapatra, S.; Kar, S.; Pal, S. K.; Vajtai, R.; Ci, L.; Victor, P.; Shaijumon, M. M.; Kaur, S.; Nalamasu, O.; Ajayan, P. M. *Nature Nanotechnology* **2006**, 1, 112.
48. Pushparaj, V. L.; Shaijumon, M. M.; Kumar, A.; Murugesan, S.; Ci, L.; Vajtai, R.; Linhardt, R. J.; Nalamasu, O.; Ajayan, P. M. *Proceedings of the National Academy of Sciences of the United States of America* **2007**, 104, 34, 13574.
49. Schindall, Joel *Institute of Electrical and Electronics Engineers Power Electronics Society Newsletter* **2008**, First Quarter, 20, 1, 32.
50. Wohlfahrt-Mehrens, M.; Schenk, J.; Wilde, P. M.; Abdelmula, E.; Axmann, P.; Garche, J. *Journal of Power Sources* **2002**, 105, 182.
51. Huggins, R. A. *Solid State Ionics* **2000**, 134, 1-2, 179.
52. Roberson, S. L.; Finello, D.; Davis, R.F.; Lui, W.; Pell, W.; Conway, B. E. *Proceedings of the 7th International Seminar on Double-layer Capacitors and Similar Energy Storage Devices*, Deerfield Beach, December 1997.
53. Kurzweil, P.; Schmid, O.; Loffler, A. *Proceedings of the 7th International Seminar on Double-layer Capacitors and Similar Energy Storage Devices*, Deerfield Beach, December 1997.
54. Long, J. W.; Swider, K. E.; Merzbacher, C. I.; Rolison, D. R. *Langmuir* **1999**, 15, 3, 780.
55. Zheng, J. P.; Jow, T. R. *Journal of the Electrochemical Society* **1995**, 142, 1, L6.

56. Cimino, A.; Carra, S. *Electrodes of Conductive Metallic Oxides - Part A.*; Trasatti, S., Ed.; Elsevier: New York, NY 1980; 97.
57. Miousse, D.; Lasia, A. *Journal of New Materials for Electrochemical Systems* **1999**, 2, 71.
58. Jeong, Y. U.; Manthiram, A. *Electrochemical and Solid State Letters* **2000**, 3, 5, 205.
59. Lee, H. Y.; Manivannan, V.; Goodenough, J. B., *Comptes rendus de l'Academie des sciences - Series Iic - Chemistry*, **1999**, 2, 11-13, 565.
60. Lee, H. Y.; Goodenough, J. B. *Journal of Solid State Chemistry* **1999**, 144, 1, 220.
61. Drezen, T.; Kwon, N.-H.; Bowenb, P.; Teerlinck, I.; Isono, M.; Exnar, I. *Journal of Power Sources* **2007**, 174, 949.
62. Wang, Y.; Takahashi, K.; Lee, K.; Cao, G. Z. *Advanced Functional Materials* **2006**, 16, 9, 1133.
63. Rudge, A.; Raistrick, I.; Gottesfeld, S.; Ferraris, J. P. *Electrochimica Acta* **1994**, 39, 2, 273.
64. Arbizzani, C.; Mastragostino, M.; Scrosati, B. *Handbook of Organic Conductive Molecules and Polymers*; Nalwa, H. S., Ed.; John Wiley & Sons, New York, NY, 1997; 11-1.
65. Novak, P.; Muller, K.; Santhanam, K. S. V.; Haas, O. *Chemical Reviews* **1997**, 97, 1, 207.
66. Mastragostino, M.; Arbizzani, C.; Soavi, F. *Journal of Power Sources* **2001**, 97-8, 812.
67. Ghosh, S.; Inganas, O. *Advanced Materials* **1999**, 11, 14, 1214.
68. Mastragostino, M.; Arbizzani, C.; Paraventi, R.; Zanelli, A. *Journal of the Electrochemical Society* **2000**, 147, 2, 407.
69. Fusalba, F.; El Mehdi, N.; Breau, L.; Belanger, D. *Chemistry of Materials* **1999**, 11, 10, 2743.
70. Gurunathan, K.; Murugan, A. V.; Marimuthu, R.; Mulik, U. P.; Amalnerkar, D. P. *Materials Chemistry and Physics* **1999**, 61, 3, 173.
71. Fusalba, F.; Belanger, D. *Journal of Physical Chemistry B* **1999**, 103, 42, 9044.
72. Carlberg, J. C.; Inganas, O. *Journal of the Electrochemical Society* **1997**, 144, 4, L61.
73. Rudge, A.; Davey, J.; Raistrick, I.; Gottesfeld, S.; Ferraris, J. P. *Journal of Power Sources* **1994**, 47, 1-2, 89.

74. Irvin, J. A.; Irvin D. J.; Stenger-Smith, J. D. *Handbook of Conducting Polymers - Electroactive Polymers for Batteries and Supercapacitors.*; Skotheim, T. A.; Reynolds, J. R., Ed.; Taylor and Francis Group, LLC: Boca Raton, FL, 2007; 9-1.
75. Leroux, F.; Koene, B. E.; Nazar, L. F. *Journal of the Electrochemical Society* **1996**, 143, 9, L181.
76. Mu, S.; Ye, J.; Wang, Y. *Journal of Power Sources* **1993**, 45, 153.
77. Mohammadi, A.; Inganas, O.; Lundstrom, I. *Journal of the Electrochemical Society* **1986**, 133, 5, 947.
78. Moon, D. K.; Padias, A. B.; Hall, H. K.; Huntoon, T.; Calvert, P. D. *Macromolecules* **1995**, 28, 18, 6205.
79. Meyer, W. H. *Advanced Materials* **1998**, 10, 6, 439.
80. Ratner, M. A.; Johansson, P.; Shriver, D. F. *Materials Research Society Bulletin* **2000**, 25, 3, 31.
81. Gray, F.; Armand, M. *Handbook of Battery Materials: Polymer Electrolytes*; Besenhard, J. O., Ed.; Wiley-VCH, New York, NY, 1999; 8-1.
82. Novak, P.; Vielstich, W. *Journal of the Electrochemical Society* **1990**, 137, 6, 1681.
83. Bittihn, R.; Ely, G.; Woeffler, F.; Muenstedt, H.; Naarmann, H.; Naegele, D. *Makromolekulare Chemie Macromolecular Symposium* **1987**, 8, 51.
84. Naegele, D.; Bittihn R. *Solid State Ionics* **1988**, 28-30, 2, 983.
85. Panero, S.; Prospero, P.; Scrosati, B. *Electrochimica Acta* **1987**, 32, 10, 1465.
86. Trinidad, F.; Alonsolopez, J.; Nebot, M. *Journal of Applied Electrochemistry* **1987**, 17, 1, 215.
87. Naoi, K.; Sakai, H.; Ogano, S.; Osaka, T. *Journal of Power Sources* **1987**, 20, 3-4, 237.
88. Prasad, K. R.; Munichandraiah, N. *Electrochemical and Solid State Letters* **2002**, 5, 12, A271.
89. Ofer, D.; Crooks, R. M.; Wrighton, M. S. *Journal of the American Chemical Society* **1990**, 112, 22, 7869.
90. Kinlen, P. J.; Mbugua, J.; Kim, Y.-G.; Jung, J.-H.; Viswanathan, S.; Liu, J., Abstract of papers, 236th ACS National Meeting, Philadelphia, PA, 2008.
91. Ibrisagic, Z. *Chemical and Biochemical Engineering* **1993**, 7, 4, 191.

92. Lee, J. Y.; Ong, L. H.; Chuah, G. K. *Journal of Applied Electrochemistry* **1992**, 22, 8, 738.
93. Echigo, Y.; Asami, K.; Takahashi, H.; Inoue, K.; Kabata, T.; Kimura, O.; Ohsawa, T. *Synthetic Metals* **1993**, 57, 1, 3611.
94. Arbizzani, C.; Mastragostino, M.; Meneghello, L. *Electrochimica Acta* **1996**, 41, 1, 21.
95. Kitani, A.; Iwai, K.; Ito, S. *Electrochemistry* **1999**, 67, 1262.
96. Nishio, K.; Fujimoto, M.; Yoshinaga, N.; Furukawa, N.; Ando, O.; Ono, H.; Suzuki, T. *Journal of Power Sources* **1991**, 34, 2, 153.
97. Hashmi, S. A.; Kumar, A.; Tripathi, S. K. *European Polymer Journal* **2005**, 41, 6, 1373.
98. Wu, H.-M.; Shy, H.-J.; Ko, H.-W. *Journal of Power Sources* **1989**, 27, 59.
99. Shacklette, L. W.; Jow, T. R.; Maxfield, M.; Hatami, R. *Synthetic Metals* **1989**, 28, 1-2, C655.
100. Yamamoto, T.; Zama, M.; Hishinuma, M.; Yamamoto, A. *Journal of Applied Electrochemistry* **1987**, 17, 3, 607.
101. Stenger-Smith, J. D.; Webber, C. K.; Anderson, N.; Chafin, A. P.; Zong, K.; Reynolds, J. R. *Journal of the Electrochemical Society* **2002**, 149, 8, A973.
102. Haringer, D.; Novak, P.; Haas, O.; Piro, B.; Pham, M. C. *Journal of the Electrochemical Society* **1999**, 146, 7, 2393.
103. Levine, K.; Iroh, J. O. *Journal of Materials Chemistry* **2001**, 11, 9, 2248.
104. Arbizzani, C.; Mastragostino, M. *Electrochimica Acta* **1990**, 35, 1, 251.
105. Rasch, B.; Novak, P.; Vielstich, W. *Synthetic Metals* **1991**, 43, 1-2, 2963.
106. Ramasamy, R. P.; Veeraraghavan, B.; Haran, B.; Popov, B. N. *J. Power Sources* **2003**, 124, 1, 197.
107. Mastragostino, M.; Scrosati, B. *Journal of the Electrochemical Society* **1985**, 132, 5, 1259.
108. Shacklette, L. W.; Toth, J. E.; Murthy, N. S.; Baughman, R. H. *Journal of the Electrochemical Society* **1985**, 132, 7, 1529.
109. Tourillon, G.; Garnier, F. *Journal of the Electrochemical Society* **1983**, 130, 10, 2042.
110. Sato, M.; Tanaka, S.; Kaeriyama, K. *Synthetic Metals* **1986**, 14, 4, 279.
111. Walker, C. W. *Journal of the Electrochemical Society* **1991**, 138, 6, 1559.

112. Nagatomo, T.; Omoto, O. *Journal of the Electrochemical Society* **1988**, 135, 9, 2124.
113. Mastragostino, M.; Marinangeli, A. M.; Corradini, A.; Arbizzani, C. *Electrochimica Acta* **1987**, 32, 11, 1589.
114. Jow, T. R.; Jen, K. Y.; Elsenbaumer, R. L.; Shacklette, L. W.; Angelopoulos, M.; Cava, M. P. *Synthetic Metals* **1986**, 14, 1-2, 53.
115. Bartley, T. *Proceedings of Advanced Capacitor World Summit*, Washington, DC, 2004, paper 13.
116. Burke, A. F.; Hardin, J. E.; Dowgiallo, E. J. *Proceedings of the 34th Power Sources Conference*, Cherry Hill, NJ, 1990.
117. Miller, J. R. *Electrochemical Capacitors*; Delnick F. M.; Tomkiewicz, M., Ed.; The Electrochemical Society Proceedings Series, Pennington, NJ, 1996.
118. Miller, J. R. *Proceeding of 56th Annual Meeting of the International Society of Electrochemistry*, Busan, Korea, 2005, paper 3C-001-IL.
119. Schottland, P.; Zong, K.; Gaupp, C. L.; Thompson, B. C.; Thomas, C. A.; Giurgiu, I.; Hickman, R.; Abboud, K. A.; Reynolds, J. R. *Macromolecules* **2000**, 33, 19, 7051.
120. Walczak, R. M.; Reynolds, J. R. *Advanced Materials* **2006**, 18, 9, 1121.
121. Steckler, T. T.; Abboud, K. A.; Craps, M.; Rinzler, A. G.; Reynolds, J. R. *Chemical Communications* **2007**, 46, 4904.
122. Reynolds, J. R.; Walczak, R. M.; Van der Aa, E. M.; Rinzler, A. *Supramolecular polymers associative to carbon nanotubes*, U.S. Patent Application 20080287638, 2008.
123. Conway, B. E.; Pell, W. G. *Journal of Power Sources* **2002**, 105, 2, 169.
124. Bard, A. J.; Faulkner, L. R. *Electrochemical Methods: Fundamentals and Applications 2nd ed.*; Wiley: New York, NY 2001.
125. Arbizzani, C.; Mastragostino, M.; Soavi, F. *Journal of Power Sources* **2001**, 100, 1-2, 164.
126. Ghosh, S.; Inganas, O. *Journal of the Electrochemical Society* **2000**, 147, 5, 1872.
127. Matsumoto, M. *Electrical Phenomena at Interfaces: Fundamentals, Measurements, and Applications 2nd ed. Vol. 76*; Ohshima, H.; Furusawa, K., Ed.; Marcel Dekker: New York, NY, 1998.
128. Dietrich, M.; Heinze, J.; Heywang, G.; Jonas, F. *Journal of Electroanalytical Chemistry* **1994**, 369, 1-2, 87.

129. Groenendaal, B. L.; Jonas, F.; Freitag, D.; Pielartzik, H.; Reynolds, J. R. *Advanced Materials* **2000**, 12, 7, 481.
130. Heywang, G.; Jonas, F. *Advanced Materials* **1992**, 4, 2, 116.
131. Kumar, A.; Welsh, D. M.; Morvant, M. C.; Piroux, F.; Abboud, K. A.; Reynolds, J. R. *Chemistry of Materials* **1998**, 10, 3, 896.
132. Welsh, D. M.; Kloeppner, L. J.; Madrigal, L.; Pinto, M. R.; Thompson, B. C.; Schanze, K. S.; Abboud, K. A.; Powell, D.; Reynolds, J. R. *Macromolecules* **2002**, 35, 17, 6517.
133. Cirpan, A.; Argun, A. A.; Grenier, C. R. G.; Reeves, B. D.; Reynolds, J. R. *Journal of Materials Chemistry* **2003**, 13, 10, 2422.
134. Mishra, S. P.; Krishnamoorthy, K.; Sahoo, R.; Kumar, A. *Journal of Polymer Science Part a-Polymer Chemistry* **2005**, 43, 2, 419.
135. Reeves, B. D.; Grenier, C. R. G.; Argun, A. A.; Cirpan, A.; McCarley, T. D.; Reynolds, J. R. *Macromolecules* **2004**, 37, 20, 7559.
136. Walczak, R. M., Synthetic methodology as a basis for conducting polymer design. Dissertation, University of Florida, Gainesville, FL, 2006.
137. Reynolds, J. R.; Ruiz, J. P.; Child, A. D.; Nayak, K.; Marynick, D. S. *Macromolecules* **1991**, 24, 3, 678.
138. Ruiz, J. P.; Dharia, J. R.; Reynolds, J. R.; Buckley, L. J. *Macromolecules* **1992**, 25, 2, 849.
139. Child, A. D.; Sankaran, B.; Larmat, F.; Reynolds, J. R. *Macromolecules* **1995**, 28, 19, 6571.
140. Pfluger, P.; Street, G. B. *Journal of Chemical Physics* **1984**, 80, 1, 544.
141. Thomas, C. A.; Zong, K.; Schottland, P.; Reynolds, J. R. *Advanced Materials* **2000**, 12, 3, 222.
142. Zotti, G.; Schiavon, G.; Berlin, A.; Pagani, G. *Chemistry of Materials* **1993**, 5, 4, 430.
143. Sonmez, G.; Schwendeman, I.; Schottland, P.; Zong, K. W.; Reynolds, J. R. *Macromolecules* **2003**, 36, 3, 639.
144. Roncali, J. *Chemical Reviews* **1992**, 92, 4, 711.
145. Schwendeman, I., Optical and transport properties of conjugated polymers and their application to electrochromic devices. Dissertation, University of Florida, Gainesville, FL, 2002.

146. Snook, G. A.; Peng, C.; Fray, D. J.; Chen, G. Z. *Electrochemistry Communications* **2007**, 9, 1, 83.
147. Wu, M. Q.; Snook, G. A.; Gupta, V.; Shaffer, M.; Fray, D. J.; Chen, G. Z. *Journal of Materials Chemistry* **2005**, 15, 23, 2297.
148. Pyo, M.; Bohn, C. C.; Smela, E.; Reynolds, J. R.; Brennan, A. B. *Chemistry of Materials* **2003**, 15, 4, 916.
149. Frackowiak, E.; Jurewicz, K.; Szostak, K.; Delpoux, S.; Beguin, F. *Fuel Processing Technology* **2002**, 77, 213.
150. Shinomiya, T.; Gupta, V.; Miura, N. *Electrochimica Acta* **2005**, 51, 21, 4412.
151. Zhihong Chen, Z., Electric field induced transparency modulation in single wall carbon nanotube ultra-thin films and a method to separate metallic and semiconducting nanotubes, Dissertation, University of Florida, Gainesville, FL, 2003.
152. Sinani, V. A.; Gheith, M. K.; Yaroslavov, A. A.; Rakhnyanskaya, A. A.; Sun, K.; Mamedov, A. A.; Wicksted, J. P.; Kotov, N. A. *Journal of the American Chemical Society* **2005**, 127, 10, 3463.
153. Bohn, C.; Sadki, S.; Brennan, A. B.; Reynolds, J. R. *Journal of the Electrochemical Society* **2002**, 149, 8, E281.
154. Ehli, C.; Rahman, G. M. A.; Jux, N.; Balbinot, D.; Guldi, D. M.; Paolucci, F.; Marcaccio, M.; Paolucci, D.; Melle-Franco, M.; Zerbetto, F.; Campidelli, S.; Prato, M. *Journal of the American Chemical Society* **2006**, 128, 34, 11222.
155. Britz, D. A.; Khlobystov, A. N. *Chemical Society Reviews* **2006**, 35, 7, 637.
156. Yuan, W. Z.; Sun, J. Z.; Dong, Y. Q.; Haussler, M.; Yang, F.; Xu, H. P.; Qin, A. J.; Lam, J. W. Y.; Zheng, Q.; Tang, B. Z. *Macromolecules* **2006**, 39, 23, 8011.
157. Chen, R. J.; Zhang, Y. G.; Wang, D. W.; Dai, H. J. *Journal of the American Chemical Society* **2001**, 123, 16, 3838.
158. DuBois, C. J.; Abboud, K. A.; Reynolds, J. R. *Journal of Physical Chemistry B* **2004**, 108, 25, 8550.
159. Thompson, B. C.; Kim, Y. G.; McCarley, T. D.; Reynolds, J. R. *Journal of the American Chemical Society* **2006**, 128, 39, 12714.
160. Colladet, K.; Fourier, S.; Cleij, T. J.; Lutsen, L.; Gelan, J.; Vanderzande, D.; Nguyen, L. H.; Neugebauer, H.; Sariciftci, S.; Aguirre, A.; Janssen, G.; Goovaerts, E. *Macromolecules* **2007**, 40, 1, 65.
161. Kulkarni, A. P.; Kong, X. X.; Jenekhe, S. A. *Macromolecules* **2006**, 39, 25, 8699.

162. Thompson, B. C.; Madrigal, L. G.; Pinto, M. R.; Kang, T. S.; Schanze, K. S.; Reynolds, J. R. *Journal of Polymer Science Part A: Polymer Chemistry* **2005**, 43, 7, 1417.
163. Sonmez, G.; Sonmez, H. B. *Journal of Materials Chemistry* **2006**, 16, 25, 2473.
164. Galand, E. M.; Mwaura, J. K.; Argun, A. A.; Abboud, K. A.; McCarley, T. D.; Reynolds, J. R. *Macromolecules* **2006**, 39, 21, 7286.
165. Sonmez, G. *Chemical Communications* **2005**, 42, 5251.
166. Irvin, D. J.; DuBois, C. J.; Reynolds, J. R. *Chemical Communications* **1999**, 20, 2121.
167. Thomas, C. A.; Zong, K. W.; Abboud, K. A.; Steel, P. J.; Reynolds, J. R. *Journal of the American Chemical Society* **2004**, 126, 50, 16440.
168. Dubois, C. J., Donor-acceptor methods for band gap control in conjugated polymers. Dissertation, University of Florida, Gainesville, FL, 2003.
169. Van Mullekom, H. A. M.; Vekemans, J. A. J. M.; Havinga, E. E.; Meijer, E. W. *Materials Science and Engineering: R: Reports* **2001**, 32, 1, 1.
170. Trasatti, S. *Electrochimica Acta* **1991**, 36, 2, 225.
171. Takasu, Y.; Murakami, Y. *Electrochimica Acta* **2000**, 45, 25-26, 4135.
172. Zheng, J. P.; Cygan, P. J.; Jow, T. R. *Journal of the Electrochemical Society* **1995**, 142, 8, 2699.
173. Hu, C. C.; Huang, Y. H. *Journal of the Electrochemical Society* **1999**, 146, 7, 2465.
174. Fang, Q. L.; Evans, D. A.; Roberson, S. L.; Zheng, J. P. *Journal of the Electrochemical Society* **2001**, 148, 8, A833.
175. Zheng, J. P.; Huang, C. K. *Journal of New Materials for Electrochemical Systems* **2002**, 5, 1, 41.
176. Zheng, J. P. *Electrochemical and Solid State Letters* **1999**, 2, 8, 359.
177. Jow, T. R.; Zheng, J. P. *Journal of the Electrochemical Society* **1998**, 145, 1, 49.
178. Zheng, J. P.; Xin, Y. *Journal of Power Sources* **2002**, 110, 1, 86.
179. Long, J. W.; Swider, K. E.; Merzbacher, C. I.; Rolison, D. R. *Langmuir* **2003**, 19, 6, 2532.
180. Long, J. W.; Ayers, K. E.; Rolison, D. R. *Journal of Electroanalytical Chemistry* **2002**, 522, 1, 58.

181. McKeown, D. A.; Hagans, P. L.; Carette, L. P. L.; Russell, A. E.; Swider, K. E.; Rolison, D. R. *Journal of Physical Chemistry B* **1999**, 103, 23, 4825.
182. Vukovic, M.; Cukman, D. *Journal of Electroanalytical Chemistry* **1999**, 474, 2, 167.
183. Kim, I. H.; Kim, K. B. *Electrochemical and Solid State Letters* **2001**, 4, 5, A62.
184. Hu, C. C.; Chen, W. C.; Chang, K. H. *Journal of the Electrochemical Society* **2004**, 151, 2, A281.
185. Sugimoto, W.; Iwata, H.; Yokoshima, K.; Murakami, Y.; Takasu, Y. *Journal of Physical Chemistry B* **2005**, 109, 15, 7330.
186. Hu, C. C.; Chu, C. H. *Materials Chemistry and Physics* **2000**, 65, 3, 329.
187. He, B. L.; Zhou, Y. K.; Zhou, W. J.; Dong, B.; Li, H. L. *Materials Science and Engineering A - Structural Materials: Properties Microstructure and Processing* **2004**, 374, 1-2, 322.
188. Park, J. H.; Ko, J. M.; Park, O. O. *Journal of the Electrochemical Society* **2003**, 150, 7, A864.
189. Wen, T. C.; Hu, C. C. *Journal of the Electrochemical Society* **1992**, 139, 8, 2158.

## BIOGRAPHICAL SKETCH

Merve Ertas was born and raised in Turkey. She received her B.S. in 2002 followed by her M.S. in 2003 in chemistry at METU, Ankara, where she worked in the research group of Professor Levent Toppare. Soon after, she moved to the University of Florida, Department of Chemistry to begin her doctoral studies under the supervision of Professor John R. Reynolds. During her time at the University of Florida, she also conducted research in several projects in collaboration with Professor Andrew G. Rinzler in the Department of Physics.